STARS

Electronic Theses and Dissertations

2019

Non-Hermitian and Space-Time Mode Management

Nicholas Nye
University of Central Florida

STARS Citation

University of
Central
Florida

STARS
Showcase of Text, Archives, Research & Scholarship

NON-HERMITIAN AND SPACE-TIME MODE MANAGEMENT

by

NICHOLAS S. NYE

B.S. Aristotle University of Thessaloniki, 2012
M.S. Aristotle University of Thessaloniki, 2012
M.S. University of Central Florida, 2017

A dissertation submitted in partial fulfillment of the requirements
for the degree of Doctor of Philosophy
in CREOL/The College of Optics & Photonics
at the University of Central Florida
Orlando, Florida

Spring Term
2019

Major Professor: Demetrios N. Christodoulides

ABSTRACT

In the last few years, optics has witnessed the emergence of two fields namely metasurfaces and parity-time (PT) symmetry. Optical metasurfaces are engineered structures that provide unique responses to electromagnetic waves, absent in natural materials. On the other hand, PT symmetry has emerged from quantum mechanics, when a new class of non-Hermitian Hamiltonian quantum systems was shown to have real eigenvalues. In this work, we demonstrate how PT-symmetric diffractive structures are capable of eliminating diffraction orders in specific directions, while maintaining/enhancing the remaining orders. In the second part of this work, we emphasize on supersymmetry (SUSY) and its applications in optics. Even though the full ramification of SUSY in high-energy physics is still a matter of debate that awaits experimental validation, supersymmetric techniques have already found their way into low-energy physics. In this work, we apply certain isospectral techniques in order to achieve single mode lasing in multi-element waveguide systems, where multimode chaotic emission is expected. In the third part of this dissertation, we emphasize on dynamically reconfigurable nanoparticle platforms. By exploiting the dielectrophoresis effect, we demonstrate how controllable lasing can be achieved in random photonic arrangements. Although this work focuses on the case of controlling random lasers, we expect that the proposed nanoparticle architecture can incorporate heterogeneous materials of a wide range of optical functionalities, including gain, scattering, plasmonic resonance, and nonlinearity. In the last part of the dissertation, we demonstrate the capability of synthesizing space-time (ST) wave packets, based on new propagation-invariant elementary

solutions of the wave equation identified through a complexification of the spatial and temporal degrees of freedom. By establishing the connection between ST propagation-invariant pulses and tilted-pulse-front pulses, a path is opened to exploiting the unique attributes of such wave packets both in nonlinear and quantum optics.

To my family.

ACKNOWLEDGMENTS

Finally, and above all, I would like to thank my family for being patient and supportive during this challenging period of my life.

TABLE OF CONTENTS

LIST OF FIGURES

from the same location of a sample, before and after particle alignment respectively. (d) All spectra shown are collected from a single sample of TiO2 wires (2.16 × 108 wires/mL) suspended in rB EG solution (2 mM). Each plot displays six spectra (initial conditions correspond to top spectra set) obtained from several sample locations. Wire alignment conditions were cycled between unassembled (black) to assembled (red). Ability to turn lasing on/off repeatedly shows robustness of the response. (e) Calculated reduced scattering coefficient plots (black line: randomly oriented wires, red line: wires aligned via applied field) dependent on the heterogeneous wire lengths of sample (a-b) (blue bars). The shaded region between lines represents the increase in reduced scattering coefficient due to

Figure 4.8 The commercially available TiO2 wires are rather heterogeneous in length, and tend to form large aggregates in solution if they are not sonicated. Insets are TEM images used in size measurements (a). Brief bath sonication was used to reduce aggregation and narrow the length distribution of reconfigurable random laser samples to 1.23 μm ± 1.1 μm (total wires counted = 532). (b) Probe sonication was used to further reduce average wire length by breaking long particles into smaller segments, ultimately reaching an average size

Figure 4.9 Scattering simulations, lasing spectra, and wire length/scattering histogram for shorter nanowires, with mean length of 0.6μm. (a, b) Near- and far-field plots representing scattering from a single TiO2 nanowire of length 1.3μm for circularly polarized incident 585 nm light. (a) light incidence parallel to the long axis of wire and (b) incident light perpendicular to the long axis of wire. (c,d) Random laser emission at very high short wire

CHAPTER 1: INTRODUCTION

Synthesizing ultrathin photonic structures in order to effectively redirect and mould optical wavefronts into arbitrary shapes, is of crucial importance in modern beam steering, imaging, and sensing technologies. To this end, planar subwavelength systems such as optical metasurfaces, have been intensely investigated in recent years. Such arrangements rely on abrupt, yet gradient, phase shifts imparted on the incident beam, by means of judiciously designed anisotropic nanoantennas. Here, we propose and demonstrate an altogether different methodology in order to manipulate the flow of light, by adopting a diatomic parity-time (PT)-symmetric Bravais lattice topology, whose unit cell involves only a transparent and a lossy optical component. In this respect, a honeycomb-like configuration is employed, whose principal symmetries are progressively broken through specific geometric transformations. The complex near-field coupling interactions between neighboring diffractive elements give rise to a discerning enhancement/attenuation along specific directions in the far-field, over a broad range of wavelengths in the visible domain. In this work, we report the realization of an all-passive PT-symmetric optical metasurface on a flexible polyimide substrate, capable of demonstrating selective directional scattering. Our study draws a clear connection between surface topology and radiation directivity, which can be systematically utilized towards observing unconventional transport effects in flat and curved space PT lattices.

In Chapter 3, we emphasize on the theory of supersymmetry (SUSY), along with its practical implications in optics. Supersymmetry emerged within particle physics as a means

1

to relate two fundamentally different classes of elementary particles: bosons (integer spin, Bose-Einstein statistics) and fermions (half integer spin, Fermi-Dirac statistics). Extensions to the Standard Model have also been proposed based on SUSY theory in order to resolve long-standing issues in quantum field theory, including the nature of vacuum energy, origin of mass scales and dark matter. Even though the experimental validation of SUSY is still an ongoing issue, supersymmetric/isospectral techniques have already found applications in low-energy physics, nonrelativistic quantum mechanics, and nonlinear dynamics, to name a few. On the other hand, waveguide laser arrays have been a subject of intense investigations for the purpose of building high-power phase-locked lasers, which are immune to the detrimental effects of nonlinearities or filamentation. Nevertheless, such systems suffer from multimode operation, which in turn leads to a chaotic emission. In this work, we proposed and demonstrated a scheme for filtering the undesired transverse supermodes of laser arrays by using the SUSY concept.

In Chapter 4 of this dissertation, we shed light on dynamically reconfigurable optical platforms, which take into advantage the effect of dielectrophoresis. Typically, top-down fabrication is used to provide positioning control of optical structures; yet, it places stringent limitations on component materials and oftentimes, dynamic reconfigurability is challenging to realize. Here, we present a nanoparticle platform that can integrate heterogeneous particle assembly of different shapes, sizes, and material compositions. We demonstrate dynamic manipulation of disorder in this platform and use it to controllably enhance or frustrate random laser emission for a suspension of titanium dioxide nanowires in a dye solution. Using an alternating current electric field, we control the nanowire orientation to

dynamically control the collective scattering of the sample and thus light confinement. Our theoretical model indicates that an increase of 22% in scattering coefficient can be achieved for the experimentally determined nanowire length distribution upon alignment. As a result, a nearly 20-fold enhancement in lasing intensity was achieved. We illustrate the generality of the approach by demonstrating enhanced lasing for aligned nanowires of other materials including gold, mixed gold/dielectric and vanadium oxide (V_xO_y).

Finally, in Chapter 5 we study the properties of tilted-pulse-front pulses, produced by dispersive devices that introduce angular dispersion. Such pulses typically have large transverse cross sections and propagate for limited distances to offset the impact of diffractive space-time coupling that leads to spectral walk-off. Here we show that sculpting the spatio-temporal spectral profile of a pulsed plane wave enables the synthesis of propagation-invariant wave packets endowed with a tilted intensity pulse front with respect to the propagation axis. These wave packets are based on new elementary propagation-invariant wave-packet solutions to the wave equation obtained by a complexification of the spatial and temporal degrees of freedom. The dissertation finishes with concluding remarks in Chapter 6.

CHAPTER 2: PT-SYMMETRIC OPTICAL METASURFACES

2.1 Introduction

The advent of metasurfaces has incited an intense research activity in the field of planar photonics. In such systems, a gradual phase shift can be imposed on the incident optical wavefront, thus leading to a generalized version of Snell's law [1]. Their inherent ability to control the phase, polarization, and angular momentum of the incident light via surface-confined subwavelength nanofeatures, has made such artificial structures of great interest for a number of applications [4-8], aimed towards scalable refractive or diffractive optical components. In recent years, parity-time synthetic photonic arrangements have also been the subject of extensive investigation [9-11]. Such PT-symmetric concepts - originally conceived within the context of quantum field theories – provide a means to construct new classes of non-Hermitian Hamiltonians, capable of exhibiting entirely real eigenvalue spectra. Given that in optics, the complex refractive index $n(\boldsymbol{r})$ plays the role of a quantum mechanical potential $V(\boldsymbol{r})$, one may then c-onclude that in a photonic setting, PT symmetry requires that the following condition is fulfilled $n(\boldsymbol{r}) = n^*(-\boldsymbol{r})$. In other words, the real part of the refractive index must be an even function of position, while the imaginary component, denoting gain or loss, must be antisymmetric. In more general arrangements, where the problem must be treated electrodynamically [12], this same symmetry implies that the complex permittivity satisfies $\varepsilon(\boldsymbol{r}) = \varepsilon^*(-\boldsymbol{r})$.

The nontrivial interplay between gain and loss domains in non-Hermitian platforms has led to a number of exciting possibilities, that have no counterpart in Hermitian

environments. These include for example, power oscillations, scattering elimination, non-reciprocal light propagation, and exceptional-point dynamics, to name a few [13-18]. The anomalous scattering properties of such systems – resulting from an underlying spontaneous symmetry breaking mechanism - have been considered within the context of PT-symmetric metasurfaces. So far, the potential of these arrangements has been the subject of mostly theoretical studies, and applications have been proposed for electromagnetic cloaking, subwavelength sensing, and planar focusing [19-23]. While asymmetric light transport and violation of Friedel's law have been reported in one-dimensional diffraction settings [24-27], the more complex analogs of these effects in higher-dimensional free-space optical platforms, still remain experimentally elusive.

In this chapter [33], we show that one-dimensional (1D) and two-dimensional (2D) optical metasurfaces endowed with PT-symmetry can display several intriguing characteristics. As we will see, PT-symmetry can be readily introduced in these systems through an appropriate amplitude and phase modulation when imposed on the surface. Such non-Hermitian structures are capable of eliminating diffraction orders in specific directions, while maintaining or even enhancing the remaining orders. Moreover, we have realized a rather unexplored family of "deformed" honeycomb arrangements, whose two-dimensional geometric distortions dictate the scattered far-field directivities. The observed asymmetric light transport is a direct byproduct of spontaneous PT symmetry breaking and signifies a clear violation of Friedel's law of diffraction. The proposed PT-symmetric dimer model relies on deeply subwavelength near-field interactions between a lossy diffractive element and its transparent counterpart. In this manner, we demonstrate robust control over the

5

propagating free-space modes and a pronounced unidirectionality. As with passive non-Hermitian waveguide arrangements, where loss-induced transparency is possible [14], in the present work we report loss-induced enhancement/suppression of radiation towards specific directions of interest in the visible part of the spectrum.

2.2 One-dimensional PT-symmetric metasurfaces

To analyze the optical properties of a PT-symmetric metasurface, we assume that the complex refractive index $n(x) = f(x) + ig(x)$ is periodically modulated on the surface. Here $f(x)$ and $g(x)$ are periodic real functions having a spatial period L, representing the length of each unit cell on this metasurface. In this regard, $n(x)$ can be expressed through a Fourier series as follows

$$n(x) = (a_0 + ia_0') + \frac{1}{2}\sum_{m=1}^{\infty}[(a_m + b_m') + i(a_m' - b_m)]e^{im\theta}$$

$$+ \frac{1}{2}\sum_{m=1}^{\infty}[(a_m - b_m') + i(a_m' + b_m)]e^{-im\theta} \tag{2.1}$$

where $\theta = 2\pi x/L$. In Eq. (2.1), $\{a_m, b_m\}$ and $\{a_m', b_m'\}$ represent the Fourier coefficients associated with the real $f(x)$ and imaginary $g(x)$ components of the complex refractive index distribution, respectively. The envisioned PT-symmetric metasurface is expected to be implemented solely using passive components, i.e. the imaginary component $g(x)$ will introduce only loss.
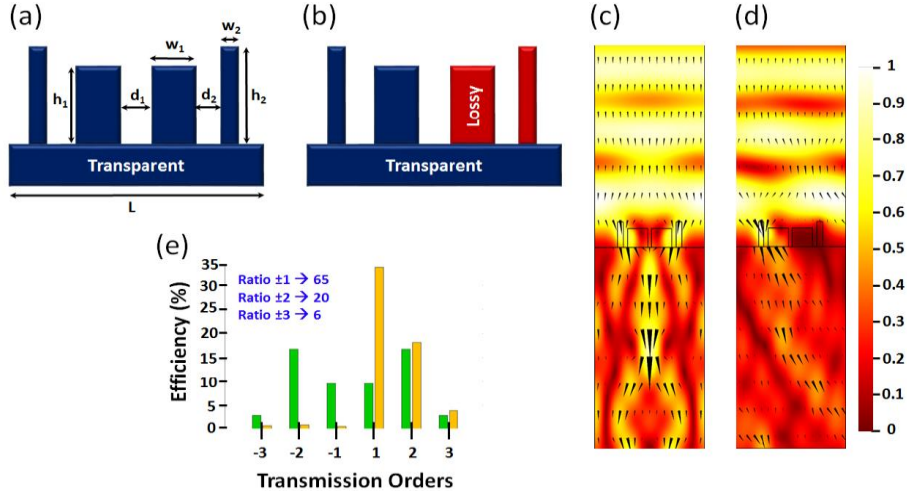
Figure 2.1 1D metasurface design for 1550 nm. The respective unit cell dimensions are L = 1520 nm, h1 = 230 nm, h2= 310 nm, w1 = 280 nm, w2= 80 nm, d1 = 50 nm, d2= 60 nm. The transparent material is silicon with a refractive index nSi = 3.4757 [32], while the lossy medium used is nickel with a refractive index nNi =3.4378 - 6.7359i [28]. (a, c) Hermitian case (when no loss is incorporated) and corresponding near-field and Poynting vector (arrow plots), (b,d) PT-symmetric case (when loss is introduced) and corresponding near-field and Poynting vector distributions, (e) transmission order efficiencies for the Hermitian case (green) and PT-symmetric case (yellow) and extinction ratios between the positive and corresponding negative orders (blue).

Of interest would be to identify methods through which the negative (or positive) diffraction orders emanating from this PT-symmetric metasurface can be entirely suppressed while the remaining orders (positive or negative) can be enhanced. For this to occur one has to eliminate, for example, the negative orders $\exp(-im\theta)$ appearing in the Fourier series of Eq. (2.1). This directly implies that $b'_m = a_m$ and $a'_m = -b_m$. From here, one obtains the following representations for $f(x)$, $g(x)$ that are necessary to suppress the negative orders

7

$$f(x) = a_0 + \sum_{m=1}^{\infty} \left\{ a_m \cos\left(m\frac{2\pi x}{L}\right) + b_m \sin\left(m\frac{2\pi x}{L}\right) \right\}$$

$$g(x) = a_0' + \sum_{m=1}^{\infty} \left\{ a_m \sin\left(m\frac{2\pi x}{L}\right) - b_m \cos\left(m\frac{2\pi x}{L}\right) \right\} \tag{2.2}$$

Equations (2.2) show that this is only possible as long as the real and imaginary parts of the refractive index are intertwined through common coefficients a_m, b_m. This index distribution is PT-symmetric, when the terms in Eq. (2.2) associated with the a_m, b_m coefficients are considered separately. Similarly, one can eliminate the positive orders $e^{im\theta}$ provided that $b_m' = -a_m$ and $a_m' = b_m$, in which case the following relations hold true

$$f(x) = a_0 + \sum_{m=1}^{\infty} \left\{ a_m \cos\left(m\frac{2\pi x}{L}\right) + b_m \sin\left(m\frac{2\pi x}{L}\right) \right\}$$

$$g(x) = a_0' + \sum_{m=1}^{\infty} \left\{ -a_m \sin\left(m\frac{2\pi x}{L}\right) + b_m \cos\left(m\frac{2\pi x}{L}\right) \right\} \tag{2.3}$$

Equations (2.2) and (2.3) indicate that, in order to eliminate either the negative or the positive orders, $f(x)$ and $g(x)$ must be PT-symmetric partners. The diffractive configuration considered here, essentially acts like a phase screen with a phase transmission function of the form $\exp(ik_0 n(x)d)$, where d represents an effective depth. Equations (2.1-3) provide a methodology for designing such unidirectional metasurfaces. Once the subwavelength surface elements are positioned on the surface in a PT-symmetric fashion, finite element simulations (FEM) are then used to further optimize the performance of such arrangements.

Based on the aforementioned analysis we investigate the optical properties of the structures shown in Figs. 2.1 and 2.2, for the wavelengths of 1550 and 532 nm, respectively. These configurations were conceived by matching the Fourier coefficients in a discrete fashion. These systems were subsequently optimized using finite element methods. For the

1550 nm design (Fig. 2.1) we employ silicon as the transparent material and nickel for loss. On the other hand, the 532 nm design (Fig. 2.2) is based on sapphire (as the transparent medium) and again utilizes nickel for loss. In general, the real part of the refractive indices of the transparent and lossy materials are here approximately equal in order to satisfy the PT-symmetry condition. We would like to note that, while the imaginary component in our designs is not exactly antisymmetric, their response is still dictated to a great extent by PT symmetry. This is due to the fact, that PT symmetric related processes can be quite robust and hence can tolerate environments, where this symmetry is not exactly satisfied. For both wavelengths, we assume normal incidence and a TE-polarization, i.e. the electric field is parallel to the 1D stripes of this metasurface. Under these conditions, the designs shown in Figs. 2.1 and 2.2 support up to six transmission orders.

In order to evaluate the performance of these configurations, we consider an extinction ratio, defined as the ratio between the diffraction efficiencies associated with the positive orders to that of the negative orders and vice versa. The FEM results corresponding to the aforementioned structures are shown in Figs. 2.1 & 2.2. As expected, if no loss is incorporated in the system (Hermitian case), light propagates symmetrically after this metasurface, as shown in Figs. 2.1(c) and 2.2(c). In this case the positive and negative orders are exactly the same. This scenario changes once loss from nickel is introduced. The resulting field distributions and Poynting vector plots are shown in Figs. 2.1(d), 2.2(d). Under these conditions, the light is skewed in one direction, towards the lossy side. The physical reason behind this symmetry-breaking behavior has to do with the redistribution of energy flow within the system. In other words, the Poynting vector now develops an additional

9

transverse component that is needed to supply energy to the lossy domains. For the 1550 nm design, the FEM simulations show that the extinction ratio between the ± 1 orders is approximately 65 (18 dB), for the ± 2 is 20 (13 dB) and for the ± 3 the extinction ratio is approximately 6 (Fig. 2.1(e)). On the other hand, the design intended for 532 nm exhibits optimum performance for the ± 2 orders where the extinction ratio is 1800 or 33 dB. Meanwhile for the remaining two orders it ranges between 62 to 16 (Fig. 2.2(e)). In essence, these metasurface designs can effectively suppress the positive (negative) orders by exploiting the symmetry-breaking induced by parity-time symmetry.

2.3 Diatomic Oblique Bravais Lattices

In the present section, we study the scattering properties of a rather unexplored family of "deformed" honeycomb arrangements, stemming from a generalized class of diatomic oblique Bravais lattices. The two-dimensional geometric distortions present in such arrangements lead to highly anisotropic radiation diagrams. The strong interplay between the surface geometry and radiation directivity has been rigorously analyzed and systematic methodologies have been developed in order to tailor the near- and far-field scattering characteristics, based on PT-symmetric dimer model.
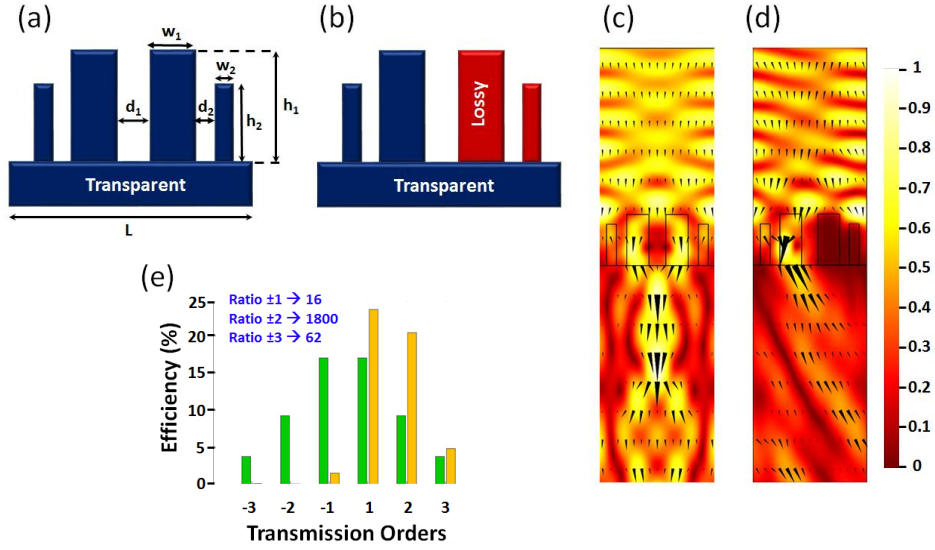
Figure 2.2 1D metasurface design for 532 nm. The corresponding unit cell dimensions are L = 1050 nm, h1 = 470 nm, h2= 380 nm, w1 = 200 nm, w2= 90 nm, d1 = 150 nm, d2= 90 nm. The transparent material is sapphire with refractive index nAl2O3=1.7718 [29], while the lossy material is nickel with refractive index nNi =1.7764 – 3.776i [28]. (a, c) Hermitian case (when no loss is incorporated) and corresponding near-field distribution and Poynting vector (arrow plots), (b, d) PT-symmetric case (when loss is introduced) and corresponding near-field distribution and Poynting vector plot, (e) transmission order efficiencies for the Hermitian case (green) and PT-symmetric case (yellow) and extinction ratios between the positive and corresponding negative orders (blue).

2.3.1 Scattering Analysis

The unit cell vectors, describing an oblique Bravais lattice topology with dimensions $L_a \times L_b$ and lattice angle φ_L (see Fig. 2.3), are given by $\boldsymbol{a_1} = L_a \boldsymbol{x}$, $\boldsymbol{a_2} = L_b \{\cos(\varphi_L)\,\boldsymbol{x} + \sin(\varphi_L)\,\boldsymbol{y}\}$. Following the analysis for a three-dimensional periodic arrangement, the reciprocal lattice vectors will be given by $\boldsymbol{G_1} = 2\pi(\boldsymbol{a_2} \times \boldsymbol{a_3})/\{\boldsymbol{a_1} \cdot (\boldsymbol{a_2} \times \boldsymbol{a_3})\} = 2\pi\{\boldsymbol{x} - \cot(\varphi_L)\,\boldsymbol{y}\}/L_a$, $\boldsymbol{G_2} = 2\pi(\boldsymbol{a_3} \times \boldsymbol{a_1})/\{\boldsymbol{a_2} \cdot (\boldsymbol{a_3} \times \boldsymbol{a_1})\} = 2\pi\,csc(\varphi_L)\,\boldsymbol{y}/L_b$, where $\boldsymbol{a_3} = \boldsymbol{z}$ As a result, we obtain relations $\boldsymbol{G_1} = 2\pi\{\boldsymbol{x} - \cot(\varphi_L)\,\boldsymbol{y}\}/L_a$, $\boldsymbol{G_2} = 2\pi\,csc(\varphi_L)\,\boldsymbol{y}/L_b$. The incident wavevector can

be expressed as $\boldsymbol{k}_i = k_0 n_1 \{\sin(\theta_i)\cos(\varphi_i)\,\boldsymbol{x} + \sin(\theta_i)\sin(\varphi_i)\,\boldsymbol{y} + \cos(\theta_i)\,\boldsymbol{z}\}$, where k_0 is the free space wavenumber, n_1 represents the refractive index of the incident medium, and θ_i, φ_i denote the elevation and azimuth angles of the electromagnetic wave, respectively. The phase matching condition dictates that $\boldsymbol{k}_{t,\parallel} = \boldsymbol{k}_{i,\parallel} + n\boldsymbol{G}_1 + m\boldsymbol{G}_2$, where (n, m) indicates the propagating order, while $\boldsymbol{k}_{i,\parallel}$ and $\boldsymbol{k}_{t,\parallel}$ represent the tangential components of the incident and diffracted wavevectors, correspondingly. Consequently, we attain

$$\boldsymbol{k}_{t,\parallel} = \left\{ k_0 n_1 \sin(\theta_i)\cos(\varphi_i) + n\frac{2\pi}{L_a} \right\} \boldsymbol{x}$$

$$+ \left\{ k_0 n_1 \sin(\theta_i)\sin(\varphi_i) - n\frac{2\pi}{L_a}\cot(\varphi_L) + m\frac{2\pi}{L_b}\csc(\varphi_L) \right\} \boldsymbol{y} \qquad \textbf{(2.4)}$$
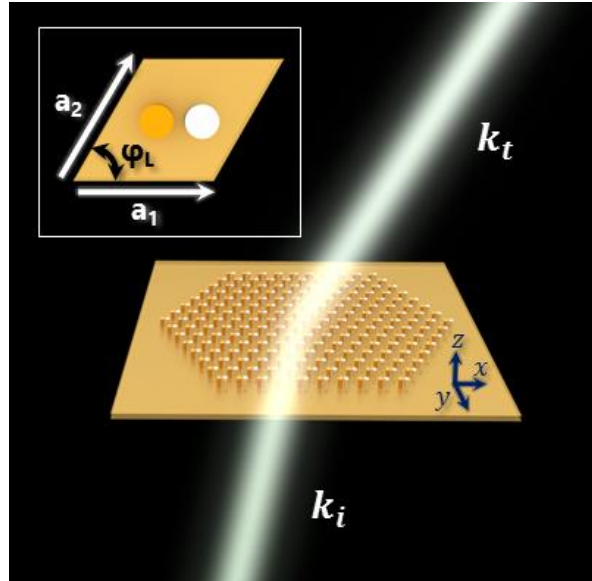
Figure 2.3 Diatomic oblique Bravais lattice. Incident and diffracted wavevectors are denoted by $\boldsymbol{k}_i$ and $\boldsymbol{k}_t$, respectively. The inset shows the unit cell of a generalized oblique Bravais lattice topology.

On the other hand, the normal component of $\boldsymbol{k}_t$ will be provided by $\boldsymbol{k}_{t,\perp} = \sqrt{(k_0 n_2)^2 - \left|\boldsymbol{k}_{t,\|}\right|^2}\,\boldsymbol{z}$ (n_2 - refractive index of the transmission medium, $\left|\boldsymbol{k}_{t,\|}\right|$ - magnitude of vector $\boldsymbol{k}_{t,\|}$). In order to obtain propagating waves, $\boldsymbol{k}_{t,\perp}$ should be a real number. This implies that $(k_0 n_2)^2 \geq \left|\boldsymbol{k}_{t,\|}\right|^2$, which leads to inequality $a_m n^2 + b_m n + c_m \leq 0$, with coefficients a_m, b_m, c_m and discriminant Δ, described by the following relations

$$a_m = \left\{\frac{2\pi}{L_a}\csc(\varphi_L)\right\}^2 \tag{2.5}$$

$$b_m = \frac{4\pi}{L_a}\{k_0 n_1 \sin(\theta_i)\cos(\varphi_i) - k_0 n_1 \sin(\theta_i)\sin(\varphi_i)\cot(\varphi_L)$$

$$-m\frac{2\pi}{L_b}\cot(\varphi_L)\csc(\varphi_L)\} \tag{2.6}$$

$$c_m = -k_0^2 n_2^2 + k_0^2 n_1^2 \sin^2(\theta_i) + m\frac{4\pi}{L_b}k_0 n_1 \sin(\theta_i)\sin(\varphi_i)\csc(\varphi_L)$$

$$+\left(m\frac{2\pi}{L_b}\right)^2 \csc^2(\varphi_L) \tag{2.7}$$

$$\Delta = -4\csc^2(\varphi_L)\left(\frac{2\pi}{L_b}\right)^2\left(\frac{2\pi}{L_a}\right)^2\left\{m - \frac{L_b}{\lambda}\{-n_1\sin(\theta_i)\cos(\varphi_L - \varphi_i) + n_2\}\right\}$$

$$\left\{m - \frac{L_b}{\lambda}\{-n_1\sin(\theta_i)\cos(\varphi_L - \varphi_i) - n_2\}\right\} \tag{2.8}$$

Since $a_m \geq 0$, it should also be true that $\Delta \geq 0$, which yields the following constraints for parameters n, m

$$\left[\frac{L_b}{\lambda}\{-n_1\sin(\theta_i)\cos(\varphi_L-\varphi_i)-n_2\}\right]\leq m\leq\left[\frac{L_b}{\lambda}\{-n_1\sin(\theta_i)\cos(\varphi_L-\varphi_i)+n_2\}\right] \quad \textbf{(2.9)}$$

$$\left[\frac{-b_m-\sqrt{\Delta}}{2\alpha_m}\right]\leq n\leq\left[\frac{-b_m+\sqrt{\Delta}}{2\alpha_m}\right] \quad\quad \textbf{(2.10)}$$

where $[x]$ represents the integer part of real number x. Finally, the elevation and azimuth angles of propagation, corresponding to the free-space mode (n, m), can be computed from $\theta_d = \text{acos}(k_{t,z}/(k_o n_2))$ and $\varphi_d = atan(k_{t,y}/k_{t,x})$, respectively, with $k_{t,x}$, $k_{t,y}$, and $k_{t,z}$ denoting the x-, y-, z-components of $\boldsymbol{k}_t$.

2.3.2 Unidirectional light transport in PT-symmetric oblique Bravais lattices

In this section, we provide both numerical and experimental results, which confirm the angularly unbalanced radiation pattern (see Fig. 2.4), stemming from a PT-symmetric oblique Bravais lattice. The respective irregular honeycomb structure, is depicted in Fig. 2.4c. The unit cell dimensions are described by L_a, L_b, while d, φ_L represent the scatterer center-to-center distance and the lattice angle, respectively. We note that this diffractive arrangement respects both local, as well as global PT symmetry. '

Figure 2.5a depicts a regular honeycomb array of scatterers with $L_a = 3d, L_b = d\sqrt{3}, \varphi_L = 30^0$. Such a configuration is characterized by a perfect hexagonal tiling, which, in turn, dictates an angularly balanced and non-directional far-field radiation pattern (Section 2.3.3). In order to attain directional scattering, certain lattice symmetries need to be progressively broken, as illustrated in Fig. 2.5c. More specifically, we modify the topology of the ABC triangle, formed by the neighboring nanopillars of the two-dimensional (2D) periodic structure. If the network is of the honeycomb type, ABC happens to be equilateral,

14

with its circumcenter (G) occupied by another diffractive element. As a first step in altering the topology of the system, we shift the central cylinder G along the perpendicular bisector of BC. Subsequently, ABC is rescaled and A is relocated, such that $AB = AC \neq BC$. As a result, we obtain an irregular "deformed" honeycomb lattice (Fig. 2.5b), for which $L_a = L_b = L$, $\varphi_L = 60^0$. In this case, the amount of lattice deformation in the final arrangement is determined by both displacements ΔG and ΔA, and as such dictates the imbalance between the propagating modes. In Section 2.3.3, we provide an alternative view of the aforementioned geometric transformations, by starting from a generalized diatomic oblique Bravais unit cell. In doing so, it is shown that in order to achieve radiation directionality, both relations $L_a = 2L_b\cos(\varphi_L)$ and $L_b/\{2dcos(\varphi_L)\} \neq 1$ must be satisfied. The former equality is required for the alignment of the lossy pillars in the y-direction (y-polarized incident electric field), while the latter condition leads to the desired lattice distortion.

Without any loss of generality, the proposed configuration is designed so as to support six distinct diffraction orders at a wavelength of λ_o = 530 nm. For this configuration, the unit cell has dimensions $L_a = L_b$ = 690 nm, $\varphi_L = 60^0$. The diameter of the nanoscatterers is $D =$ 160 nm, while their center-to-center distance is $d =$ 210 nm. Due to the deeply subwavelength gap ($\sim\lambda_o/10$) between the lossy and transparent pillars, their respective coupling strength becomes enhanced, thus leading to a highly asymmetric radiation profile. In order to further increase such near-field interactions, the nanopillars (overall height $h =$ 370 nm) were partially buried at a height of $h_s =$ 90 nm in the polyimide substrate. In all cases, nickel (Ni) [28] was used for realizing the lossy elements, alumina/sapphire (Al_2O_3) [29] for the transparent scatterers, and high-index polyimide [30] for the substrate.

Moreover, it is assumed that the optical field is y-polarized at normal incidence. The propagation direction of the transmitted modes is determined by the elevation and azimuth angles θ_d and φ_d, respectively, which can be analytically computed (see Section 2.3.1).
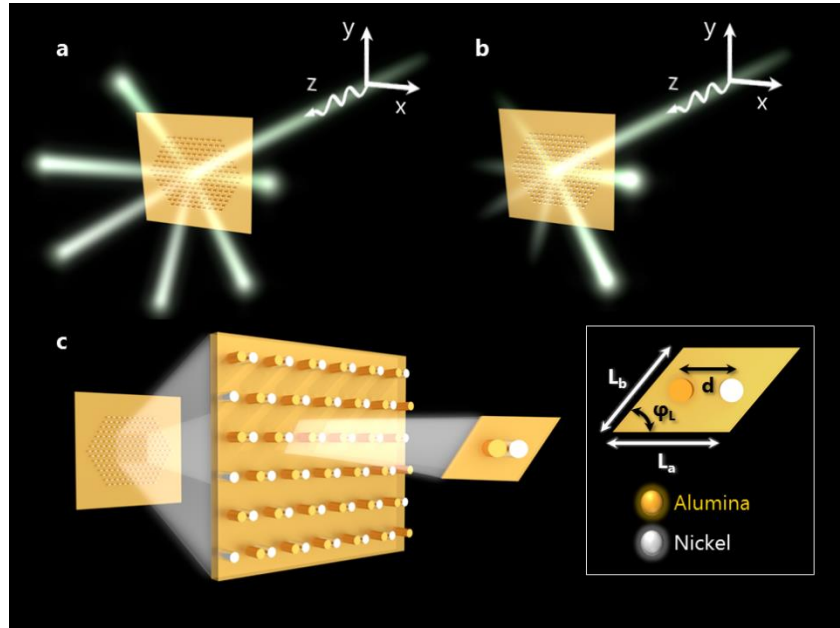
Figure 2.4 Passive PT-symmetric metasurface. a, Symmetric far-field emission in various diffraction modes under Hermitian conditions (alumina nanopillars). b, Lopsided diffraction and loss-induced redistribution of power in favor of desired free-space modes for the PT-symmetric metasurface (involving alumina and nickel nanopillars). c, Schematic illustration of an irregular PT-symmetric photonic honeycomb network. The inset shows the unit cell of a generalized oblique Bravais lattice topology.

Figure 2.5d depicts near-field distribution results along the azimuthal cross-sectional plane at $\varphi = 0^0$, associated with the Hermitian and its corresponding PT-symmetric arrangement, for a wavelength of $\lambda_o = 530$ nm. Numerical simulations were carried out using the COMSOL Multiphysics software, which is based on the finite element method analysis. A single unit cell (see Fig. 2.4c) was analyzed, after applying periodic boundary conditions.

Perfect matching layers (PML) were employed to eliminate any back reflections from the model's boundaries. Periodic ports were used, in order to calculate the efficiencies of the propagating diffraction orders. As excitation field, we assumed a plane wave of the form $E = E_o e^{-jk_x x - jk_y y - jk_z z}$. Moreover, triangular and tetrahedral mesh schemes were utilized for the boundaries and bulk domains, respectively, with mesh element size not exceeding $\lambda/6$.
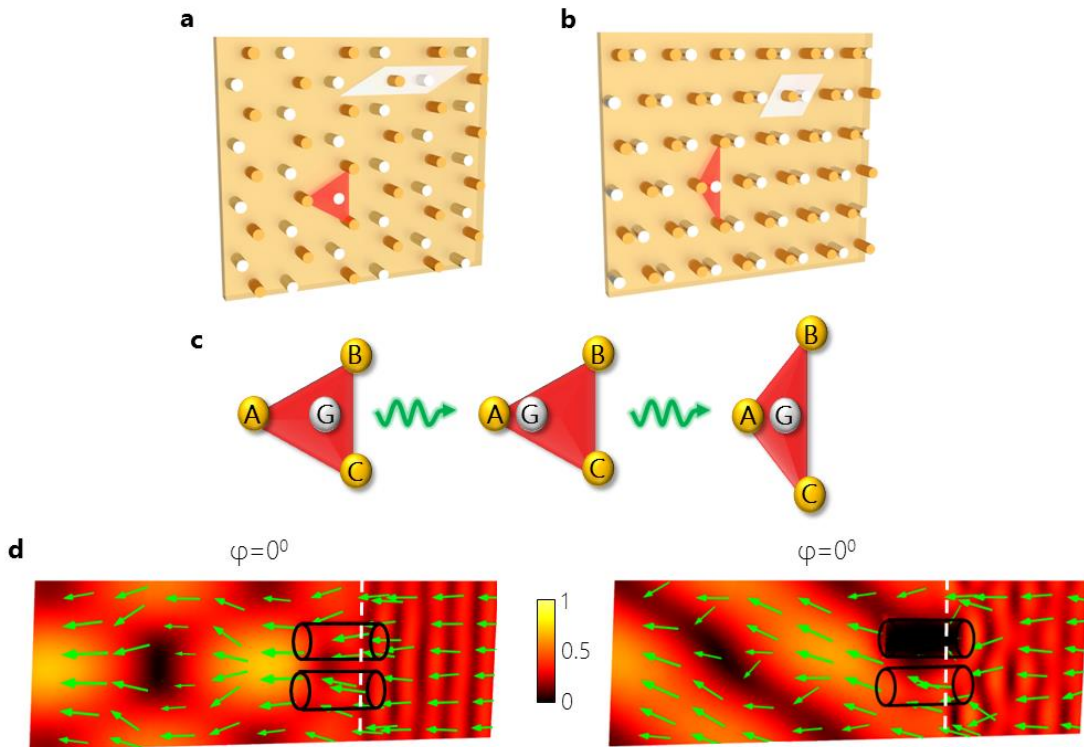
Figure 2.5 Operation principle of PT-symmetric metasurfaces. a, b, Standard (a) and "deformed" (b) honeycomb networks. The respective unit cells (white) and triangles (red) formed by neighboring diffractive elements are also shown. c, Sequential geometric transformations relating the lattices in a and b. Elements A, B, C, indicate the position of lossless sapphire nanopillars, while G denotes lossy nickel elements. d, Near-field results for the Hermitian (left panel) and PT-symmetric (right panel) cases. Arrows indicate the Poynting power density vector flow, while the near-field distributions are depicted along the azimuthal planes $\boldsymbol{\varphi} = 0^0$.

The Poynting vector graphs clearly indicate a reorientation of the average power flow towards the lossy diffractive nanopillars in the PT-symmetric configuration (right panel - Fig. 2.5d), as opposed to the Hermitian case (left panel - Fig. 2.5d). This lopsided emission is attributed to the presence of an additional transverse component in the Poynting vector field, needed to promote energy transfer to the lossy subdomains. In Section 2.3.3, the 2D field distributions along the plane $\varphi = 90^0$ are also provided. In this case, no asymmetry is observed owing to the alignment of the lossy pillars along the y-axis. .

For our study, we fabricated an irregular photonic honeycomb lattice via a double patterning process using standard electron beam (e-beam) lithography techniques (see Section 2.3.5). As a first step, a silica layer was deposited on top of a silicon wafer through plasma-enhanced chemical vapor deposition. Subsequently, the nickel elements (PT-symmetric structure) were patterned, followed by e-beam evaporation and lift-off. The same process was repeated for the alumina nanopillars. The distance between the lossy and transparent surface scatterers was kept at 50 nm through accurate alignment by e-beam lithography. Ultimately, spin-coating of the polyimide was performed, along with dry and wet etching of the silicon substrate and the sacrificial silica layer, respectively. The end result is a flexible Hermitian/PT-symmetric metasurface, as shown in Figs. 2.6a,b. Scanning electron microscope (SEM) images of this irregular hexagonal pattern formation are shown in Figs. 2.6c,d. A summary of the fabrications steps, along with a more detailed analysis of the experimental methods, are provided in Section 2.3.5.
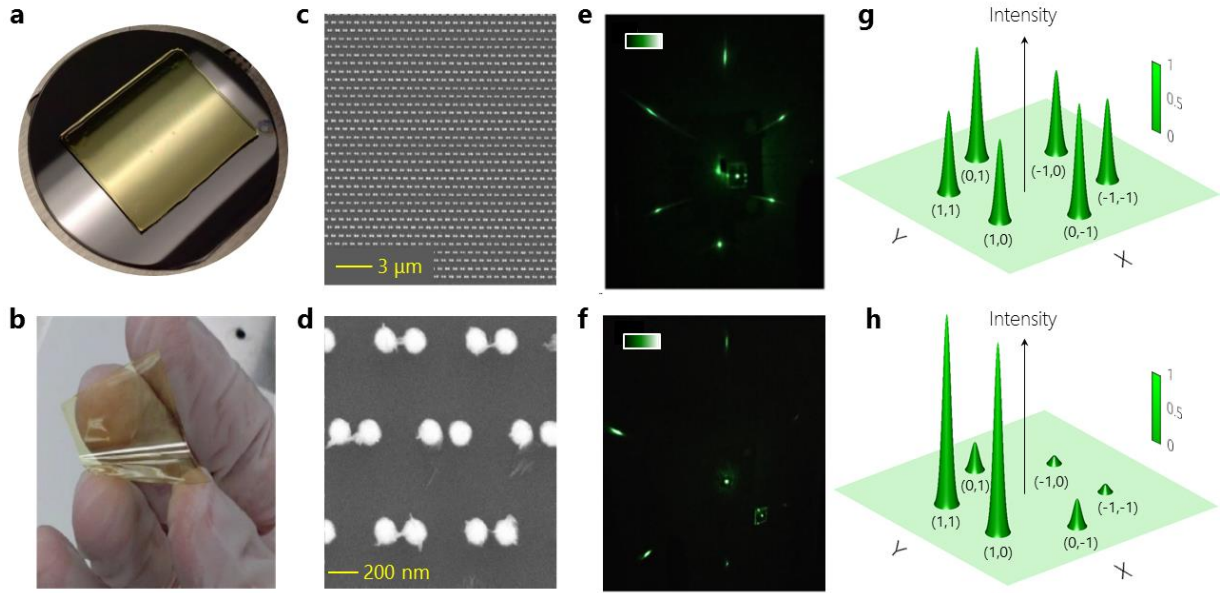
Figure 2.6 Experimental results. a,b, A flexible PT-symmetric metasurface on Si substrate (a) and final sample with Si etched away (b). c,d, Scanning electron microscope images of the irregular hexagonal pattern on the flexible substrate. e,f, Far-field emission under Hermitian (e) and parity-time (f) conditions. g,h, Experimentally measured power diffraction efficiencies for the Hermitian (g) and PT-symmetric (h) configurations.

In order to probe the far-field scattering behavior of these PT-symmetric metasurfaces, we illuminated the samples with a laser beam at 530 nm, after passing through a vertical polarizer, followed by a biconvex lens (Section 2.3.5). The experiment was performed under normal incidence, while the power of the diffracted orders was measured by a power meter. The field directivity of the fabricated samples was quantified by means of an extinction ratio, defined as the ratio between the power efficiencies of the enhanced and attenuated propagating modes. As previously mentioned, the structure supports six higher-order transmission modes with respective azimuth angles $\varphi_d = \pm 30^0, \pm 90^0, \pm 150^0$. In all cases, the elevation angle of propagation is $\theta_d = 62^0$. The obtained results (Figs. 2.6e-h)

19

demonstrate a pronounced asymmetric diffraction, as predicted theoretically. The numerically computed (see Section 2.3.3) and experimentally obtained far-field efficiencies (Figs. 2.6g,h) were found to be in good agreement. More specifically, mode orders (0,1), (0,-1), (-1,0), (-1,-1) are reduced below 1%, while the propagating modes (1,1), (1,0), become significantly enhanced by a factor of $\times$ 2.3, leading to an extinction ratio of 8 dB. Such unidirectional emission indicates a broken PT phase and signifies a clear violation of Friedel's law of diffraction.

2.3.3 Effect of surface topology on near- and far-field transmission

As demonstrated in Section 2.3.2, directive scattering can be attained, after breaking certain symmetries present in a standard honeycomb array. In the present section, we provide an alternative view of such geometric transformations, by considering a generalized oblique Bravais lattice arrangement (see Fig. 2.7a).

As a first step in altering the topology of the system, the lossy nanopillars become aligned along the y direction (Fig. 2.7b). This implies that relation $L_a = 2L_b\cos(\varphi_L)$ should hold true. As a result, we obtain significantly reduced diffraction efficiencies for the transmission modes propagating along the azimuthal planes $\varphi = \pm 90^0$, since the incident field is also y-polarized. In order to attain a standard honeycomb array, the hexagons formed by the neighboring scattering elements should have all their sides and angles equal. The former requirement is met, if relation $L_b = 2d\cos(\varphi_L)$ is satisfied (see Fig. 2.7c). Finally, by also setting $\varphi_L = 30^0$, we obtain a perfect hexagonal tiling with $L_a = 3d$, $L_b = \sqrt{3}d$ (Fig. 2.7d).

For our study, we have utilized the "deformed" honeycomb network of Fig. 2.7b, with $\varphi_L = 60^0$. In this case, condition $L_a = 2L_b cos(\varphi_L)$ implies that the unit cell should have equal sides ($L_a = L_b = L$). Moreover, it will be true that $L_b/(2dcos\varphi_L) = L_a/d > 1$, which leads to an irregular hexagonal pattern formation and, consequently, to directional far-field emission. Figure 2.8 provides near-field distributions, along the azimuthal plane $\varphi = 90^0$, and respective numerically computed far-field power efficiencies, associated with the Hermitian and PT-symmetric metasurfaces studied in the main text ($L_a = L_b = 690$ nm, $\varphi_L = 60^0$, $d = 210$ nm, $D = 160$ nm). The wavelength of operation was assumed to be $\lambda_o = 530$ nm ($n_{Al_2O_3} = 1.77$, $n_{Ni} = 1.77$-3.18i, $n_{polyimide} = 2$).
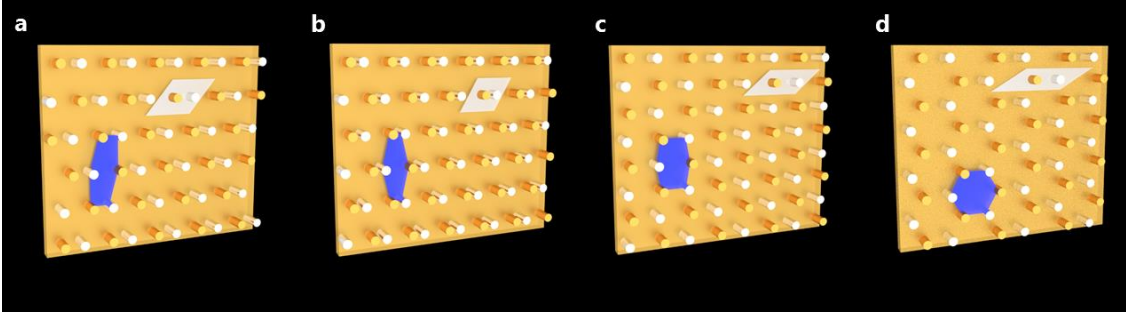
Figure 2.7 Oblique Bravais lattice - geometric transformations. a, Generalized diatomic oblique Bravais lattice. b, Alignment of lossy scatterers, imposed by relation $\boldsymbol{L_a = 2L_b cos(\varphi_L)}$. c,d, Arrangement of nanopillars, such that hexagon cells formed by neighboring diffractive elements have equal sides (c - $\boldsymbol{L_b = 2dcos(\varphi_L)}$) and, subsequently, equal angles (d - $\boldsymbol{\varphi_L = 30^0, L_a = 3d, L_b = \sqrt{3}d}$). The lattice shown in d, corresponds to a standard honeycomb network. In all cases, the respective unit (white) and hexagon (blue) cells, are shown.

For comparison purposes, we provide near-field scattering results, along with numerically computed diffraction efficiencies, for a honeycomb lattice with unit cell

parameters $L_a = 1200$ nm, $L_b = 700$ nm, $\varphi_L = 300$, and $d = 400$ nm (Fig. 2.9). The scatterer diameter is $D = 200$ nm, while the nanopillars (overall height $h = 370$ nm) were once again partially buried at a height of $h_s = 90$ nm in the polyimide substrate. The diffraction arrangement supports six distinct transmission orders at the wavelength of 530 nm, with respective azimuth angles $\varphi_d = 0^0, \pm60^0, \pm120^0, 180^0$. The free-space modes propagate at an elevation angle of $\theta_d = 62^0$. As shown in Fig. 2.9, a loss-induced redistribution of energy in favor of the orders (1,1), (-2,-1), (1,0) is observed. Nevertheless, power flows in an angularly balanced manner, leading to a non-directional far-field emission.
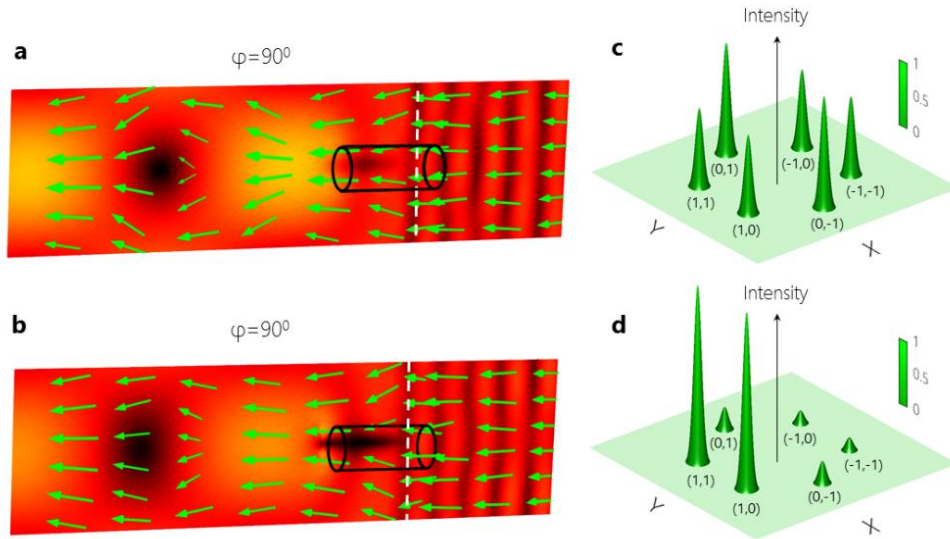
Figure 2.8 "Deformed" honeycomb arrangement - numerical scattering results. a,b, Near-field distributions under Hermitian (a) and parity-time (b) conditions, along the azimuthal planes $\boldsymbol{\varphi} = 90^0$. c,d, Diffraction efficiencies corresponding to the Hermitian (c) and PT-symmetric (d) metasurfaces.
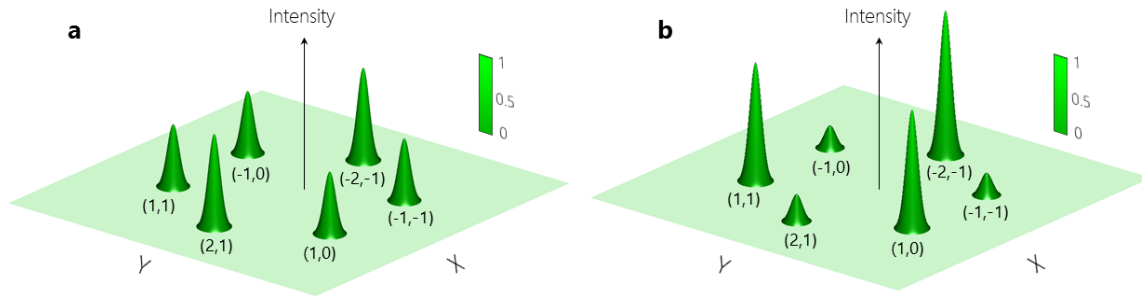
Figure 2.9 Honeycomb lattice - diffraction results. a,b, Numerically computed power diffraction efficiencies for the Hermitian (a) and PT-symmetric metasurfaces (b). The wavelength of operation is assumed to be 532 nm.

2.3.4 Broadband asymmetric light transport

In order to confirm numerically the broadband operation of PT-symmetric metasurfaces, the respective far-field efficiencies were evaluated over the wavelength range 410-590 nm, via finite element simulations. Material dispersion corresponding to the nickel /alumina nanopillars [28,29] and polyimide substrate [30], was also taken into account. The corresponding results (see Fig. 2.10a) indicate a symmetric power distribution between modes (1,1) and (-1,0) for the Hermitian arrangement. On the other hand, under parity-time conditions, diffraction order (1,1) demonstrates higher efficiency than the remaining free-space modes, throughout the spectral range 410-590 nm. This leads to a broadband loss-induced redistribution of energy towards the propagation directions $(\theta_d, \varphi_d) = (62^0, \pm30^0)$. Moreover, the extinction ratio is monotonically increasing with wavelength, reaching up to 15 dB close to 590 nm. Propagating modes (1,0), (0,-1), (-1,-1) are not depicted in Fig. 2.10a,

since they exhibit identical efficiencies with modes (1,1), (0,1), (-1,0), respectively. This is attributed to the underlying symmetry present in an oblique Bravais lattice configuration. In all cases, the structure dimensions and materials were kept the same as in the main text.
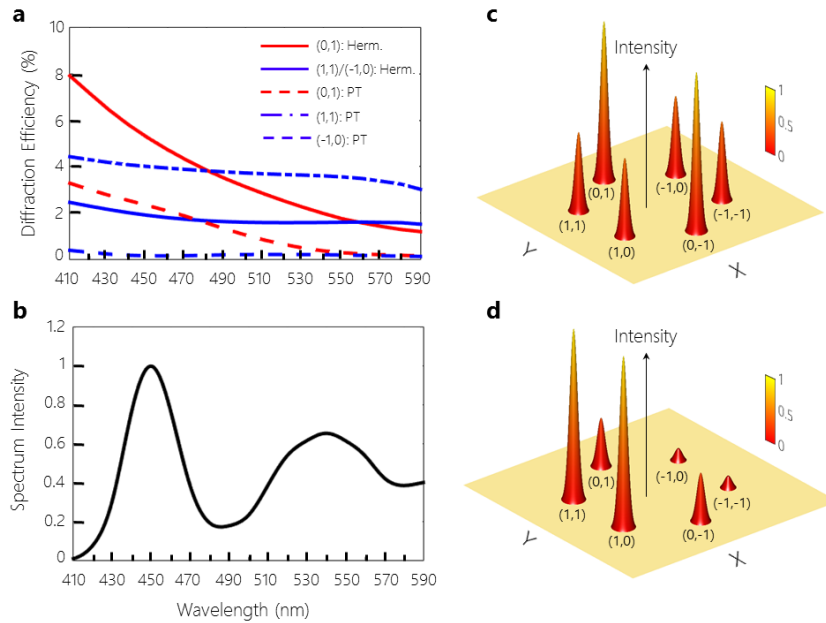
Figure 2.10 Broadband finite element computations. a, Diffraction efficiencies for mode orders (0,1), (1,1), (-1,0) over the wavelength range 410-590 nm, corresponding to both Hermitian (solid lines) and PT-symmetric cases (dashed and dashed-dot lines). b-d, Spectrum efficiency of the broadband white light source used in the experiments (b), along with the respective numerically evaluated power diffraction efficiencies, under Hermitian (c) and parity-time (d) conditions.

Finally, far-field diffraction efficiencies $\overline{DE}_{(n,m)}$, associated with the white light source used in the experiments (see Fig. 2.10b for spectral response), can be attained via the following weighted average expression

$$\overline{DE}_{(n,m)} = \frac{\int_\lambda DE_{(n,m)}(\lambda) \cdot S(\lambda) d\lambda}{\int_\lambda S(\lambda) d\lambda} \tag{2.11}$$

24

where $DE_{(n,m)}(\lambda)$ denotes the diffraction efficiency corresponding to mode order (n,m) at wavelength λ, while $S(\lambda)$ represents the spectrum intensity of the incoherent light source. The corresponding results are shown in Figs. 2.10c,d, for both the Hermitian and PT-symmetric metasurfaces.
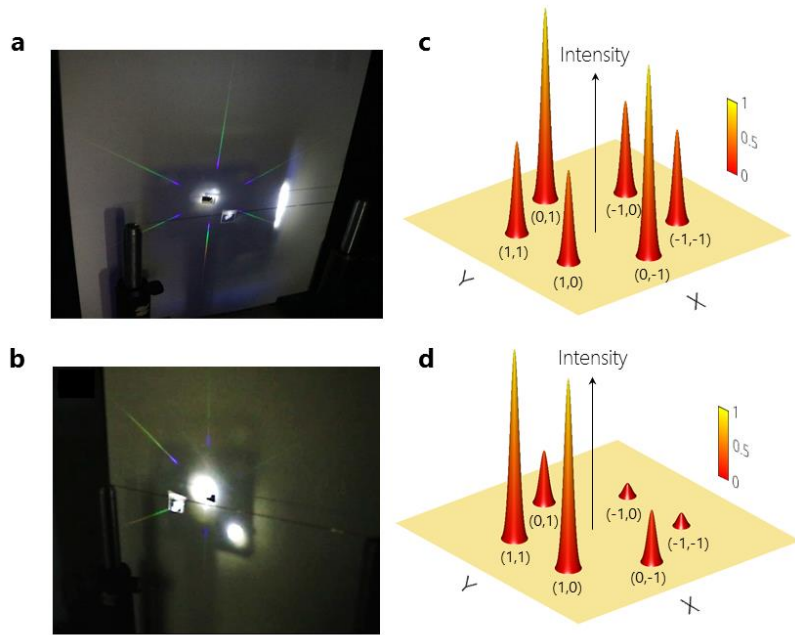
Figure 2.11   Broadband scattering experimental results. a,b, Far-field diffraction patterns under Hermitian (a) and PT conditions (b). c,d, Power diffraction efficiencies, as measured experimentally, for the Hermitian (c) and PT-symmetric (d) metasurfaces.

In order to experimentally demonstrate the unidirectional transmission over a broad range of wavelengths, we illuminated the sample with an incoherent white light source, whose spectral response is shown in Fig. 2.10b. The respective diffraction efficiency results are shown in Fig. 2.11 and indicate a close match between experiments and simulations. More specifically, a suppression of all the free-space modes is evident, besides the desired

25

orders (1,1) and (1,0), with an extinction ratio of 6 dB. We should note that in all cases, the two diffraction orders propagating in the $\varphi = 90^0$ plane, i.e. (0,1), (0,-1), are equally attenuated, owing to the imposed alignment of the lossy nanopillars along the y-direction.

2.3.5 Experimental methods

The fabrication methodology follows the "top-down" approach, while the recipe steps are summarized in Fig. 2.12. As aMore specifically, a layer of silica (SiO_2) with a thickness of 300 nm was deposited on a silicon wafer (2 x 3 cm2) via plasma-enhanced chemical vapor deposition (PECVD). Consequently, the sample was spin-coated with a polymethyl methacrylate (PMMA) 950 A6 film for an additional thickness of 600 – 630 nm, through the following gradual process:

1 – First spin-coating was executed at 500 rounds per minute (rpm) speed with 352 rpm acceleration, for 5 seconds.

2 – Second spin-coating was performed at 4000 rpm speed at 352 rpm acceleration, for 45 seconds. As a result, a uniform PMMA film of 600 – 630 nm thickness (measured using filmometrics) was obtained.

3 – The substrate was baked in the oven at 1800C for 15 hours.
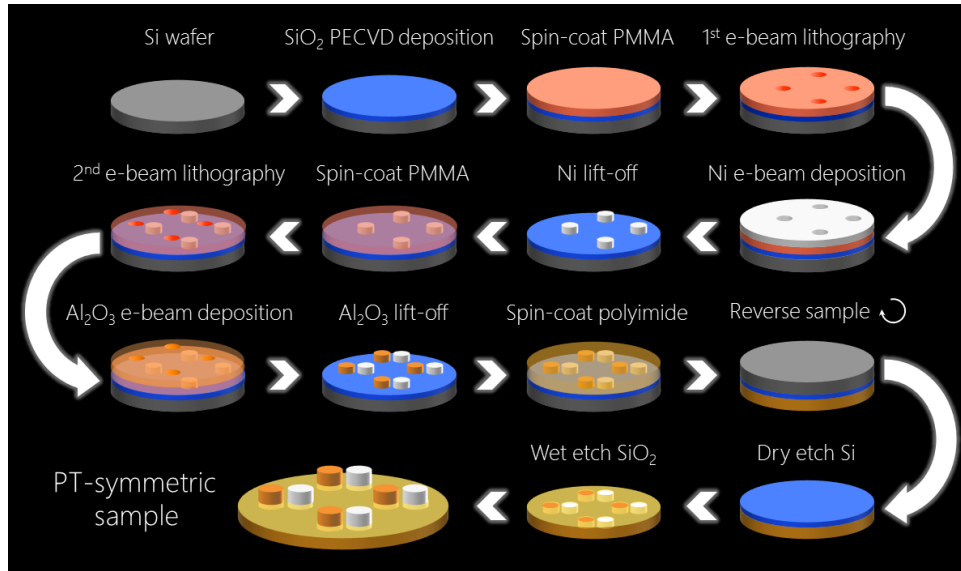
Figure 2.12 Fabrication methodology
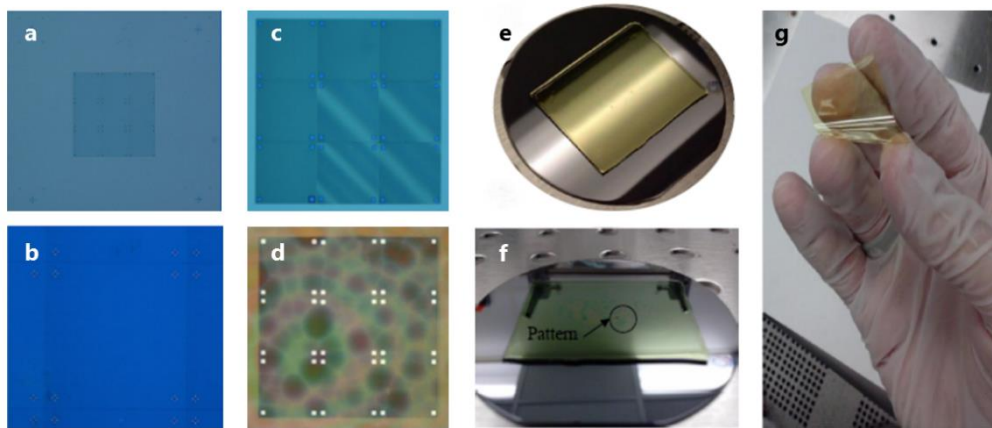
Figure 2.13 PT-symmetric sample. a-d, Images taken under the optical microscope at different stages during the fabrication process: before nickel deposition (a), after Ni lift-off (b), before alumina deposition (c), and final pattern on flexible polymer (d). e-g, Top (e), side (f) profile of the flexible PT-symmetric metasurface on a silicon substrate, and final sample with Si etched away.

The first electron beam (e-beam) lithography step follows. Subsequently, alumina (passive arrangement) or nickel (non-Hermitian configuration) was deposited with a thickness of 370 nm at a rate of 1 Å/sec. Lift-off with acetone was performed, while isopropanol (IPA) was used to remove any residual material. Images taken under the optical microscope are shown in Fig. 2.13, after drying the sample with N_2 gas.

For the PT-symmetric metasurface, an additional e-beam lithography step is required for the patterning of the Al_2O_3 pillars. This involves again spin-coating of a thin PMMA film, followed by e-beam writing at a dosage of 760 $\mu C/cm^2$, using a separation of 80 nm and a size of 110 nm. Alumina was then deposited with a thickness of 370 nm (at 1 Å/sec). During the Al_2O_3 deposition process, the temperature of the chamber increases, thus causing the PMMA to be hardened. Therefore, the polymer is exposed to ultraviolet radiation for 6 min to soften it. After the lift-off process is completed, polyimide is spin-coated on both the passive and PT-symmetric arrangements (1000 rpm speed at 100 rpm acceleration, for 60 seconds), in order to attain a uniform polyimide film of 10 μm thickness. Finally, dry and wet etching (buffer oxide) were both performed, in order to remove the silicon substrate and the silica sacrificial layer, respectively. Figure 2.14 shows scanning electron microscope (SEM) images, which reveal an average nanopillar diameter, scatterer separation, and lattice constant, of 158 nm, 54 nm, and 696 nm, respectively. Finally, the experimental setup is demonstrated in Fig. 1.15. Samples were illuminated independently, by both a laser beam at 532 nm and an incoherent white light source (broadband measurements). Both optical beams pass through a vertical polarizer, followed by a biconvex lens. The power of the diffracted orders was measured by a power meter.
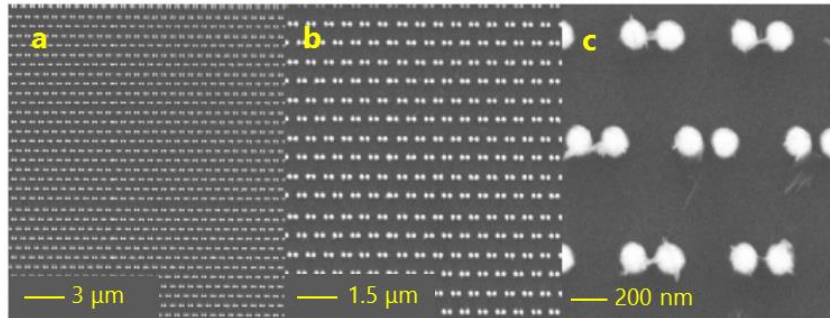
Figure 2.14 Irregular hexagonal pattern formation - SEM images.
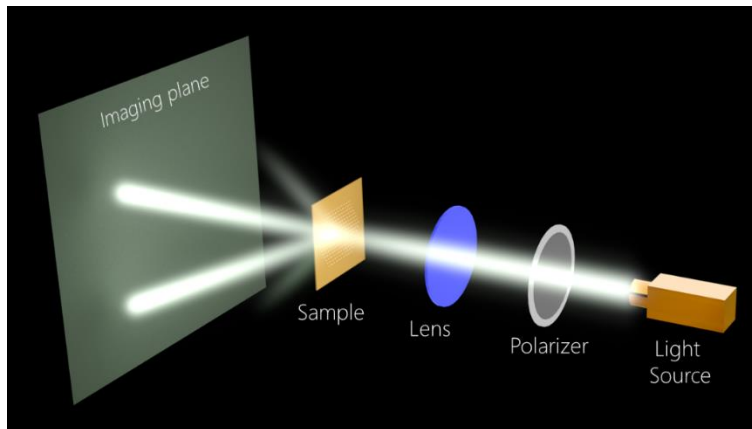
Figure 2.15 Measurement of far-field emission – experimental setup.

2.4 Conclusions

In conclusion, in this work we have shown that flexible PT-symmetric metasurfaces can be employed to significantly enhance or suppress their respective far-field diffraction efficiencies. Passive PT-symmetry was introduced in 1D and 2D oblique diatomic Bravais lattices, through loss elements. The presented methodology can be readily extended to other

wavelength regions (e.g., terahertz, infrared) and physical settings, such as acoustics and microwaves. Moreover, our approach can open up new possibilities in the field of reconfigurable optics, based on materials with controllable properties via external stimuli, such as voltage, temperature, and magnetic fields. Owing to the flexibility of the proposed non-Hermitian structure, additional studies can be made on the propagation dynamics on curved lattice geometries, where relativistic-like effects are expected to take place [31]. Finally, of great interest, would be to investigate the behavior of the proposed non-Hermitian arrangements close to the exceptional point of operation. In this case, not only the eigenvalues, but also the eigenvectors coalesce, leading to extraordinary transmission properties [10]. This will constitute the objective of our future work.

2.5 References

1. N. Yu, P. Genevet, M. A. Kats, F. Aieta, J.-P. Tetienne, F. Capasso, and Z. Gaburro, "Light propagation with phase discontinuities: generalized laws of reflection and refraction," Science **334**, 333–337 (2011).

2. A. V. Kildishev, A. Boltasseva, and V. M. Shalaev, "Planar photonics with metasurfaces," Science **339**, 1232009 (2013).

3. N. Yu and F. Capasso, "Flat optics with designer metasurfaces, " Nat. Mater. **13**, 139–150 (2014).

4. D. Lin, P. Fan, E. Hasman, and M. L. Brongersma, "Dielectric gradient metasurface optical elements," Science **345**, 298-302 (2014).

5. X. Ni, N. K. Emani, A. V. Kildishev , A. Boltasseva, and V. M. Shalaev, "Broadband light bending with plasmonic nanoantennas," Science **335**, 427 (2012).

6. Y. Yang, W. Wang, P. Moitra, I. I. Kravchenko, D. P. Briggs, and J. P. Valentine, "Dielectric meta-reflectarray for broadband linear polarization conversion and optical vortex generation, " Nano Lett. **14**, 1394-1399 (2014).

7. T. Guo and C. Argyropoulos, "Broadband polarizers based on graphene metasurfaces, " Opt. Lett. **41**, 5592-5595 (2016).

8. S. Boroviks, R. A. Deshpande, N. A. Mortensen, and S. I. Bozhevolnyi, "Multifunctional metamirror: polarization splitting and focusing, " ACS Photonics **5**, 1648-1653 (2017).

9. C. M. Bender and S. Boettcher, "Real spectra in non-Hermitian Hamiltonians having PT Symmetry, " Phys. Rev. Lett. **80**, 5243–5246 (1998).

10. R. El-Ganainy, K. G. Makris, M. Khajavikhan, Z. H. Musslimani, S. Rotter, and D. N. Christodoulides, "Non-Hermitian physics and PT symmetry," Nat. Phys. **14**, 11-19 (2018).

11. T. Kottos, "Optical physics: Broken symmetry makes light work, " Nat. Phys. **6**, 166–167 (2010).

12. G. Castaldi, S. Savoia, V. Galdi, A. Alu, and N. Engheta, "PT metamaterials via complex-coordinate transformation optics, " Phys. Rev. Lett. **110**, 173901 (2013).

13. C. E. Ruter, K. G. Makris, R. El-Ganainy, D. N. Christdoulides, M. Segev, and D. Kip, "Observation of parity-time symmetry in optics," Nat. Phys. **6**, 192–195 (2010).

14. A. Guo, G. J. Salamo, D. Duchesne, R. Morandotti, M. Volatier-Ravat, V. Aimez, G. A. Siviloglou, and D. N. Christodoulides, "Observation of PT-symmetry breaking in complex optical potentials, " Phys. Rev. Lett. **103**, 093902 (2009).

15. L. Feng, Y.-L. Xu, W. S. Fegadolli, M.-H. Lu, J. E. B. Oliveira, V. R. Almeida, Y.-F. Chen, and A. Scherer, "Experimental demonstration of a unidirectional reflectionless parity-time metamaterial at optical frequencies, " Nat. Mater. **12**, 108-113 (2013).

16. B. Zhen, C. W. Hsu, Y. Iqarashi, L. Lu, I. Kaminer, A. Pick, S.-L. Chua, J. D. Joannopoulos, and M. Soljacic, "Spawning rings of exceptional points out of Dirac cones, " Nature **525**, 354-358 (2015).

17. B. Peng, S. K. Ozdemir, F. Lei, F. Monfi, M. Gianfreda, G. L. Long, S. Fan, F. Nori, C. M. Bender, and L. Yang, "Parity–time-symmetric whispering-gallery microcavities, " Nat. Phys. **10**, 394-398 (2014).

18. K. G. Makris, A. Brandstötter, P. Ambichl, Z. H. Musslimani, and S. Rotter, "Wave propagation through disordered media without backscattering and intensity variations, " Light Sci. Appl. **6**, e17035 (2017).

19. M. V. Berry, "Lop-sided diffraction by absorbing crystals," J. Phys. A **31**, 3493–3502 (1998).

20. M. Kulishov and B. Kress, "Free space diffraction on active gratings with balanced phase and gain/loss modulations, " Opt. Express **20**, 29319-29328 (2012).

21. D. L. Sounas, R. Fleury, and A. Alù, "Unidirectional cloaking based on metasurfaces with balanced loss and gain, " Phys. Rev. Appl. **4**, 014005 (2015).

22. R. Fleury, D. L Sounas, and A. Alù, "Negative refraction and planar focusing based on parity-time symmetric metasurfaces, " Phys. Rev. Lett. **113**, 023903 (2014).

23. S. Xiao, J. Gear, S. Rotter, and J. Li, "Effective PT-symmetric metasurfaces for subwavelength amplified sensing," New J. Phys. **18**, 085004 (2016).

24. Y. Jia, Y. Yan, S. V. Kesava, E. D. Gomez, and N. C. Giebink, "Passive parity-time symmetry in organic thin film waveguides, " ACS Photonics **2**, 319-325 (2015).

25. C. Hahn, Y. Choi, J. W. Yoon, S. H. Song, C. H. Oh, and P. Beriniet, "Observation of exceptional points in reconfigurable non-Hermitian vector-field holographic lattices," Nat. Commun. **7**, 12201 (2016).

26. R. Birabassov, A. Yesayan, and T. V. Galstyan, "Nonreciprocal diffraction by spatial modulation of absorption and refraction," Opt. Lett. **24**, 1669-1671 (1999).

27. C. Keller, M. K. Oberthaler, R. Abfalterer, S. Bernet, J. Schmiedmayer, and A. Zeilinger, "Tailored complex potentials and Friedel's law in atom optics," Phys. Rev. Lett. **79**, 3327-3330 (1997).

28. A. D. Rakić, A. B. Djurišić, J. M. Elazar, and M. L. Majewski, "Optical properties of metallic films for vertical-cavity optoelectronic devices," Appl. Opt. **37**, 5271-5283 (1998).

29. I. H. Malitson and M. J. Dodge, "Refractive index and birefringence of synthetic sapphire," J. Opt. Soc. Am. **62**, 1405 (1972).

30. H. W. Su and W. C. Chen, "High refractive index polyimide–nanocrystalline-titania hybrid optical materials," J. Mater. Chem. **18**, 1139-1145. (2008).

31. V. H. Schultheiss, S. Batz, A. Szameit, F. Dreisow, S. Nolte, A. Tunnermann, S. Longhi, and U. Peschel, "Optics in curved space," Phys. Rev. Lett. **105**, 143901 (2010).

32. H. H. Li, "Refractive index of silicon and germanium and its wavelength and temperature derivatives," J. Phys. Chem. Ref. Data **9**, 561–658 (1980).

33. N. S. Nye, A. El-Halawany, A. Bakry, M. A. N. Razvi, A. Alshahrie, M. Khajavikhan, and D. N. Christodoulides. "Passive PT-symmetric metasurfaces with directional field scattering characteristics," IEEE J. Sel. Top. Quantum Electron **22**, 107-114 (2016).

CHAPTER 3: SUPERSYMMETRIC LASER ARRAYS

3.1 Introduction

Symmetries play a fundamental role in physical sciences. Symmetry principles ensure energy and momentum conservation and dictate the allowable dynamical laws governing our world. The Lorentz invariance embodied in Maxwell's equations was crucial in developing the theory of relativity, while the exchange symmetry allows one to classify fundamental particles as either bosons or fermions. In high-energy physics, other overarching symmetries like that of charge-parity-time (CPT) and supersymmetry (SUSY) have also emerged as a means to unveil the laws of nature [1,2]. SUSY, first proposed within the context of particle physics as an extension of the Poincare space-time symmetry, makes an ambitious attempt to provide a unified description of all fundamental interactions. In general, SUSY relates bosonic and fermionic degrees of freedom in a cohesive fashion. This directly implies that each type of boson has a supersymmetric counterpart, a superpartner fermion, and vice versa [3]. Even though the full ramification of SUSY in high energy physics is still a matter of debate that awaits experimental validation, supersymmetric techniques have already found their way into low energy physics, condensed matter, statistical mechanics, nonlinear dynamics and soliton theory as well as in stochastic processes and BCS-type theories, to mention a few [4-9].

Shortly after the discovery of semiconductor lasers, it was recognized that integrated arrays of such emitters may provide a viable avenue in scaling up the radiance (power per unit area per unit solid angle), without running into complications arising from

nonlinearities and filamentation in broad area devices [10]. Unfortunately, however, such arrays tend to support multiple spatial modes (supermodes), an undesirable behavior that in turn degrades the quality of the emitted beam. This has since fueled a flurry of activities in search of strategies that enable the generation of high power and diffraction-limited coherent beams by enforcing the coupled laser array to operate in the fundamental (in-phase) mode. In this regard, several schemes have been developed using for example resonant leaky-wave coupling in antiguided arrangements [11], spatial filtering [12], Talbot effects[13], to name a few [14-16]. Of interest will be to devise fully integrated global approaches that apply to any type of active arrays in order to enforce single-mode lasing in the fundamental transverse supermode. To address this issue, here we report the first realization of a supersymmetric laser array [30]. This lattice emits in its fundamental mode in a stable fashion, as evidenced from far-field and spectral measurements. In this SUSY arrangement, the main array is paired with a lossy superpartner, whose role is to suppress all undesired higher-order modes while at the same time enhancing the gain seen by the fundamental supermode of the primary lattice. In implementing such lasers, we made use of the SUSY formalism first proposed by Witten [17].

3.2 Theoretical Analysis of Supersymmetric Optical Structures

Within the context of non-relativistic quantum mechanics, supersymmetric isospectrality can be established provided that the Hamiltonian of the system, $H^{(1)}$, is factorized in terms of two operators A and $A^\dagger$, i.e. $H^{(1)} = A^\dagger A$ [5]. Similarly, a superpartner

Hamiltonian $H^{(2)}$ can be constructed via $H^{(2)} = A A^\dagger$ by exchanging the action of these two operators. If one now assumes that $|\varphi\rangle^{(1)}$ represents an eigenstate of $H^{(1)}$ with an eigenvalue $\lambda^{(1)}$, i.e. $H^{(1)}|\varphi\rangle^{(1)} = A^\dagger A|\varphi\rangle^{(1)} = \lambda^{(1)}|\varphi\rangle^{(1)}$, then it follows that $AH^{(1)}|\varphi\rangle^{(1)} = (A A^\dagger)A|\varphi\rangle^{(1)} = H^{(2)}A|\varphi\rangle^{(1)} = \lambda^{(1)}A|\varphi\rangle^{(1)}$. Hence, $A|\varphi\rangle^{(1)}$ is an eigenvector of $H^{(2)}$ with an eigenvalue $\lambda^{(1)}$. This immediately indicates that the two Hamiltonians are isospectral since they exhibit identical eigenenergies, i.e. $\lambda^{(2)} = \lambda^{(1)}$, while their eigenstates can be pairwise converted into one another through the action of the A, $A^\dagger$ operators: $|\varphi\rangle^{(2)} = A|\varphi\rangle^{(1)}$ and $|\varphi\rangle^{(1)} = A^\dagger|\varphi\rangle^{(2)}$. If the ground state of $H^{(1)}$ is annihilated by the action of the operator A, then the eigenenergy associated with the ground state of $H^{(1)}$ is zero, and therefore it will not have a corresponding state in $H^{(2)}$. In other words, all the eigenvalues associated with the states of $H^{(1)}$ and $H^{(2)}$ are exactly matched except for the lowest energy state of $H^{(1)}$. When this is the case, then the SUSY is called unbroken. Otherwise, if the ground state of $H^{(1)}$ has a counterpart in its superpartner $H^{(2)}$ with the same eigenvalue, the supersymmetry is broken. Using this approach in 1D Schrödinger problems, one can always identify two SUSY potential functions, $V^{(1)}(x)$ and the superpartner $V^{(2)}(x)$, that are entirely isospectral except for the lowest energy state of $V^{(1)}$ (Fig. 3.1A) [5]. In optics, SUSY can be introduced by exploiting the mathematical isomorphism between the Schrödinger and the optical wave equation [18]. In this setting, the optical refractive index profile plays the role of the potential $V(x)$, which in the context of supersymmetry can be used for mode conversion [19,20] and transformation optics [21], design of Bragg gratings [22], and Bloch-like waves in random-walk potentials [23], to mention a few [24- 26]. However, the

implications of SUSY isospectrality in active platforms, as well as its interplay with nonlinearity and non-Hermiticity has so far remained unexplored. Here we lay the groundwork for such studies by demonstrating a SUSY-based laser.

Figure 3.1B depicts a schematic of the proposed supersymmetric laser. The primary array in this SUSY arrangement is synthesized by coupling five identical ridge-waveguide cavities of length L. The individual waveguide elements are designed to support only the lowest order transverse mode (TE_0). Consequently, each element on its own, is expected to support resonances at angular frequencies $\omega_m = m\pi c/(L n_g)$, where n_g represents the effective group index associated with the TE_0 mode. The evanescent coupling between the five cavities, causes every such resonance frequency ω_m to split into a cluster of five frequencies, corresponding to the five supermodes of the active array. Optical supersymmetric strategies are then employed to build a superpartner index profile that has propagation eigenvalues that match those of the four higher-order supermodes associated with the main (primary) array [27].

In the present analysis, we assume a primary array consisting of five single element ridge waveguide cavities with widths of $1000\ nm$ and a gap of $400\ nm$ in between (Fig. 3.2A). To design the SUSY partner, the Hamiltonian of the primary lattice is discretized into a $N \times N$ tridiagonal matrix. The elements of this matrix are given by $H_{n,n}^{(1)} = \lambda_s$ and $H_{n,n+1}^{(1)} = H_{n+1,n}^{(1)} = k$, where λ_s is the eigenvalue (effective index) of the single element laser constructing the main array and k is the coupling constant of the two adjacent single cavities. The Hamiltonian of the superpartner array is then obtained by $H^{(2)} = (RQ + \lambda_0 I)_{(N-1)} =$

$(Q^T H^{(1)} Q)_{(N-1)}$ in which λ_0 is the eigenenergy of the fundamental mode of the main array, I is the identity matrix of dimensions $N \times N$, and Q and R are the QR factorization matrices of $H^{(1)} - \lambda_1 I$ [18,19,29] Here, the subscript $(N-1)$ means that $H^{(2)}$ is built by only choosing the upper-left block diagonal matrix having the dimensions $(N-1) \times (N-1)$. Finally, the SUSY laser configuration is realized by evanescently coupling the main and the auxiliary arrays. A schematic of the SUSY laser array and the dimensions of its various parts is depicted in Fig. 3.2A.
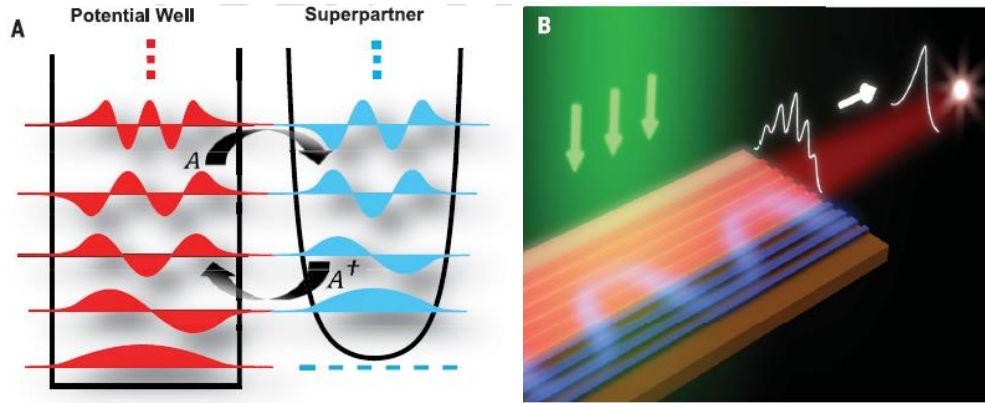
Figure 3.1 Operation principle of SUSY laser array. (A) An infinite potential well and its superpartner in the unbroken SUSY regime. Apart from the ground state, all the eigenvalues of the primary potential are exactly matched to those of the superpartner. The eigenfunctions of the primary potential and its supersymmetric counterpart are transformed into one another through the action of the operators A and $A^\dagger$. (B) A schematic representation of a SUSY laser array involving a primary active lattice (red) coupled to its lossy superpartner (blue). The SUSY laser emits exclusively in the fundamental in-phase mode.

The simulated eigenmodes of the main array and the superpartner, before coupling to each other are depicted in Figs. 3.2B & C. In these simulations, two-dimensional finite element numerical method is employed to acquire the eigenstates supported by each array. The refractive index of InP and InGaAsP in the simulations are considered to be 3.4 and 3.14, respectively. The simulations are performed by eigenfrequency analysis module in COMSOL Multiphysics package.
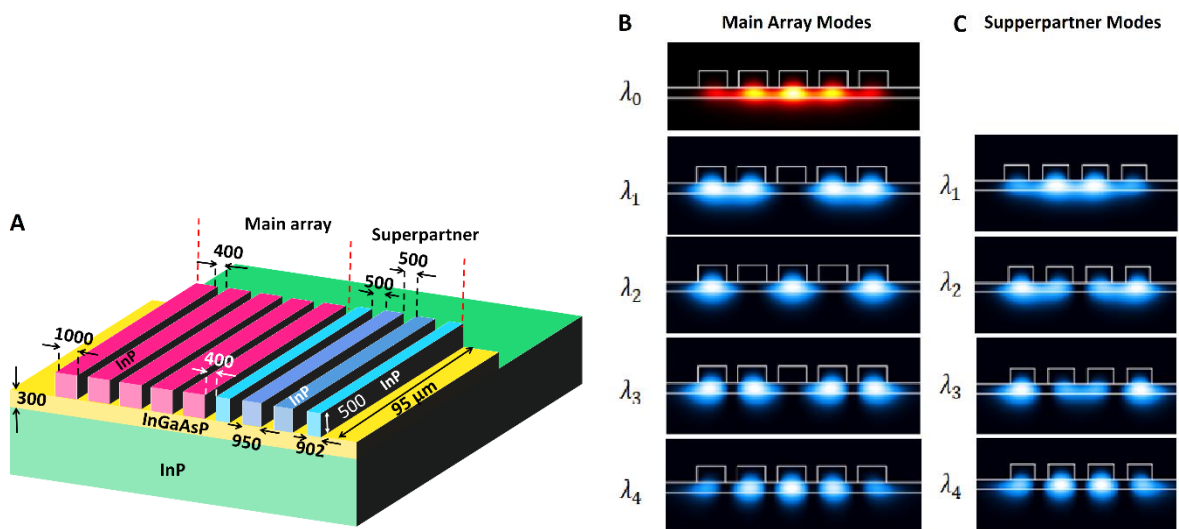
Figure 3.2 Design of the SUSY laser. (A) Schematic representation of the designed SUSY laser. The main array consists of identical waveguides with a 400 nm gap between them. (B) The intensity of the modes of the primary array, obtained by FEM simulations. (C) The intensity of the modes of the superpartner structure, obtained from FEM simulation. The four higher order eigenvalues, λ_1 to λ_4, of the main array are pairwise matched to the eigenvalues of superpartner array.

3.3 Single-mode lasing via SUSY laser arrays

The SUSY laser arrays were realized on an InP wafer with InGaAsP quantum wells as the gain material. In doing so, we used electron beam lithography and plasma etching techniques to define the structures (see Section 3.4). Figure 3.3A displays a scanning electron microscopy (SEM) image of the fabricated SUSY structures. Finite element method (FEM) simulations were performed to determine the modal content of these structures and to determine the level of gain-loss contrast required to suppress the higher order modes, as described in Section 3.2 Figure 3.3B depicts the intensity profiles of all the modes supported by this SUSY configuration. The performance of the SUSY laser was then assessed by means of a custom-made optical setup (see Section 3.4). The arrays are optically pumped at a wavelength of 1064 nm, emitted from a fiber laser. Spatial masks are deployed to selectively pump different regions. The coherent radiation (centered around 1450 nm) emerging from the cleaved facets of the lasers is monitored by both a spectrometer and an infrared camera, after blocking remnants of the pump emission by means of a notch filter. The diffraction angles associated with the far-field emissions along the laser's slow axis, were determined by raster scanning a rectangular aperture placed in front of the array. In every step, the total emitted power from the laser was also measured by a photodiode.
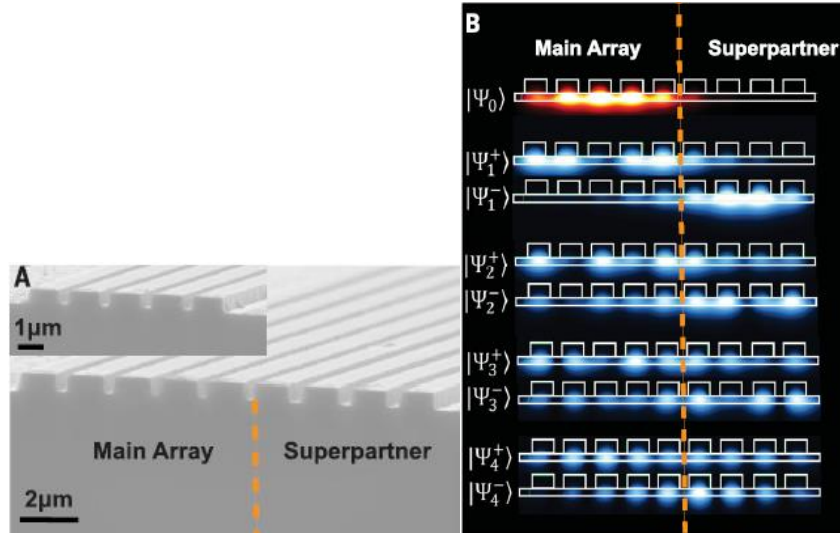
Figure 3.3 A scanning electron microscope image (SEM) and modal field profiles of the SUSY laser array. (A) SEM image of a fabricated SUSY lattice comprised of a five-element primary array, positioned in close proximity ($\sim 400\ nm$) to a four-element superpartner. The inset shows a stand-alone five-element laser array. (B) Intensity distributions associated with the eigenmodes supported by the SUSY arrangement, as obtained from numerical simulations. The fundamental mode of the five-element laser is only confined in the main array, while all the higher-order modes are coupled to the superpartner. The dashed line illustrates the boundary between the main and the superpartner array.

The spectral response, far-field emission, and light-light characteristics are compared for three different configurations: (i) a single ridge waveguide lasing element, (ii) a laser array involving five evanescently coupled ridge cavities, and (iii) a SUSY laser array comprised of a primary active five-element lattice and its corresponding four-element lossy superpartner. In the latter configuration, the two lattices are fabricated in a close proximity to each other and are therefore coupled. The system is judiciously designed so as SUSY is unbroken. This was achieved by appropriately varying the widths (or effective refractive indices) of the ridge elements in the superpartner array. The schematic representations of

these three lasers are provided in the insets of Figs. 3.4A, C, and E, respectively. The lasers are uniformly pumped at an average power density level that is approximately 4 times the threshold. Loss is introduced in the superpartner array by blocking the pump beam using a knife-edge. Under these pumping conditions, the single element cavity lases in a few longitudinal modes (in the TE_0 mode), at wavelengths around 1443 nm (Fig. 3.4A). When the five-element laser array is exposed to the same pump power density, we found that each longitudinal mode now splits into five lines corresponding to the resonances of the five supermodes involved (Fig. 3.4C). This multimode operation leads to a significant deterioration in the beam quality emitted by such a lattice. In contrast, when the SUSY laser array is illuminated at the same pump intensity level (-while the superpartner is blocked), the device emits in a single transverse supermode (Fig. 3.4E). Moreover, the peak intensity produced by this SUSY laser is now 4.2 times higher than that from the standard laser array (i.e. without superpartner), and 8.5 times larger than that from the single element laser. These results clearly indicate that in a SUSY laser arrangement, all higher-order transverse modes are indeed suppressed in favor of the fundamental mode.

To further verify the anticipated SUSY response, the far-field radiation from these three laser systems was collected along with the diffraction profiles in the direction of the slow axis (parallel to the wafer). These measurements are correspondingly displayed in Figs. 3.4B, D, and F. A comparison between these three radiation patterns reveals a striking difference in the way a SUSY laser operates. As opposed to the standard laser array, whose far-field exhibits a multi-lobe profile with a diffraction angle of 19° (Fig. 3.4D), the far-field of the SUSY array presents a single bright spot having instead a much smaller divergence

angle of ~5.8° (Fig. 3.4F). This small-diverging radiance is a characteristic attribute of a laser array operating only in its in-phase lowest-order mode [28]. In addition, in the standard array system, we observe a multi-lobe far-field pattern that changes with pump intensity (see Section 3.4). On the other hand, the beam spot size associated with the SUSY laser is narrower than that of a single laser eleme-nt (12°) as shown in Fig. 3.4B - indicating a higher brightness associated with the SUSY arrangement. The experimentally obtained diffraction patterns are in good agreement with numerical, as demonstrated in Section 3.4.

The light-light curves corresponding to these three lasers and the evolution of their spectra are also depicted in Figs. 3.5A and B, respectively. As expected, both SUSY and standard laser arrays outperform the single element laser in terms of output power (Figure 3.5A). When the overall output power is compared, the two arrays (standard and SUSY) were found to exhibit similar thresholds and slope efficiencies. On the other hand, Fig. 3.5B provides valuable information as to the lasing onset for higher-order supermodes. More specifically, as the pump power is gradually increased above the threshold, the higher-order modes of the standard laser array start to successively emerge in the spectrum (blue lines in Fig. 3.5B), while the SUSY array still lases in its fundamental transverse mode with larger spectral peaks (red lines in Fig. 3.5B). These observations further confirm that indeed in SUSY laser, all undesired higher-order modes are effectively eliminated via coupling to the lossy superpartner- giving the opportunity to the fundamental mode to prevail.
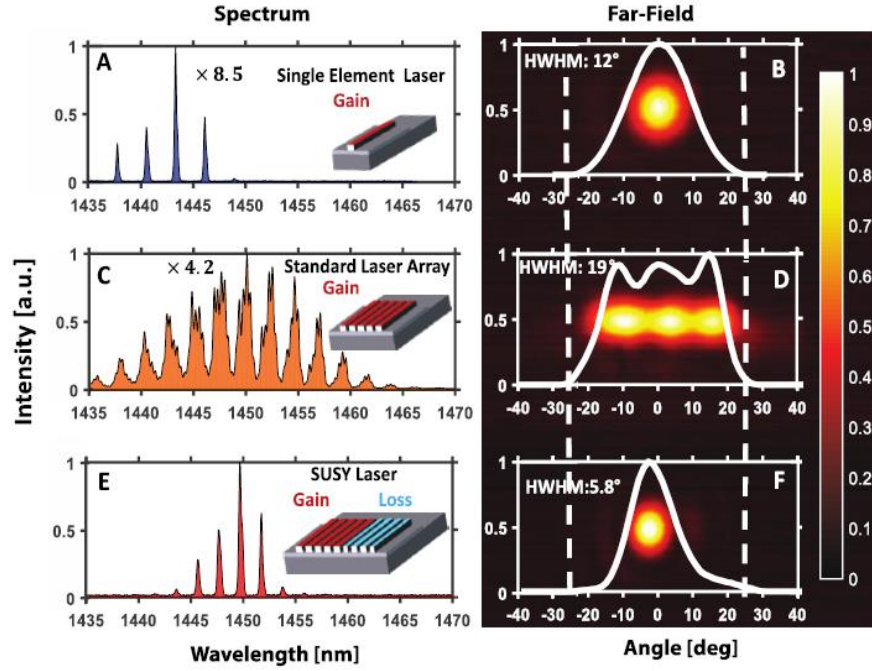
Figure 3.4 Spectral and far-field characteristics of the SUSY laser array. Emission spectrum of a (A) single laser cavity, (C) standard five-element laser array, and (E) corresponding SUSY laser arrangement. The vertical axes are normalized to the spectrum of the SUSY laser. Each longitudinal resonant frequency, in the spectrum of the standard array splits into fine lines- corresponding to the five transverse supermodes. In contrast, the spectrum of the SUSY array is free from such undesired resonances, indicating that all higher order modes are suppressed. (B, D, F) Far-field diffraction patterns from the corresponding lasers. The measured diffraction angle associated with the SUSY laser ($\sim 5.8°$) is smaller than that of the standard laser array ($\sim 19°$) and single cavity laser ($\sim 12°$).

The single transverse mode operation of the SUSY arrangement shows some level of resilience to first-order perturbations and fabrication errors. In order to assess the tolerance of the designed SUSY arrangement to fabrication imperfections, a sensitivity analysis was performed on the superpartner array. Assuming a perturbing Hamiltonian V, the final system can be described by $H_p^{(2)} = H^{(2)} + \varepsilon V$, where ε represents the strength of perturbation. To first order, the original eigenvalues $\lambda^{(2)}$ are perturbed according to $\Delta\lambda^{(2)} =$

45

$\lambda_p^{(2)} - \lambda^{(2)} = \varepsilon < \varphi^{(2)}|V|\varphi^{(2)} >$. In the absence of degeneracies, the higher-order terms in the power expansion of $\lambda_p^{(2)}$ can be neglected. Based on the numerically computed eigenmodes $|\varphi^{(2)}\rangle$ (Fig. 3.3B), we have directly calculated parameter $\Delta\lambda^{(2)}$ for an ensemble of different Hamiltonian implementations V. These include both random diagonal and off diagonal perturbations, due to either fabrication errors or nonlinearly induced detunings.
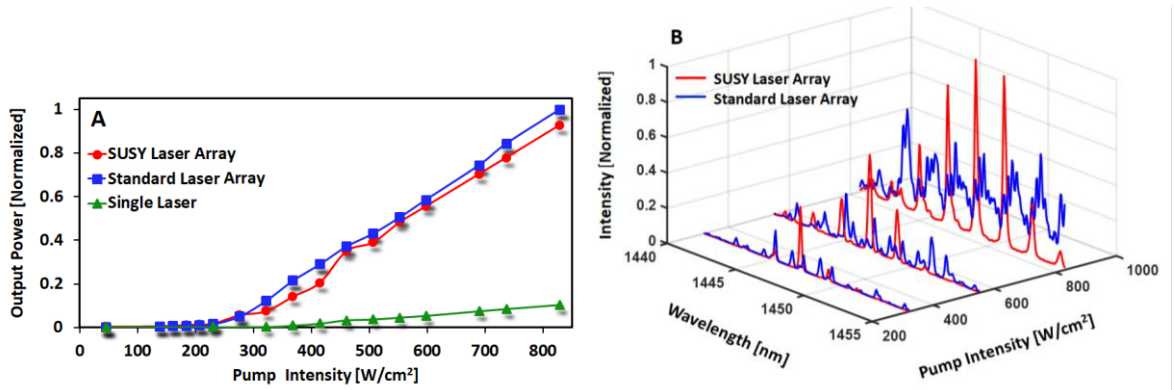
Figure 3.5 Emission characteristics. (A) The light-light curves corresponding to a single laser element (green line), a five-element laser array (blue line), and the SUSY laser arrangement (red line). The output power and slope efficiency of the standard array and the SUSY laser are comparable, and exceed that from a single cavity laser. (B) The spectral evolution behaviors of the standard and SUSY lasers are compared. The standard laser array (blue line) is highly multimoded even slightly above threshold, while the SUSY laser array remains transversely single-moded at much higher pump levels.

The resulting angular histogram (see Fig. 3.6) clearly indicates that the slopes $\langle \varphi^{(2)}|V|\varphi^{(2)}\rangle$ do not exceed 450 and are mostly concentrated in a region of ±150 $(\tan(15^0) = 0.27)$ around the ε-axis. The higher-order modes exhibit even less sensitivity to dimension variations, owing to their weaker confinement in the original array. This implies that the applied supersymmetric transformation method can be considered robust against first-order perturbation defects.
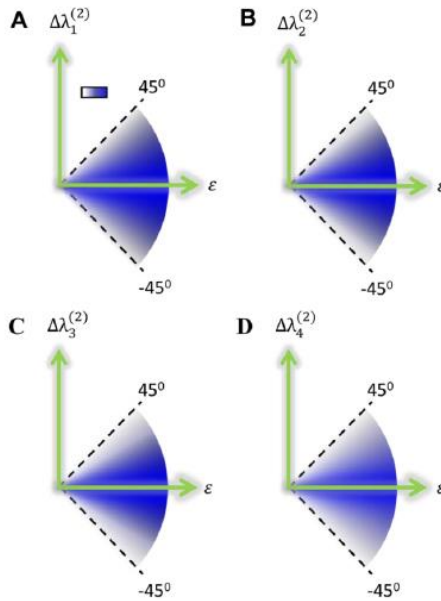
Figure 3.6 First-order perturbation analysis results. Angular histograms of the variations in the normalized propagation constants $\Delta\lambda_i^{(2)}$ are shown, for perturbations of order ε in both onsite and off-diagonal elements in the superpartner array for (A) mode #1, $\Delta\lambda_1^{(2)}$, (B) mode #2, $\Delta\lambda_2^{(2)}$,(C) mode #3 $\Delta\lambda_3^{(2)}$, and (D) mode #4 $\Delta\lambda_4^{(2)}$. The colorbar inset in (A) describes the relative strength $\langle \varphi^{(2)}|V|\varphi^{(2)}\rangle$ of these perturbations (0-100%). The dotted lines indicate the φ= ±450 azimuthal lines, and signify a sensitivity threshold.

3.4 Experimental methods and diffraction angle measurements

The steps involved in the fabrication of the SUSY laser arrays are schematically depicted in Fig. 3.7. The wafer under process is composed of a multiple quantum well gain layer grown on an intrinsic InP substrate and covered by a 500 nm thick undoped InP film (Fig. 3.7A). The gain layer consists of 10 quantum wells of $In_{x=0.737}Ga_{1-x}As_{y=0.569}P_{1-y}$ (20 nm)/$In_{x=0.564}Ga_{1-x}As_{y=0.933}P_{1-y}$ (10 nm). After cleaning, hydrogen silsesquioxane (HSQ) solution was spun over the wafer to obtain a 100 nm thick layer of the negative tone inorganic electron beam resist (Fig. 3.7B). Laser arrays with different widths and gaps in between were patterned after exposing to the electron beam and developing by tetramethylammonium hydroxide (TMAH) solution (Fig. 3.7C). These patterns then transferred to the wafer through dry etching which is performed by a combination of reactive ion etching and inductively coupled plasma (RIE-ICP) processes (H2:CH4:AR, 40:10:20 SCCM, RIE power: 150 W, ICP power: 150 W, Pressure:35 mT). Overall, 500 nm of InP is removed in selected areas, leaving behind the ridge waveguides of the laser cavities (Fig. 2.7D). The wafer is cleaned in oxygen plasma in order to remove the remnant of organic contaminations and polymers created during the dry etching process. Next, the rear facet of the laser cavities was defined. This was accomplished by using a four-step procedure. First, a 500 nm thick SiO2 mask was deposited by means of plasma-enhanced chemical vapor deposition (PECVD). The ridge waveguides were partially covered by a negative tone photoresist (NR7-3000) through spinning and UV-lithography, allowing the uncovered SiO2 layer to be dry etched. The rear facets of the lasers were formed by further RIE-ICP dry etching of the gain layer in places where SiO2 mask was absent (Fig. 3.7E). The exposed HSQ

and the remaining SiO2 was removed by dissolving in the buffer oxide etchant (BOE) solution. Finally, the front facets of the lasers were defined by cleaving the wafer (Fig. 3.7F).

The experimental setup is schematically illustrated in Fig. 3.8. The pump beam (wavelength: 1064 nm, pulse duration: 9 s, repetition rate: 290 kHz) was provided by a fiber laser. The appropriately shaped pump beam illuminates the sample after passing through a 20X objective. The image of a knife edge is used in order to block the pump beam from the superpartner arrays. Without the knife edge, the diameter of the beam on the sample is approximately 120 μm. The same 20X objective lens also serves to image the top of the sample, illuminated by an ASE light passed through a rotating diffuser, onto an infrared CCD camera. This imaging system allows one to precisely adjust the location of the pump beam with respect to the array. The laser output is collected form the cleaved facet at the edge of the sample by means of a 50X objective lens. The collected emission is then directed into a spectrometer as well as a CCD infrared camera.

To measure the diffraction angle associated with the emission of laser array, a rectangular slit is placed between 50X objective lens and the sample (Fig. 3.9). The rectangular slit is raster-scanned by using a stepper motor parallel to the surface of the sample, i.e. in the direction of lasers' slow axis. To construct the transverse profile of the beam, at each step, the output power passing through the slit is measured by a photodiode operating in the lock-in detection scheme. The slit is then shifted by means of a stepper motor to a new position along the optical axis, where the diffraction angle measurement is repeated. Since the exact distance between these two points along the lens' optical axis is

49

known, the divergence angle of the emerging beam can be determined from these two measurements.
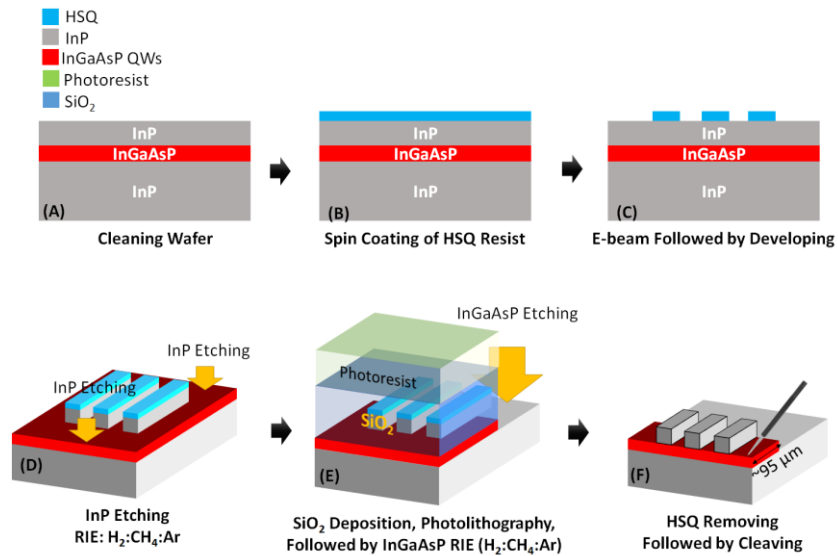
Figure 3.7   Fabrication process. (A) wafer structure, (B) spinning HSQ resist, (C) electron beam lithography and developing, (D) dry etching got transferring the patterns into the wafer, (E) defining the back facet of the lasers through a four step process, (F) cleaving the wafer and removing SiO2 and HSQ by BOE wet-etching.

To obtain the simulated far-field patterns emitted from the laser cavities, first the near-field modes supported by the corresponding ridge waveguides are numerically calculated using finite element method (FEM). Then, the far-field profiles and diffraction angles are calculated using Fourier transform techniques. Figure 3.10A shows the result of the far-field simulation for a SUSY laser (when only the main array is pumped). The simulation result is in good agreement with the experimental measurement (Fig. 3.10B). A similar numerical analysis, performed on the single element laser, also matches well with the experimental observation (Figs. 3.10C, D). It should be noted that, even though both SUSY and single element lasers generate diffraction limited far-field patterns, the beam from the

50

SUSY arrangement has a considerably smaller spot size. This feature in combination with the higher power extracted from such SUSY lasers are direct outcome of radiance (brightness) scaling that is unique to phase-locked arrays.
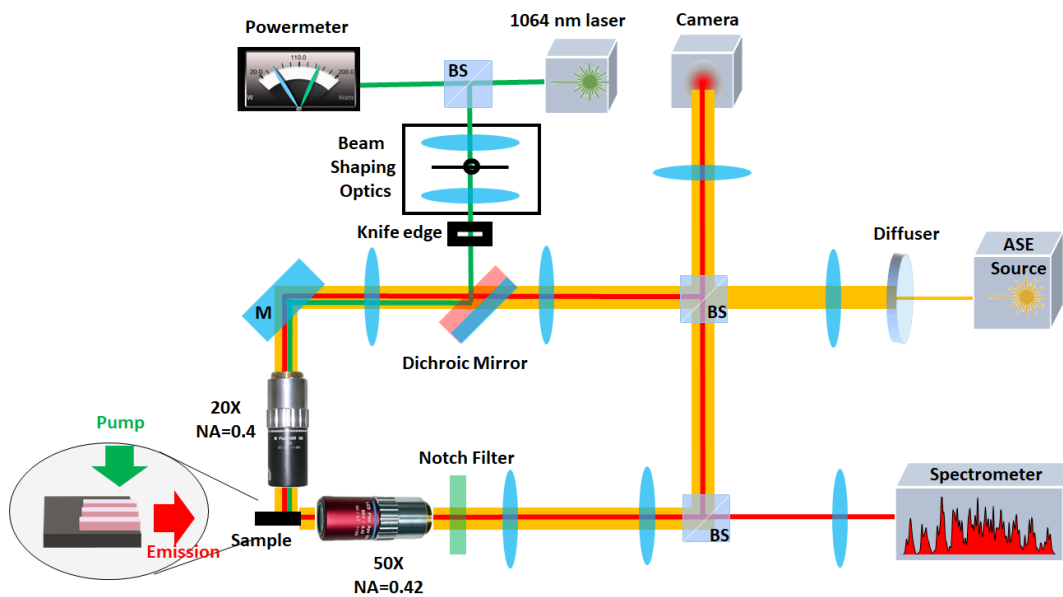
Figure 3.8 Optical measurement setup. A 1064 nm laser is used as the pump source. After shaping into a proper beam size, it illuminates the sample from the top. A knife edge in the path blocks the pump beam form illuminating the superpartner. Additionally, the 20X objective lens along with an ASE source serve to image the sample from a top view onto an IR camera. The emission from the cleaved facets of the lasers are collected via a 50X objective lens and is directed to a spectrometer and the IR camera to capture the far-field patterns of the samples.
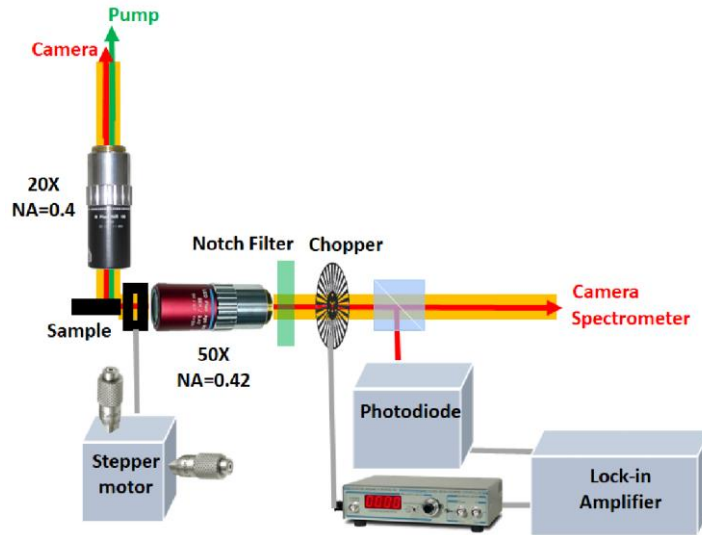
Figure 3.9 Optical setup for diffraction angle measurement. A rectangular slit is raster scanned along the lasers' slow axis by a stepper motor. In each step, a photodiode in a lock-in detection scheme is used to measure the emitted power passing through the slit.
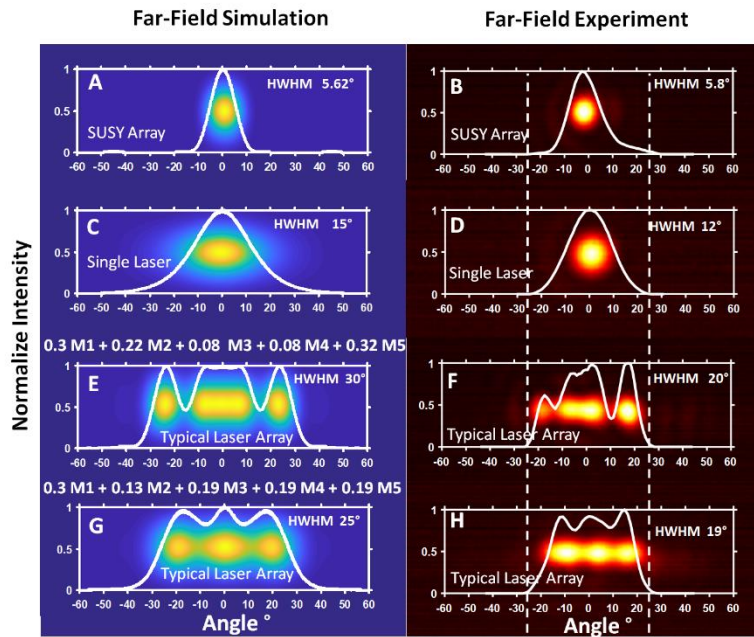
Figure 3.10 Simulated vs. experimental far-field emissions. Numerically obtained far-field diffraction pattern of (A) the SUSY laser array, (C) a single element laser, (E) the standard laser array at 5 times above threshold, and (G) 4 times above threshold. (B), (D), (F), and (H) are the corresponding experimental far-field patterns that match to the simulated profiles. The limitation imposed by the numerical aperture of the 50X objective lens in measuring the diffraction angles is highlighted by dashed lines.

52

Figures 3.10E, G display the calculated far-field emissions of the five-element standard laser array when several supermodes are simultaneously excited. For example, in these figures, the percentage of power distribution among five supermodes involved (from in-phase to out-of-phase modes) are (30, 22, 8, 8, 32), and (30, 13, 19, 19, 19), respectively. These far-field patterns closely resemble the experimental far-field profiles of a standard five-element laser, acquired under two different pumping levels: 5 and 4 times above the threshold (Figs. 3.10F, H). It is worth mentioning that the numerical aperture (NA=0.42) of the 50X objective lens imposes some limitations in capturing the larger diffraction angles in such arrangements.

3.5 Conclusions

To summarize, by harnessing notions from supersymmetry, we present the first realization of an integrated supersymmetric laser array. Our results indicate that the existence of an unbroken SUSY phase in conjunction with a judicial pumping of the laser array, can promote the in-phase supermode thus resulting to a high radiance emission. This new mechanism of phase-locking is resilient to first order deviations in fabrication, and provides a global approach that can be systematically applied to a wide range of coupled active lattices. Our results may have practical implications in designing high brightness single mode laser arrays, while introducing a unique platform to study the interplay between non-Hermiticity and supersymmetry.

3.6 References

1. H. E. Haber and L. K. Gordon, "The search for supersymmetry: probing physics beyond the standard model, " Phys. Rep. **117**, 75-263 (1985).

2. J. H. Schwarz and N. Seiberg, "String theory, supersymmetry, unification, and all that," Rev. Mod. Phys. **71**, 188-202 (1999).

3. M. Dine, *Supersymmetry and string theory: Beyond the standard model* (Cambridge University Press, Cambridge, MA, 2015).

4. G. Junker, *Supersymmetric Methods in Quantum and Statistical Physics* (Springer, 1996).

5. F. Cooper, A. Khare, and U. Sukhatme, "Supersymmetry and quantum mechanics," Phys. Rep. **251**, 267–385 (1995).

6. J. Zinn-Justin, *Quantum Field Theory and Critical Phenomena*, 4th edition, International series of monographs on physics No. 113 (Clarendon Press, Oxford University Press, 2002).

7. Y. Nambu, "Fermion-Boson relations in BCS-type theories," Physica D 15, 147–151 (1985).

8. P. G. Kevrekidis, J. Cuevas–Maraver, A. Saxena, F. Cooper, and A. Khare, "Interplay between parity-time symmetry, supersymmetry, and nonlinearity: An analytically tractable case example," Phys. Rev. E **92**, 042901 (2015).

9. Y. Yu and K. Yang, "Simulating the Wess-Zumino supersymmetry model in optical lattices," Phys. Rev. Lett. **105**, 150605 (2010).

10. D. R. Scifres, R. D. Burnham, and W. Streifer, "Phase-locked semiconductor laser array," Appl. Phys. Lett. **33**, 1015-1017 (1978).

11.   D. Botez, L. Mawst, P. Hayashida, G. Peterson, and T. J. Roth, "High-power, diffraction-limited-beam operation from phase-locked diode-laser arrays of closely spaced ''leaky'' waveguides (antiguides) ," Appl. Phys. Lett. **53**, 464-466 (1988).

12.   J. R. Leger, "Lateral mode control of an AlGaAs laser array in a Talbot cavity, " Appl. Phys. Lett. **55**, 334-336 (1989).

13.   T.-Y. Kao, J. L. Reno, and Q. Hu, "Phase-locked laser arrays through global antenna mutual coupling, " Nat. Photonics **10**, 541–546 (2016).

14.   R. H. Rediker, R. P. Schloss, and L. J. V. Ruyven, "Operation of Individual Diode Lasers as a Coherent Ensemble Controlled by a Spatial Filter within an External Cavity," Appl. Phys. Lett. **46**, 133-135 (1985).

15.   C. J. Corcoran and F. Durville, "Experimental demonstration of a phase-locked laser array using a self-Fourier cavity," Appl. Phys. Lett. **86**, 201118 (2005).

16.   J. R. Andrews, "Traveling-wave amplifier made from a laser diode array," Appl. Phys. Lett. **48**, 1331–1333 (1986).

17.   E. Witten, "Dynamical breaking of supersymmetry, " Nucl. Phys. B **188**, 513–554 (1981).

18.   M.-A. Miri, M. Heinrich, R. El-Ganainy, D. N. Christodoulides, "Supersymmetric optical structures," Phys. Rev. Lett. **110**, 233902 (2013).

19.   M. Heinrich, M.-A. Miri, S. Stützer, R. El-Ganainy, S. Nolte, A. Szameit, and D. N. Christodoulides, "Supersymmetric mode converters, " Nat. Commun. **5**, 3698 (2014).

20.   W. Walasik, B. Midya, L. Feng, N. M. Litchinitser. "Supersymmetry-guided method for mode selection and optimization in coupled systems, " Opt. Lett. **43**, 3758-3761 (2018).

21. M.-A. Miri, M. Heinrich, and D. N. Christodoulides, "SUSY-inspired one-dimensional transformation optics," Optica **1**, 89–95 (2014).

22. S. Longhi, "Supersymmetric Bragg gratings," J. Opt. **17**, 045803 (2015).

23. S. Yu, X. Piao, J. Hong, and N. Park, "Bloch-like waves in random-walk potentials based on supersymmetry," Nat. Commun. **6**, 8269 (2015).

24. A. Macho, R. Llorente, and C. Garcia-Meca, "Supersymmetric transformations in optical fibers," Phys. Rev. Appl. **9**, 014024 (2018).

25. S. Kocinac, V. Milanovic, Z. Ikonic, D. Indjin, J. Radovanovic, and P. Harrison, "SUSY transformation of guided modes in semiconductor waveguides," Phys. Status Solidi **2**, 3552-3555 (2005).

26. S. Longhi, "Supersymmetric transparent optical intersections," Opt. Lett. **40** 463-466 (2015).

27. R. El-Ganainy, L. Ge, M. Khajavikhan, and D. N. Christodoulides, "Supersymmetric laser arrays," Phys. Rev. A **92**, 033818 (2015).

28. J. R. Leger, *Microoptical components applied to incoherent and coherent laser arrays*, in Diode Laser Arrays, D. Botez, D. Scifres, Eds. (Cambridge University Press, 1994), pp-123–179.

29. J. E. Gentle, *Matrix Algebra: Theory, Computations, and Applications in Statistics* (Springer, Berlin, 2007).

30. M. P. Hokmabadi, N. S. Nye, R. El-Ganainy, D. N. Christodoulides, and M. Khajavikhan, "Supersymmetric laser arrays," Science **363**, 623-626 (2019).

CHAPTER 4: RECONFIGURABLE NANOWIRE-BASED RANDOM LASING

4.1 Introduction

Control of the organization of micro- or nano-structures plays an essential role in manipulating light propagation, which is the basis of a wide variety of photonic metamaterials [1-3]. For instance, a periodic arrangement can result in a photonic bandgap within which no propagating mode exists [4], while in structures of increasing disorder light propagation can transition from the diffusion regime to the Anderson localization regime [5]. Fabrication of nanostructure components and accurate control of their relative positions are commonly achieved by top-down approaches. Unfortunately, optical materials created by such top-down methods typically suffer by being expensive to fabricate, and exhibiting non-tunable properties due to their constituent nanostructures having fixed positions. These limitations present a significant barrier for realizing dynamically reconfigurable optical materials. Further, top-down approaches have inherent difficulties to incorporate a diverse variety of heterogeneous component materials, in particular, anisotropic nanomaterials with different sizes, shapes, chemical compositions, and optical functionalities. Nanoparticle anisotropy offers a number of appealing optical properties due to their anisotropic linear and nonlinear susceptibilities, which, for example, can result in differences in absorbance and scattering for light impinging on the particles in longitudinal vs. transverse orientations [6-9]. Individual nanowires have also been used to serve as waveguides for subwavelength photonics or as tiny light sources [10-12], while nanowire collections can function as metamaterials, polarizers or scattering media for random lasing [6,7,9,13,14]. By integrating

reconfigurable particle assemblies [15] into photonic platforms, control over the optical response of the system can be achieved [16-22]. For example, applied electric fields have been used to control orientation of anisotropic nanoparticles or liquid crystals, generating reconfigurable polarizers [17,23]. Less explored, the incorporation of particle anisotropy in a medium with gain should also enable control over the interplay of light amplification, absorption, and scattering, thus providing a means for creating dynamic, active optical materials and devices.

We present a reconfigurable nanoparticle platform [64] that can incorporate anisotropic nanomaterials of diverse sizes and shapes to overcome the fundamental limitations of the top-down approaches. This is accomplished by manipulating collective anisotropy within particle systems through electric field driven assembly. Random lasing arrangements present exemplary models in order to demonstrate how complex optical phenomena can be dynamically controlled via the general approach of high aspect ratio particle assembly; herein we present to the best of our knowledge the first example of a reconfigurable active material system based on scatterer orientation, and propose the underlying mechanism for the observed response. Specifically, we demonstrate control over disorder by electric field directed reconfiguration of TiO2 nanowires suspended in gain medium. Alternating current (AC) electric field driven alignment of these anisotropic scatterers was used to tune random laser emission in real time. We also show that this approach is general by demonstrating it using other anisotropic materials including solid metallic and metal oxide nanowires as well as composite metal/dielectric particles.

58

4.2 Theoretical Analysis

4.2.1 Calculation of the scattering cross section of a single nanowire

The scattering cross section (σ_{sc}) for an individual nanowirecan be defined as:

$$\sigma_{sc} = \frac{1}{P_{inc}} \oiint (\hat{\boldsymbol{n}} \cdot \boldsymbol{P}_{sc}) \, dS \tag{4.1}$$

where $\hat{\boldsymbol{n}}$ represents the vector normal to the surface S (enclosing the scatterer) and pointing outwards from the nanowire, $\boldsymbol{P}_{sc}$ is the scattering intensity (time-averaged Poynting vector), and P_{inc} is the incident intensity. For the evaluation of Eq. (3.1), we have developed appropriate finite element (FEM) models for the computation of both the scattering near- and far-field distributions based on the Straton-Chu formula. The TiO2 nanowires (n_{TiO_2} = 2.6) are immersed in an ethylene glycol (EG) solvent ($n_{EG} = 1.44$), while the wire dimensions are matched to experiment (nanowire length: $L = 1.3 \, \mu m$, diameter: $D = 180 \, nm$). The wavelength of operation is assumed to be $\lambda_o = 585 \, nm$ based on the measured fluorescence peak of rhodamine B (rB) laser dye.

The nanowires are assumed to be excited by a right-handed circularly polarized (RHCP) incident wave. The corresponding field canbe expressed as a linear superposition of the transverse electric (TE) and transverse magnetic (TM) modes, which are out of phase by $\pi/2$. In other words, the total electric field will be given by $\dot{\boldsymbol{E}}_{RHCP} = \dot{\boldsymbol{E}}_{TE} + j\dot{\boldsymbol{E}}_{TM}$, where $\dot{\boldsymbol{E}}_{TE} = (sin\varphi\hat{\boldsymbol{\alpha}}_1 - cos\varphi\hat{\boldsymbol{\alpha}}_2)e^{-jkr}$ and $\acute{\boldsymbol{E}}_{TM} = (cos\theta cos\varphi\hat{\boldsymbol{\alpha}}_1 + cos\theta sin\varphi\hat{\boldsymbol{\alpha}}_2 + sin\theta\hat{\boldsymbol{\alpha}}_3)e^{-jkr}$. Bold letters denote vectors in $\mathbb{R}^3$ space, while dotted bold letters correspond to complex vectors in $\mathbb{C}^3$ space. Vectors $\boldsymbol{k}, \boldsymbol{r}$represent the wavevector and the position vector, respectively, at a point Q with spherical coordinates (r, θ, φ).

To provide a measure of the relative portion of scattering towards the forward/backward direction, the anisotropy factor g is defined as the average of the scattering angle θ:

$$g = \int_{4\pi} p(\theta, \varphi) cos\theta d\Omega = \frac{\int_{4\pi} P(\theta,\varphi) cos\theta d\Omega}{\int_{4\pi} P(\theta,\varphi) d\Omega} = \frac{\int_0^{2\pi} \int_0^{\pi} P(\theta,\varphi) cos\theta sin\theta d\theta d\varphi}{\int_0^{2\pi} \int_0^{\pi} P(\theta,\varphi) sin\theta d\theta d\varphi} \qquad (4.2)$$

where $p(\theta, \varphi) = P(\theta, \varphi)/\int_{4\pi} P(\theta, \varphi) d\Omega$ is the normalized scattering phase function $\left(\int_{4\pi} p(\theta, \varphi) d\Omega = 1\right)$, $P(\theta, \varphi)$ is the intensity in the far-field provided by the radiation diagrams while $d\Omega = sin\theta d\theta d\varphi$ is the differential solid angle, expressed in spherical coordinates. While Eq. (4.2) is typically used in the literature for azimuthally symmetric scattering [24-26], it can still be employed to quantitatively investigate the radiation properties of directive scattering nanoparticles. Analogous studies have been performed in the case of anisotropic biological media, where isotropic diffusion models have been utilized to examine the underlying multiple scattering dynamics [27-29].

4.2.2 Scattering properties of a three-dimensional array of nanowires

In this section, we will perform a probabilistic analysis for a radiating three-dimensional (3D) array of nanowires in a dye laser environment, as shown in Fig. 4.1a. Such investigation is necessary in order to determine, how the randomness in the orientation and location of each nanoantenna will affect the scattering properties of the particle assembly. In order to simplify our study, we will assume identical length L for each nanorod. Each nanowire will be considered as an independent radiating dipole, while the collective effect of all the radiating scatterers will be investigated in the far-field.

In the following analysis, each lattice site will be designated by a triplet $\tilde{m} = (m_1, m_2, m_3)$ with a corresponding position vector $\boldsymbol{r}_o^{\tilde{m}} = m_1 l_1 \hat{\boldsymbol{\alpha}}_1 + m_2 l_2 \hat{\boldsymbol{\alpha}}_2 + m_3 l_3 \hat{\boldsymbol{\alpha}}_3$ (Fig. 4.1). In the latter formulation, parameters l_1, l_2, l_3 represent the periodicity along the x-, y-, and z-axis, while m_1, m_2, and m_3 are integers with $m_1 \in H_1 = [0, M_1 - 1], m_2 \in H_2 = [0, M_2 - 1$ and $m_3 \in H_3 = [0, M_3 - 1]$. Moreover, M_1, M_2, and M_3, represent the number of nanowires in the x-, y-, and z-axis respectively, while $\hat{\boldsymbol{\alpha}}_1, \hat{\boldsymbol{\alpha}}_2, \hat{\boldsymbol{\alpha}}_3$, indicate the unit vectors along the same directions. In all cases, bold letters denote vectors in $\mathbb{R}^3$ space, while dotted bold letters (e.g. complex electric field $\dot{\boldsymbol{E}}$) correspond to complex vectors in $\mathbb{C}^3$ space.

The position of each nanowire is denoted by $\boldsymbol{R}^{\tilde{m}} = \boldsymbol{r}_o^{\tilde{m}} + \Delta \boldsymbol{R}^{\tilde{m}}$, where $\Delta \boldsymbol{R}^{\tilde{m}} = \Delta R_1^{\tilde{m}} \hat{\boldsymbol{\alpha}}_1 + \Delta R_2^{\tilde{m}} \hat{\boldsymbol{\alpha}}_2 + \Delta R_3^{\tilde{m}} \hat{\boldsymbol{\alpha}}_3$ represents the random displacement from the corresponding lattice site $\tilde{m}$. Furthermore, each scatterer is characterized by a random orientation, designated by the azimuth angle $\Phi_c^{\tilde{m}}$ and elevation angle $\Theta_c^{\tilde{m}}$. Moreover, we introduce the following random vectors, which belong to the $\mathbb{R}^{M_1 \cdot M_2 \cdot M_3}$ space: $\Delta \underline{\boldsymbol{R}}_1 = \left(\Delta R_1^{(0,0,0)}, \dots, \Delta R_1^{(M_1-1, M_2-1, M_3-1)} \right)$, $\Delta \underline{\boldsymbol{R}}_2 = \left(\Delta R_2^{(0,0,0)}, \dots, \Delta R_2^{(M_1-1, M_2-1, M_3-1)} \right)$, $\Delta \underline{\boldsymbol{R}}_3 = \left(\Delta R_3^{(0,0,0)}, \dots, \Delta R_3^{(M_1-1, M_2-1, M_3-1)} \right)$, $\underline{\boldsymbol{\Theta}}_c = \left(\Theta_c^{(0,0,0)}, \dots, \Theta_c^{(M_1-1, M_2-1, M_3-1)} \right), \underline{\boldsymbol{\Phi}}_c = \left(\Phi_c^{(0,0,0)}, \dots, \Phi_c^{(M_1-1, M_2-1, M_3-1)} \right)$. The group of random variables $\{\Delta R_1^{\tilde{m}} | \tilde{m} \in H = H_1 \times H_2 \times H_3\}7$ are assumed to be independent and identically distributed (i.i.d). The same also applies independently for $\{\Delta R_2^{\tilde{m}} | \tilde{m} \in H\}$, $\{\Delta R_3^{\tilde{m}} | \tilde{m} \in H\}$, $\{\Theta_c^{\tilde{m}} | \tilde{m} \in H\}$, and $\{\Phi_c^{\tilde{m}} | \tilde{m} \in H\}$. Following the terminology used in probability theory, uppercase letters will denote random variables $(\boldsymbol{R}^{\tilde{m}}, \Delta \boldsymbol{R}^{\tilde{m}}, \Theta_c^{\tilde{m}}, \Phi_c^{\tilde{m}})$, while the corresponding lowercase letters will indicate their particular realizations $(\boldsymbol{r}^{\tilde{m}}, \Delta \boldsymbol{r}^{\tilde{m}}, \theta_c^{\tilde{m}}, \varphi_c^{\tilde{m}})$.

Having provided certain preliminary definitions, we proceed with the electromagnetic field analysis. The spherical wave at a point Q with spherical coordinates (r, θ, φ) radiated from a nanoantenna, located at site $\widetilde{m}$, is described by [30]:

$$\dot{\boldsymbol{E}}^{\widetilde{m}} = \frac{e^{-jk\left(r-R^{\widetilde{m}}\right)}}{r} \dot{\boldsymbol{G}}^{\widetilde{m}}(\dot{\boldsymbol{E}}_{inc}, L, \theta, \varphi, \Theta_c^{\widetilde{m}}, \Phi_c^{\widetilde{m}}), \tag{4.3}$$

where $\boldsymbol{r} = r(cos\varphi sin\theta \widehat{\boldsymbol{a}}_1 + sin\varphi sin\theta \widehat{\boldsymbol{a}}_2 + cos\theta \widehat{\boldsymbol{a}}_3)$ is the position vector at point Q, $\boldsymbol{k} = k \cdot \boldsymbol{r}/r$ is the wavevector with $k = 2\pi/\lambda$ (λ: wavelength in the dye laser medium), $\dot{\boldsymbol{E}}_{inc}$ is the incident field and $\dot{\boldsymbol{G}}^{\widetilde{m}}(\dot{\boldsymbol{E}}_{inc}, L, \theta, \varphi, \Theta_c^{\widetilde{m}}, \Phi_c^{\widetilde{m}})$ is a vector function, which describes the radiation characteristics of the scatterer at site $\widetilde{m}$. In the special case, when the nanoelement $\widetilde{m}$ is aligned to the z-axis ($\theta_c^{\widetilde{m}} = 0^o$) and for sinusoidal current distribution with amplitude I_o along the same direction, the vectorial function $\dot{\boldsymbol{G}}^{\widetilde{m}}$ will be analytically given by:

$$\dot{\boldsymbol{G}}^{\widetilde{m}} = j\eta \frac{I_o}{2\pi} \frac{cos\left(\frac{kL}{2}cos\theta\right) - cos\left(\frac{kL}{2}\right)}{sin\theta} \widehat{\boldsymbol{a}}_\theta \tag{4.4}$$

while for the case of an electrically small dipole, Eq. (4.4) can be simplified as follows:

$$\dot{\boldsymbol{G}}^{\widetilde{m}} = j\eta \frac{kI_oL}{8\pi} sin\theta \widehat{\boldsymbol{a}}_\theta \tag{4.5}$$

where $\widehat{\boldsymbol{a}}_\theta = cos\varphi cos\theta \widehat{\boldsymbol{a}}_1 + sin\varphi cos\theta \widehat{\boldsymbol{a}}_2 - sin\theta \widehat{\boldsymbol{a}}_3$, and η is the characteristic impedance of the dye laser medium.
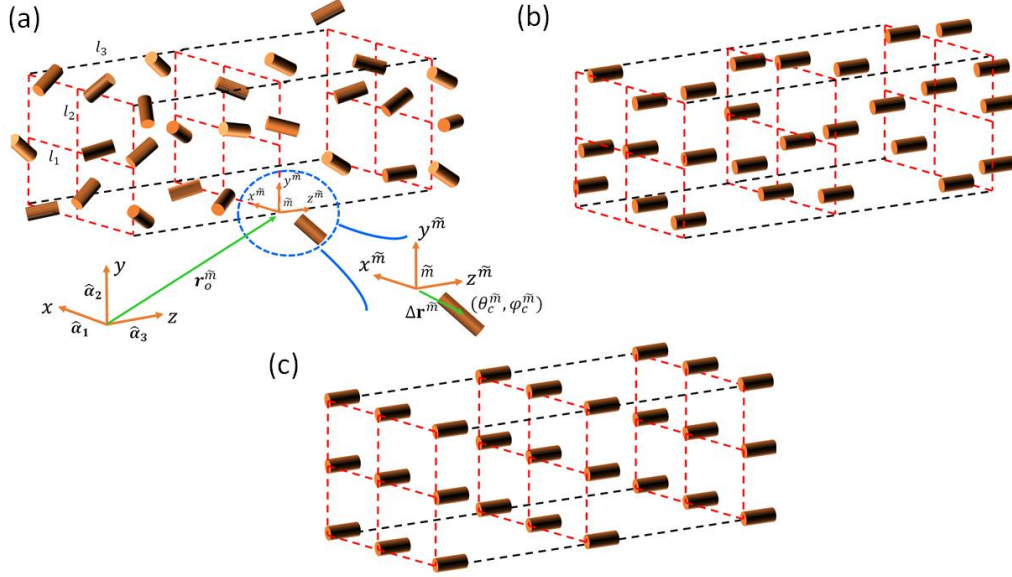
Figure 4.1 (a) Randomly oriented and displaced nanowires in an orthorhombic lattice, with unit cell constants l_1, l_2, l_3. The global and local coordinate systems (at the lattice point $\widetilde{m} = (m_1, m_2, m_3)$) are represented as xyz am $x^{\widetilde{m}} y^{\widetilde{m}} z^{\widetilde{m}}$ correspondingly. The magnified inset depicts the nanowire at site $\widetilde{m}$ (with position vector $r_o^{\widetilde{m}} = m_1 l_1 \hat{a}_1 + m_2 l_2 \hat{a}_2 + m_3 l_3 \hat{a}_3$), along with its relative orientation $(\theta_c^{\widetilde{m}}, \varphi_c^{\widetilde{m}})$ and dislocation $\varDelta r^{\widetilde{m}}$ from the center of the local Cartesian system $x^{\widetilde{m}} y^{\widetilde{m}} z^{\widetilde{m}}$. (b) Parallely oriented nanowires $\{\forall \widetilde{m} \in H : \theta_c^{\widetilde{m}} = 0^o\}$ with random displacements from the respective lattice points. (c) Nanorods located at the lattice sites of the orthorhombic arrangement, with no relative rotation $\{\forall \widetilde{m} \in H : \theta_c^{\widetilde{m}} = 0^o, \varDelta r^{\widetilde{m}} = 0\hat{a}_1 + 0\hat{a}_2 + 0\hat{a}_3\}$.

The total radiated electric and magnetic fields at point Q are given by:

$$\dot{E}_{tot} = \sum_{\widetilde{m}} \dot{E}^{\widetilde{m}} = \sum_{\widetilde{m}} \frac{e^{-jk\left(r - R^{\widetilde{m}}\right)}}{r} \dot{G}^{\widetilde{m}} \tag{4.6}$$

$$\dot{H}_{tot} = \frac{\hat{r} \times \dot{E}_{tot}}{\eta} \tag{4.7}$$

where $\hat{r} = r/r$. We should note that Eq. (4.7) should hold true in the far-field, since in this regime spherical waves behave similarly to plane waves. The time-averaged Poynting vector, calculated in terms of the radiation fields, can be computed as:

$$P_{tot} = \frac{1}{2} Re(\dot{E}_{tot} \times \dot{H}_{tot}^*) = \frac{1}{2\eta} Re\left(\dot{E}_{tot} \times \left(\hat{r} \times \dot{E}_{tot}^*\right)\right)$$

$$= \frac{1}{2\eta} Re\left(\hat{r} \cdot \left(\dot{E}_{tot} \cdot \dot{E}_{tot}^*\right) - \dot{E}_{tot}^* \cdot \left(\hat{r} \cdot \dot{E}_{tot}\right)\right) = \hat{r} \frac{|\dot{E}_{tot}|^2}{2\eta} \tag{4.8}$$

where $\dot{E}_{tot}^*$, indicates the complex conjugate quantity of $\dot{E}_{tot}$. Given Eq. (4.6), we obtain for $|\dot{E}_{tot}|^2$ that:

$$|\dot{E}_{tot}|^2 = \sum_{\widetilde{m}} \sum_{\tilde{n}} \frac{e^{-jk(R^{\tilde{n}}-R^{\widetilde{m}})}}{r^2} \dot{G}^{\widetilde{m}}(\dot{G}^{\tilde{n}})^* \tag{4.9}$$

where $\widetilde{m}$ and $\tilde{n}$ represent lattice sites (m_1, m_2, m_3) and (n_1, n_2, n_3) correspondingly.

After averaging Eq. (4.9) over the random variables $\underline{\Theta}_c$, $\underline{\Phi}_c$, and given that the orientation of each nanowire is independent compared to its neighboring elements, we obtain:

$$< |\dot{E}_{tot}|^2 >_{\underline{\theta}_c,\underline{\phi}_c} = \sum_{\widetilde{m}} \sum_{\tilde{n}} \frac{e^{-jk(R^{\tilde{n}}-R^{\widetilde{m}})}}{r^2} < \dot{G}^{\widetilde{m}}(\dot{G}^{\tilde{n}})^* >_{\Theta_c^{\widetilde{m}},\Phi_c^{\widetilde{m}},\Theta_c^{\tilde{n}},\Phi_c^{\tilde{n}}}$$

$$= \sum_{\widetilde{m}} \sum_{\tilde{n}} \frac{e^{-jk(R^{\tilde{n}}-R^{\widetilde{m}})}}{r^2} < \dot{G}^{\widetilde{m}} >_{\Theta_c^{\widetilde{m}},\Phi_c^{\widetilde{m}}} \left(< \dot{G}^{\tilde{n}} >_{\Theta_c^{\tilde{n}},\Phi_c^{\tilde{n}}}\right)^* \tag{4.10}$$

For two distinct complex vectors $\dot{a}, \dot{b}$, the following is true:

$$(\dot{a})^* \dot{b} + \dot{a}(\dot{b})^* = Re\{(\dot{a})^* \dot{b} + \dot{a}(\dot{b})^*\} \le |(\dot{a})^* \dot{b} + \dot{a}(\dot{b})^*| \le 2|\dot{a}||\dot{b}| \tag{4.11}$$

Given Eq. (4.11), Eq. (4.10) becomes now:

$$< |E_{tot}|^2 >_{\underline{\theta}_c,\underline{\phi}_c} \le \sum_{\widetilde{m}} \sum_{\tilde{n}} \frac{e^{-jk\left(R^{\tilde{n}}-R^{\widetilde{m}}\right)}}{r^2} \left|< \dot{G}^{\widetilde{m}} >_{\Theta_c^{\widetilde{m}},\Phi_c^{\widetilde{m}}}\right| \left|< \dot{G}^{\tilde{n}} >_{\Theta_c^{\tilde{n}},\Phi_c^{\tilde{n}}}\right|$$

$$= \sum_{\widetilde{m}} \sum_{\tilde{n}} \frac{e^{-jk(R^{\tilde{n}}-R^{\widetilde{m}})}}{r^2} \left|< \dot{G}^{\widetilde{m}} >_{\Theta_c^{\widetilde{m}},\Phi_c^{\widetilde{m}}}\right|^2. \tag{4.12}$$

We should note that relation $\left| < \dot{\boldsymbol{G}}^{\widetilde{m}} >_{\Theta_c^{\widetilde{m}}, \Phi_c^{\widetilde{m}}} \right| = \left| < \dot{\boldsymbol{G}}^{\widetilde{n}} >_{\Theta_c^{\widetilde{n}}, \Phi_c^{\widetilde{n}}} \right|$, which was used for the derivation of Eq. (4.12), holds true assuming identical nanowires, as well asidentical distributions of the random variable pairs$\{\Theta_c^{\widetilde{m}}, \Theta_c^{\widetilde{n}}\}$ and $\{\Phi_c^{\widetilde{m}}, \Phi_c^{\widetilde{n}}\}$. According to Jensen's inequality in a probabilistic setting [8], the following inequality holds:

$$\left| < \dot{\boldsymbol{G}}^{\widetilde{m}} >_{\Theta_c^{\widetilde{m}}, \Phi_c^{\widetilde{m}}} \right|^2 \leq < \left| \dot{\boldsymbol{G}}^{\widetilde{m}} \right|^2 >_{\Theta_c^{\widetilde{m}}, \Phi_c^{\widetilde{m}}}. \tag{4.13}$$

In order to enhance the performance of random lasing, emphasis should be given on increasing the peak field scattering strength from the nanowire ensemble. For that purpose, we will emphasize on the supremum of the vector function $\left| < \dot{\boldsymbol{G}}^{\widetilde{m}} >_{\Theta_c^{\widetilde{m}}, \Phi_c^{\widetilde{m}}} \right|$ for $\widetilde{m} \in H$, given that $(\theta, \varphi) \in V = [0 \ \pi] \times [0 \ 2\pi]$. The following inequality holds for supremums [31]

$$\sup_{(\theta,\varphi)\in V} \left\{ < \left| \dot{\boldsymbol{G}}^{\widetilde{m}} \right|^2 >_{\Theta_c^{\widetilde{m}}, \Phi_c^{\widetilde{m}}} \right\} \leq < \sup_{(\theta,\varphi)\in V} \left\{ \left| \dot{\boldsymbol{G}}^{\widetilde{m}} \right|^2 \right\} >_{\Theta_c^{\widetilde{m}}, \Phi_c^{\widetilde{m}}} \leq \sup_{(\theta,\varphi)\in V} \left\{ \left| \dot{\boldsymbol{G}}^{\widetilde{m}} \right|^2_{(\Theta_c^{\widetilde{m}}, \varphi_c^{\widetilde{m}})=(\theta_o,\varphi_o)} \right\}$$

$$\tag{4.14}$$

where (θ_o, φ_o) corresponds to the orientation which leads to maximum scattering, For light incident along the y-axis, the optimum orientation for electrically short wires (Rayleigh scatterers) is $(\theta_o, \varphi_o) = (90^o, 90^o)$, as will be shown numerically in Section 4.5 (Fig. 4.9), while for long wires (Mie scatterers) stronger scattering takes place when the nanorods lie on the xz plane (see Fig. 4.4 in Section 4.4) . After applying Eq. (4.14) to Eq. (4.13), we obtain that

$$\sup_{(\theta,\varphi)\in V} \left\{ < \left| \dot{\boldsymbol{E}}_{tot} \right|^2 >_{\boldsymbol{\Theta}_c, \boldsymbol{\Phi}_c} \right\} \leq \sum_{\widetilde{m}} \sum_{\widetilde{n}} \frac{e^{-jk\left(R^{\widetilde{n}} - R^{\widetilde{m}}\right)}}{r^2} \sup_{(\theta,\varphi)\in V} \left\{ \left| \dot{\boldsymbol{G}}^{\widetilde{m}} \right|^2_{(\theta_c^{\widetilde{m}}, \varphi_c^{\widetilde{m}})=(\theta_o,\varphi_o)} \right\} \tag{4.15}$$

The equality in Eq. (r.15) holds when there is no relative rotation between the individual nanoscatterers, i.e. $\left(\theta_c^{\widetilde{m}}, \varphi_c^{\widetilde{m}} \right) = (\theta_o, \varphi_o)$ for every lattice site $\widetilde{m}$ (see Fig. 4.1(b) for

$\theta_o = 0^o$). Consequently, after substituting $\dot{G} = \dot{G}^{\widetilde{m}}(E^{inc}, L, \theta, \varphi, \theta_c^{\widetilde{m}} = \theta_o, \varphi_c^{\widetilde{m}} = \varphi_o)$ and based on relations $R^{\widetilde{m}} = r_o^{\widetilde{m}} + \Delta R^{\widetilde{m}}$ and $R^{\widetilde{n}} = r_o^{\widetilde{n}} + \Delta R^{\widetilde{n}}$, Eq. (4.9) now becomes

$$\left|\dot{E}_{tot}\right|^2 = \sum_{\widetilde{m}} \sum_{\widetilde{n}} \frac{e^{-jk(R^{\widetilde{n}} - R^{\widetilde{m}})}}{r^2} \left|\dot{G}\right|^2 = \sum_{\widetilde{m}} \frac{1}{r^2} \left|\dot{G}\right|^2 + \sum_{\widetilde{m} \neq \widetilde{n}} \sum_{\widetilde{n}} \frac{e^{-jk(R^{\widetilde{n}} - R^{\widetilde{m}})}}{r^2} \left|\dot{G}\right|^2$$

$$= \frac{\left|\dot{G}\right|^2}{r^2} M + \frac{\left|\dot{G}\right|^2}{r^2} \sum_{\widetilde{m} \neq \widetilde{n}} \sum_{\widetilde{n}} e^{-jk(r_o^{\widetilde{n}} - r_o^{\widetilde{m}})} e^{-jk(\Delta R^{\widetilde{n}} - \Delta R^{\widetilde{m}})}$$

$$= \left|\dot{E}_o\right|^2 M + \left|\dot{E}_o\right|^2 \sum_{\substack{(m_1, m_2, m_3) \\ \neq (n_1, n_2, n_3)}} \sum_{(n_1, n_2, n_3)} \prod_{q=1}^3 e^{-jk \cdot \hat{a}_q (n_q - m_q) l_q} e^{-jk \cdot \hat{a}_q (\Delta R_q^{\widetilde{n}} - \Delta R_q^{\widetilde{m}})} \qquad \textbf{(4.16)}$$

where $M = M_1 M_2 M_3$ is the total number of nanowires, and $\left|\dot{E}^{\widetilde{m}}\right| = \left|\dot{E}_o\right| = \left|\dot{G}\right|/r$.

Having shown that optimum scattering results are obtained when the nanowires are aligned, in the next step of our analysis we will investigate the effect of the random location of each nanoantenna on the far-field radiation. For that purpose, we compute the average of $\left|\dot{E}_{tot}\right|^2$ in Eq. (4.16) with respect to the random displacement variables $\Delta \underline{R}_1, \Delta \underline{R}_2, \Delta \underline{R}_3$. Given that the location of each nanowire is independent from its neighbors, we obtain:

$$< \left|\dot{E}_{tot}\right|^2 >_{\Delta \underline{R}_1, \Delta \underline{R}_2, \Delta \underline{R}_3}$$

$$= \left|\dot{E}_o\right|^2 M$$

$$+ \left|\dot{E}_o\right|^2 \sum_{\substack{(m_1, m_2, m_3) \\ \neq (n_1, n_2, n_3)}} \sum_{(n_1, n_2, n_3)} \prod_{q=1}^3 e^{-jk \cdot \hat{a}_q (n_q - m_q) l_q} < e^{-jk \cdot \hat{a}_q \Delta R_q^{\widetilde{n}}} >_{\Delta R_q^{\widetilde{n}}}$$

$$< e^{jk \cdot \hat{a}_q \Delta R_q^{\widetilde{m}}} >_{\Delta R_q^{\widetilde{m}}}$$

$$= \left|\dot{\boldsymbol{E}}_o\right|^2 M + \left|\dot{\boldsymbol{E}}_o\right|^2 \sum_{\substack{(m_1,m_2,m_3) \\ \neq (n_1,n_2,n_3)}} \sum_{(n_1,n_2,n_3)} \prod_{q=1}^{3} e^{-j\boldsymbol{k}\cdot\hat{\boldsymbol{a}}_q(n_q-m_q)l_q}\, \Phi_{\Delta R_q^{\tilde{n}}}\!\left(-\boldsymbol{k}\cdot\hat{\boldsymbol{a}}_q\right)\Phi_{\Delta R_q^{\tilde{m}}}\!\left(\boldsymbol{k}\cdot\hat{\boldsymbol{a}}_q\right),$$

(4.17)

where $\Phi_{\Delta R_q^{\tilde{n}}}(\omega)$ represents the characteristic function of the random variable $\Delta R_q^{\tilde{n}}$ [32]. Since $\{\Delta R_q^{\tilde{m}}|\tilde{m} \in H\}$ are i.i.d random variables independently of q $(q = 1, 2, 3)$, we can safely perform the substitutions $\Phi_q(\omega) = \Phi_{\Delta R_q^{\tilde{n}}}(\omega) = \Phi_{\Delta R_q^{\tilde{m}}}(\omega)$. Moreover, since the respective probability density functions are even $f_{\Delta R_q^{\tilde{m}}}(\Delta r_q^{\tilde{m}}) = f_{\Delta R_q^{\tilde{m}}}(-\Delta r_q^{\tilde{m}})$ (identical nanowire displacements in the positive or negative directions along the x-, y-, or z- axis are equiprobable), similarly the corresponding Fourier transforms, i.e. characteristic functions, will be even: $\Phi_q(\omega) = \Phi_q(-\omega)$. Therefore, Eq. (4.17) now becomes:

$$< \left|\dot{\boldsymbol{E}}_{tot}\right|^2 >_{\Delta\underline{\boldsymbol{R}}_1,\Delta\underline{\boldsymbol{R}}_2,\Delta\underline{\boldsymbol{R}}_3} = \left|\dot{\boldsymbol{E}}_o\right|^2 M + \left|\dot{\boldsymbol{E}}_o\right|^2 \left\{\prod_{q=1}^{3}\Phi_q^2(\boldsymbol{k}\cdot\hat{\boldsymbol{a}}_q)\right\}\left\{\prod_{q=1}^{3}\left|\frac{sin\left(\frac{\boldsymbol{k}\cdot\hat{\boldsymbol{a}}_q M_q l_q}{2}\right)}{sin\left(\frac{\boldsymbol{k}\cdot\hat{\boldsymbol{a}}_q l_q}{2}\right)}\right|^2 - M\right\}$$

(4.18)

Based on Eq. (4.8), we obtain for the total radiated power

$$< \boldsymbol{P}_{tot} >_{\Delta\underline{\boldsymbol{R}}_1,\Delta\underline{\boldsymbol{R}}_2,\Delta\underline{\boldsymbol{R}}_3} = \boldsymbol{P}_o M + \boldsymbol{P}_o\left\{\prod_{q=1}^{3}\Phi_q^2(\boldsymbol{k}\cdot\hat{\boldsymbol{a}}_q)\right\}\left\{\prod_{q=1}^{3}\left|\frac{sin\left(\frac{\boldsymbol{k}\cdot\hat{\boldsymbol{a}}_q M_q l_q}{2}\right)}{sin\left(\frac{\boldsymbol{k}\cdot\hat{\boldsymbol{a}}_q l_q}{2}\right)}\right|^2 - M\right\}$$ **(4.19)**

where $\boldsymbol{P}_o = \hat{\boldsymbol{r}}\left|\dot{\boldsymbol{E}}_o\right|^2/2\eta$.

From Eq. (4.19), we can deduce that the average total radiated power is the summation of two terms: i) the power radiated from each individual nanoantenna, and ii) the interference arising from the electromagnetic interaction between the distinct

nanoscatterers. When the location of each nanowire is fixed at the points of the 3D orthorhombic lattice (Fig. 4.1c), i.e. $\Delta r_q^{\tilde{m}} = 0$ or equivalently $r^{\tilde{m}} = r_o^{\tilde{m}}$ for every lattice site $\tilde{m}$, then $\Phi_q(k \cdot \hat{a}_q) = 1$. As a result, we obtain from Eq. (4.19) the power radiated from a 3D periodic nanoantenna array. On the other hand, in a probabilistic setting, the presence of the characteristic functions $\Phi_q(k \cdot \hat{a}_q)$, in Eq. (4.19), reduces the effect of the interference term. For instance, if for each displacement direction (x- axis: $q = 1$, y- axis: $q = 2$, z- axis: $q1 = 3$), we assume that $\{\Delta R_q^{\tilde{m}} | \tilde{m} \in H\}$, are i.i.d Gaussian distributed random variables with mean and standard deviation $\mu_q = 0$ and σ_q, correspondingly, then $\Phi_q(k \cdot \hat{a}_q) = \Phi_{\Delta R_q^{\tilde{m}}}(k \cdot \hat{a}_q) = e^{-\sigma_q^2(k \cdot \hat{a}_q)^2/2}$ [32]. In the case when $\sigma_1 = \sigma_2 = \sigma_3 = \sigma$, in Eq. (4.19) it will be true that

$$\prod_{q=1}^3 \Phi_q^2(k \cdot \hat{a}_q) = e^{-\sigma^2 \sum_{q=1}^3 (k \cdot \hat{a}_q)^2} = e^{-\sigma^2 |k|^2} = e^{-(2\pi\sigma/\lambda)^2}.$$
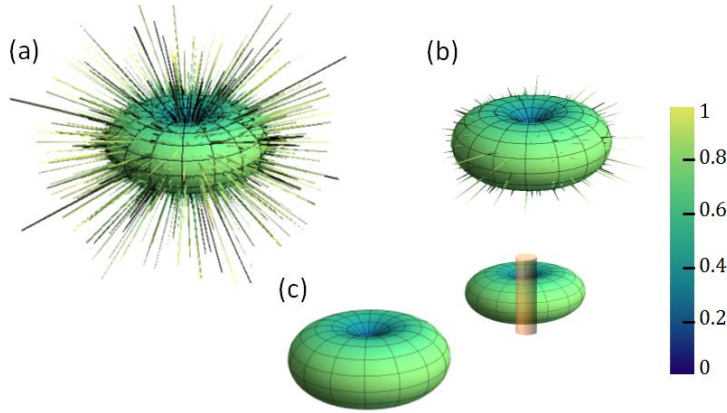
Figure 4.2 Far-field radiation diagrams for different dispersion values σ. The distribution of the normalized electric field $\sqrt{<|\dot{E}_{tot}|^2>_{\Delta R_1, \Delta R_2, \Delta R_3}}$ according to Eq. (S.16) for a 3D array of half-wave dipoles $L = 203 \, nm$ in an ethylene glycol environment at $\lambda_o = 585 \, nm$ is shown for different dispersion values σ in the location of each nanoscatterer: (a) $\sigma = 0.3\lambda = 122 \, nm$, (b) $\sigma = 0.4\lambda = 164 \, nm$, and (c) $\sigma = 0.6\lambda = 244 \, nm$. The inset in (c) depicts the radiation from a single dipole element.

In order to demonstrate the effect of the characteristic function, we analyze the case of radiation from a 3D nanorod array with $M_1 = M_2 = M_3 = 10$ elements ($M = M_1 \cdot M_2 \cdot M_3 = 100$) immersed in ethylene glycol solvent ($n_{EG} = 1.44$). We assume operational wavelength of $\lambda_o = 585\ nm$ and that each nanoscatterer is a half-wave dipole($L = \lambda/2 = \lambda_o/2n_{EG} = 203\ nm$). Moreover, for typical periodicities $l_1 = l_2 = l_3 = 5\ \mu m$, orientation of each element parallel to z-axis, and sinusoidal current distribution, the field from each nanoantenna can be retrieved from Eq. (4.3) and Eq. (4.4). In Fig. 4.2, we show the radiation diagrams for the total normalized electric field corresponding to three distinct cases: i) $\sigma = 0.3\lambda = 122\ nm$, ii) $\sigma = 0.4\lambda = 164\ nm$, and iii) $\sigma = 0.6\lambda = 244\ nm$. It is evident that for moderate values of dispersion ($\sigma \geq 250\ nm$), the far-field distribution becomes identical to that of a single nanoscatterer, since the inherent randomness diminishes the interference effects. Similar conclusions can be drawn for arbitrary scattering functions $\dot{G}$ or induced current distributions. Therefore, we can infer that in highly dispersive dye laser environments, the collective behavior of the nanowire ensemble can be equivalently studied via the radiated field of each individual nanoemitter.

Analogous results can be also found for the more general case, when the nanowires have unequal lengths. Under the assumption that the nanoscatterers are nearly identically oriented - due to the application of an external electric field (for optimum scattering efficiency) - we can classify them based on their respective size and current distribution. Each class will be characterized by an energy flux vector $\boldsymbol{P}_i$ (in the far-field), scattering cross section $\sigma_{sc,i}$, phase function $p_i(\theta, \varphi)$, and anisotropy factor g_i. Moreover, for each set of

nanowires, we assume concentration $\rho_i = N_i/V$, where N_i stands for the number of elements

in each class, while V represents the volume occupied by the assembly. The overall

nanoparticle concentration will then be given by $\rho = M/V = \sum_i N_i/V = \sum_i \rho_i$, where $M = $

$\sum_i N_i$ designates the total number of nanoantennas. The equivalent scattering cross section

of the nanowire ensemble can then be found as:

$$\sigma_{sc,eq} = \frac{1}{P_{inc}} \oiint (\hat{\boldsymbol{n}} \cdot < \boldsymbol{P}_{tot} >_{\Delta\underline{\boldsymbol{R}}_1, \Delta\underline{\boldsymbol{R}}_2, \Delta\underline{\boldsymbol{R}}_3}) dS = \sum_i \frac{N_i}{M} \left\{ \frac{1}{P_{inc}/M} \oiint (\hat{\boldsymbol{n}} \cdot \boldsymbol{P}_i) dS \right\} = \sum_i (\rho_i/\rho)\sigma_{sc,i}$$

(4.20)

where P_{inc} is the incident intensity, S is the surface enclosing the radiating nanoparticle

assembly, $\hat{\boldsymbol{n}}$ is the unit vector normal to the surface S and pointing outwards from the

nanoscatterers, $< \boldsymbol{P}_{tot} >_{\Delta\underline{\boldsymbol{R}}_1, \Delta\underline{\boldsymbol{R}}_2, \Delta\underline{\boldsymbol{R}}_3}$ is the averaged radiated power flux over the random

displacement vectors $\Delta\underline{\boldsymbol{R}}_1, \Delta\underline{\boldsymbol{R}}_2, \Delta\underline{\boldsymbol{R}}_3$, and $\sigma_{sc,i} = \frac{1}{P_{inc}/M} \oiint (\hat{\boldsymbol{n}} \cdot \boldsymbol{P}_i) dS$ is the expression for the

scattering cross section corresponding to class i. In the derivation of Eq. (4.20), we assumed

that $< \boldsymbol{P}_{tot} >_{\Delta\underline{\boldsymbol{R}}_1, \Delta\underline{\boldsymbol{R}}_2, \Delta\underline{\boldsymbol{R}}_3} = \sum_i \boldsymbol{P}_i$. This is a straightforward extension of Eq. (4.19) for the case

of unequal nanowire lengths, if interference effects are neglected. It is also consistent with

the independent scattering approximation [33].

The total scattering coefficient $\mu_{sc,eq}$, based on Eq. (4.20), can now be attained as:

$$\mu_{sc,eq} = \rho\sigma_{sc,eq} = \sum_i \rho_i \, \sigma_{sc,i} = \sum_i \mu_{sc,i} \qquad \textbf{(4.21)}$$

where $\mu_{sc,i} = \rho_i\sigma_{sc,i}$ is the scattering strength corresponding to the nanowires with nearly

identical radiating power flux vector $\boldsymbol{P}_i$.

In a similar manner, the equivalent reduced scattering coefficient $\mu'_{sc,eq}$ will be

provided by [56-58]

$$\mu'_{sc,eq} = \Sigma_i \, \mu'_{sc,i} = \Sigma_i (1 - g_i) \, \mu_{sc,i} = \mu_{sc,eq} - \Sigma_i \, g_i \mu_{sc,i} \qquad \textbf{(4.22)}$$

Based on Eq. (4.21), the probability of scattering at an arbitrary point Q in the far-field with coordinates (θ, φ), can be described by $\mu_{sc,i}/\mu_{sc,eq}$ for a nanoparticle belonging in class i. As a result, the equivalent scattering phase function $p_{eq}(\theta, \varphi)$ of the nanowire assembly will be given by:

$$p_{eq}(\theta, \varphi) = \Sigma_i \big(\mu_{sc,i}/\mu_{sc,eq} \big) p_i(\theta, \varphi) \qquad \textbf{(4.23)}$$

The equivalent anisotropy factor will be provided by:

$$g_{eq} = \int_{4\pi} p(\theta, \varphi) \cos\theta d\Omega = \Sigma_i \big(\mu_{sc,i}/\mu_{sc,eq} \big) \int_{4\pi} p_i(\theta, \varphi) \cos\theta d\Omega = \Sigma_i \big(\mu_{sc,i}/\mu_{sc,eq} \big) g_i \quad \textbf{(4.24)}$$

where $g_{eq,i} = \int_{4\pi} p_i(\theta, \varphi) \cos\theta d\Omega$ is the expression for the anisotropy factor corresponding to each class of nanowires, while $d\Omega$ is the differential solid angle. From Eqs. (4.22) and (4.24), alternatively the overall reduced scattering coefficient can be computed as $\mu'_{sc,eq} = \big(1 - g_{eq}\big)\mu_{sc,eq} = \big(1 - \Sigma_i \big(\mu_{sc,i}/\mu_{sc,eq}\big)g_i\big)\mu_{sc,eq} = \mu_{sc,eq} - \Sigma_i \, g_i\mu_{sc,i}$, which agrees with Eq. (4.22).

In conclusion, we can infer about the properties of random scattering media, by equivalently studying the radiation properties of each individual nanoantenna. Moreover, based on Eqs. (4.20-24), one can now investigate the complex photon scattering dynamics taking place in a probabilistic dye laser medium and evaluate its lasing performance, based on equivalent scalar quantities, like the (reduced) scattering coefficient, scattering phase function, and anisotropy factor.

4.3 Nanowire-based random lasing

Random lasing arises from the confinement of light within disordered gain media leading to mirrorless coherent laser emission [34]. Potential applications of random lasing include speckle free imaging, data encryption, military friend-or-foe identification, and biosensing [35-38]. A common variety of random laser is comprised of nanoparticles suspended in fluorescent dye solution, acting as random scatterers and gain medium respectively [39]. Light is confined via multiple scatterings within the particle matrix and is amplified by the gain medium (Fig. 4.3b). At sufficiently high scattering strengths and above a certain pump pulse threshold energy, random lasing emission occurs atop the fluorescence background. A representative random lasing spectrum for a sample of TiO2 nanowires (Fig. 4.3c) suspended in a rhodamine B solution is shown in Fig. 4.3d. Sharp emission peaks can be seen, corresponding to multiple lasing modes. The uneven spacing between these peaks is a characteristic of random lasers, and can be further represented by the field autocorrelation curve, which is the Fourier transform of the emission spectrum, as a function of the effective cavity lengths (Fig. 4.3e).

4.4 Orientation-dependent scattering

Random laser emission characteristics have been shown to vary according to not only the number density [40,41] but also the shape of scattering features [42-44]. For anisotropic scatterers, the orientation with respect to impinging light can be expected to impact scattering strength. For example, light that is incident parallel to a nanowire's long axis may experience a different scattering cross section compared to light incident perpendicularly to the long axis. Hence, the rotation angle of an anisotropic particle will influence its scattering interactions.
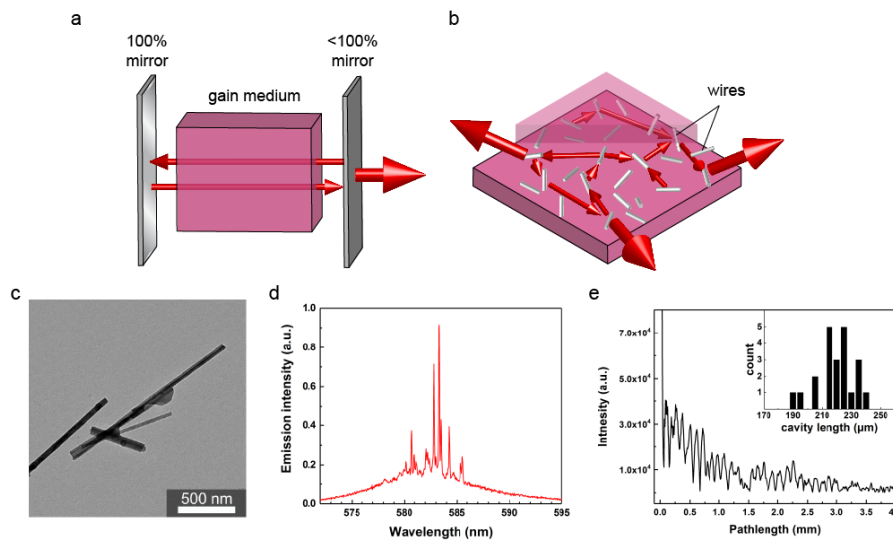
Figure 4.3 Nanowire based random lasing. Illustrations of conventional and nanowire based random laser, TEM of particles used in experiments, and representative experimental random lasing spectrum and analysis. (a) Depiction of lasing buildup in a conventional Fabry Perot laser cavity. (b) Depiction of random lasing in nanowire suspension assembly in dye solution. (c) Representative TEM images of individual TiO2 nanowires. (d) Experimental random lasing spectra produced by a TiO2 nanowire suspension (4.37 × 107 wires/mL) in rB EG dye solution (2 mM). (e) Field autocorrelation curve (Fourier transform of the emission spectrum depicted in (d)) and (inset) effective mode cavity lengths indicating random lasing.

We performed numerical calculations of the scattering cross section of an individual nanowire to validate this hypothesis. The simulation results in Figs. 4.4a,c reveal that for light parallel to the long axis of the nanowires, little angular scattering is observed in both the near- and far-field diagrams. The resonances observed are attributed to the excitation of the fundamental mode along the wire. This arrangement can be considered as a cylindrical guiding structure (core: TiO2, cladding: ethylene glycol), with V-number equal to $=$ $\pi D \sqrt{n_{TiO_2}^2 - n_{EG}^2}/\lambda_o \approx 2.1$. The latter implies single mode operation, while finite element calculations indicate a respective effective index of $n_{eff} = 1.8$. The nanowire acts like a cavity with resonances being $\Delta z = \lambda_o/2n_{eff} = 160$ nm apart, which is verified in Fig. 4.4a. On the other hand, light incident perpendicular to the wire's long axis shows a larger deviation from its original propagation direction both in the near and far field, including a strong backscattering component (Fig. 4.4b,d). In this case, resonances can no longer be sustained, while the far-field diagram (Fig. 4.4d) appears to be azimuthally asymmetric, owing to the large anisotropy between the longitudinal and transverse dimensions of the wire ($L/D = 7.2$). Smaller contrast ratios will result in more symmetric radiation diagrams with reduced scattering and thus inferior lasing performance (see Section 4.2.2). The orientation-dependent scattering is corroborated experimentally in Fig. 4.4e by the observed increase of the backscattered light intensity from a TiO2 wire suspension (illuminated with a xenon arc light source) under random and perpendicular aligned orientations. Due to the enhanced scattering of individual nanowires as shown in simulation, the overall backscattered intensity increased as a result of wire alignment.

Each individual scatterer exhibits a strong angular scattering field component (Fig. 4.4a-d). Such angular scattering can be significantly enhanced in a nanoparticle ensemble, if the nanowires have identical orientation, and can impact the laser emission directionality [45]. A nanowire suspension aligned perpendicularly to the propagation direction will more strongly confine and amplify light, resulting in improved laser quality at reduced pump pulse threshold energy. Furthermore, if average nanowire orientation uniformity can be tailored within the assembly, the net scattering strength of the suspension can be tuned in order to optimize the lasing performance. In Section 4.2.2, by treating the nanowire ensemble as a probalistic setting, we analytically show how the relative orientation (θ_c, φ_c) of the scatterers affects the peak scattering strength in the far-field. The optimum case appears when all the nanowires are parallely oriented $(\theta_c = 0^o)$, resulting in improved lasing performance in active environments. Moreover, the randomness in the location of the individual nanoantennas is shown to mitigate the interference effects among the scatterers. As a result, the overall far-field diagrams can be readily deduced by studying the radiation characteristics from each invidividual nanowire. In the case of nonuniform distribution of wire lengths, the total scattering cross section can be retrieved by averaging over the wire ensemble (see Section 4.2.2).

While anisotopic particles have been previously shown to impact lasing properties in random but fixed configurations, reconfigurable particle orientation has hitherto not been used as a tool to control the lasing emission characteristics. Tuning of random lasers has primarily been approached by techniques such as liquid crystal alignment, which generates local differences in refractive index to introduce scattering [46-49] and spatial light

modulation of pump beams, which used to manipulate the spatial distribution of gain in the lasing medium [50,51]. In contrast, our approach is based on controlling the orientation of nanowires as anisotropic scatterers using an electric field, and thus provides new opportunities to dynamically control a variety of parameters including both the scattering and gain landscapes.
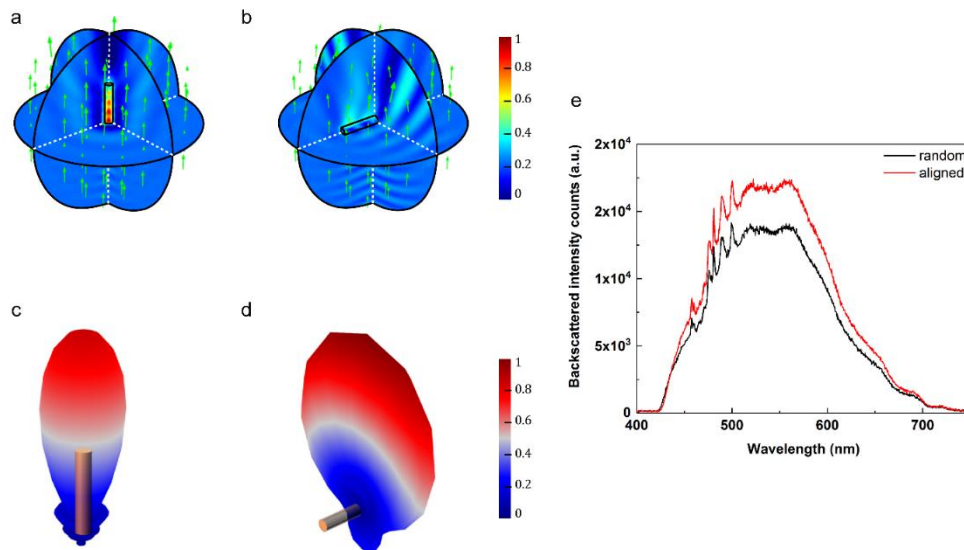
Figure 4.4   Orientation-dependent scattering. Near- and far-field plots representing scattering direction and intensity from a single TiO2 nanowire of length 1.3 μm for incident circularly polarized 585 nm light: (a) near-field pattern with light incidence parallel to wire long axis, (b) near-field pattern with light incidence perpendicular to wire long axis, (c) far-field intensity pattern with light incidence parallel to wire long axis, (d) far-field intensity pattern with light incidence perpendicular to wire long axis. The first row (top) corresponds to near-field cross sections of field E. The second row (bottom) depicts a 3D perspective of the far-field intensity ($|E|2$). (e) Experimental backscattered light intensity from a TiO2 nanowire suspension under random and perpendicular aligned. orientations. Due to the enhanced scattering of individual nanowires, the overall backscattered intensity increased as a result of wire alignment.
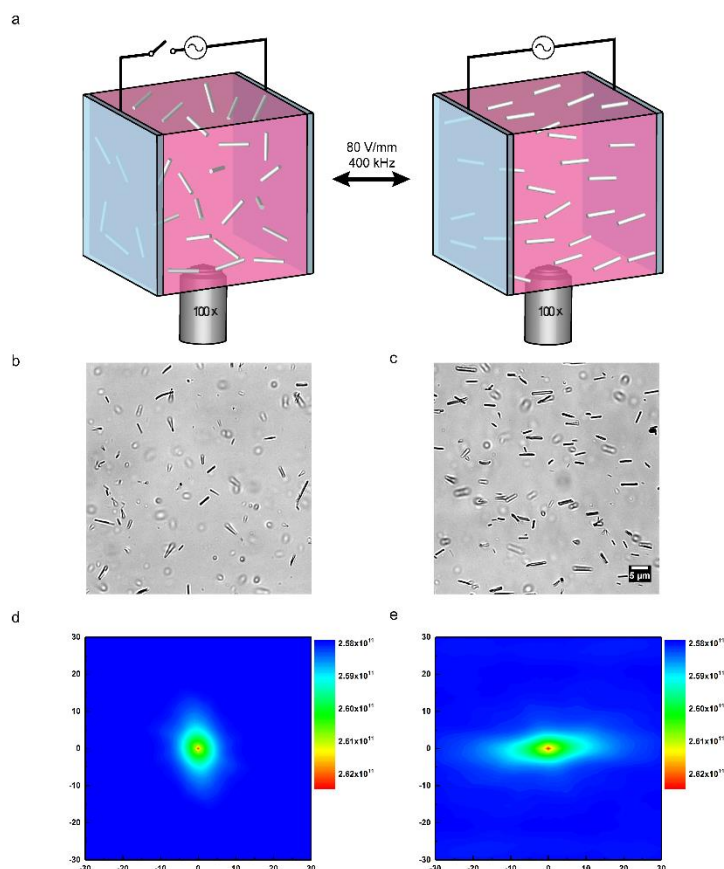
Figure 4.5 Reconfigurable nanowire random laser system. Schematic, optical images, and alignment characteristics of tunable random laser nanowire suspensions. (a) 3D schematic representation of wire assembly cell depicting reversible wire alignment. ITO is separated by a 500 μm thick silicone spacer (not shown). Samples are pumped and emission is epi-collected via a 100× oil immersion objective. When no field is applied across the assembly gap, wires randomly orient via a Brownian motion mechanism (left). Application of an electric field (80 V/mm, 400 kHz) across the sample orients the wires parallel to the horizontal field lines (right). The transition between random and aligned orientation states is reversible. (b, c) Transmission bright field optical microscope images of TiO2 wires suspended in rB EG solution confined in an assembly cell under (b) unassembled and (c) assembled conditions. (d, e) Autocorrelation results indicating the random and aligned wire orientation character depicted in (b) and (c) respectively.

Alignment of nanowires in suspension is accomplished through a technique called electro-orientation, in which an AC electric field is applied across the sample. The field induces the formation of a dipole along the long axis of the wires, which readily rotate in order to align their poles parallel to the field lines [52-55]. A custom assembly cell was designed in order to facilitate this reversible assembly (Figs. 4.5a, 4.6). Conductive indium tin oxide (ITO) cell walls connected to a function generator, generate the AC field across the random laser system (TiO2 wires suspended in 2 mM rB EG). The wires transition from random orientations (Fig. 4.5b,d) to a uniform aligned state (Figure 4.5c,e) in response to the field. Decreasing the applied voltage returns the nanowires to a Brownian motion governed randomized orientation.
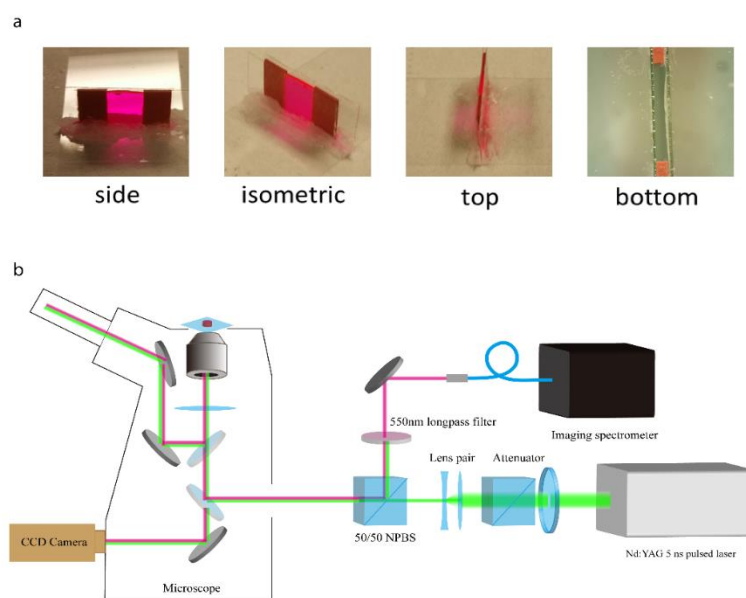
Figure 4.6 Assembly cell & experimental setup . (a) Photographs of a representative assembly cell filled with random laser nanowire suspension. (b) Diagram of the random laser experimental setup including pulsed optical excitation, imaging, and spectroscopy components.

4.5 Reconfigurable random lasing

To experimentally verify the impact of reconfigurable wire alignment on random lasing, we constructed a hybrid experimental setup, which enables simultaneous particle assembly, gain excitation, lasing emission analysis, and nanoparticle imaging (Fig. 4.6). A pulsed Nd:YAG laser (wavelength: 532 nm, repetition rate: 10 Hz, pulse width: 5 ns) is coupled into an inverted Nikon microscope. Samples are excited in a 60 μm diameter spot by a 100× oil immersion objective. Sample emission is then epi-collected and analyzed by an optical spectrometer. For low nanowire concentration (4.3×107 particles/mL) lasing is not observed at any pulse excitation energy due to insufficient scattering (particles in a random orientation state (see Fig. 4.7a). However, by applying the electric field the nanowires become aligned and lasing is observed at up to a 20-fold intensity increase, even at low pumping energies (Fig. 4.7b). Figure 4.7c displays this response directly, presenting emission spectra collected from a single location of the device both before and after assembly. The fluorescence spectrum (black curve) corresponds to the initial unassembled state, while the spectrum in red shows the formation of lasing peaks owing to the wire alignment. This behavior is shown to be reversible, and is used to modulate light emission between fluorescence and lasing configurations (Figure 4.7d). Moreover, by aligning the scatterers such that their long axes are parallel to each other and perpendicular to the sample's excitation/collection angle, we can significantly improve the random lasing performance.

In agreement with simulation, maximizing the particle assembly's anisotropic character can enhance the scattering strength, hence light confinement and lasing

performance. This can be seen by the asymmetry in the radiation patterns of Fig. 4.4, and is attributed to the light scattering characteristics of TiO2 wires. In order to quantify the collective effect of the nanowires from the scattering simulation results of single particles, the anisotropy factor g is used, which provides a measure of the relative portion of scattering towards the forward/backward direction. To interpret the lasing emission characteristics of the TiO2 nanowire ensemble, the reduced scattered coefficient μ'_{sc} [56-58], defined as $\mu'_{sc} = (1 - g)\mu_{sc}$, where μ_{sc} represents the scattering strength ($\mu_{sc} = N_{sc}\sigma_{sc}$, N_{sc}: concentration of scatterers), is used to describe the diffusion of photons undergoing several scattering events.

In order to better determine how nanoparticle anisotropy is impacting the switchable lasing response observed, we numerically calculate the coefficient μ'_{sc} for different wire length distributions of experimental samples (Fig. 4.8). In Figure 4.7e, the graphs of the effective scattering coefficients under random and aligned configurations are depicted. Immediately prominent is that as wire length increases beyond 0.6 μm, μ'_{s} values show dependency on the assembly condition, while little change is observed for wires with smaller aspect ratios. The difference between unassembled and assembled reduced scattering coefficients (visualized by the shaded area between the plots), further confirms that wire alignment is the key factor influencing lasing configurability, showing a net improvement of nearly 20% when wires are aligned vs random for this experimental sample. Even as wire percent composition reduces to below 5 % of the total sample composition, for long wires the contrast in scattering coefficient remains impressively large.
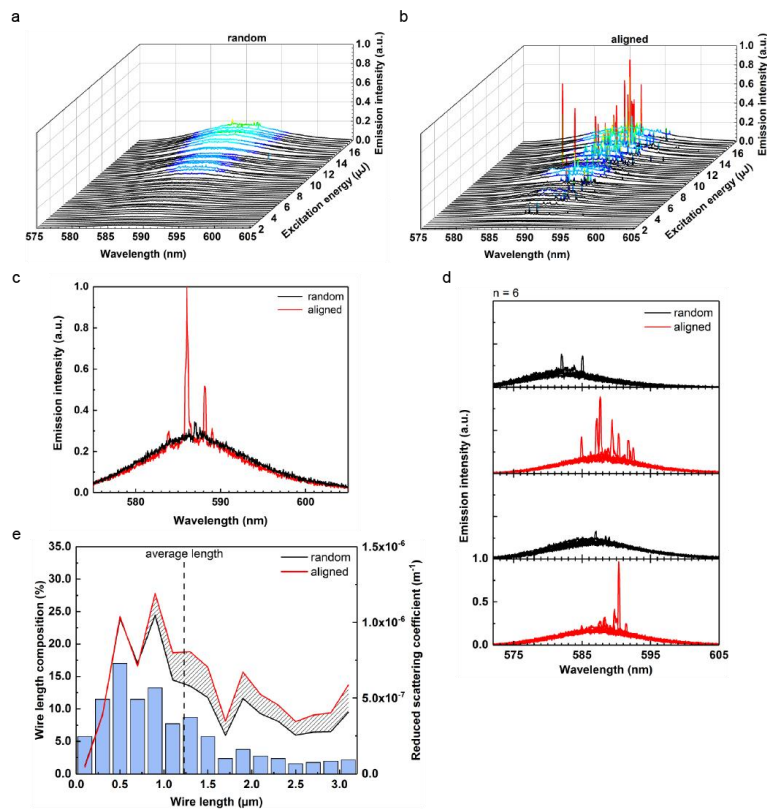
Figure 4.7 Reconfigurable lasing response. Emission spectra and calculated reduced scattering coefficients of randomly oriented nanowire/dye suspensions vs. horizontally assembled nanowire/dye suspensions. (a) Plot of emission spectra of randomly oriented nanowires as excitation energy is increased. (b) Spectra collected from the same sample at the same pumping energies while wires are aligned. (c) Spectra depicting assembly facilitated transition from florescence (black) to lasing (red). Both spectra were collected from the same location of a sample, before and after particle alignment respectively. (d) All spectra shown are collected from a single sample of TiO2 wires (2.16 × 108 wires/mL) suspended in rB EG solution (2 mM). Each plot displays six spectra (initial conditions correspond to top spectra set) obtained from several sample locations. Wire alignment conditions were cycled between unassembled (black) to assembled (red). Ability to turn lasing on/off repeatedly shows robustness of the response. (e) Calculated reduced scattering coefficient plots (black line: randomly oriented wires, red line: wires aligned via applied field) dependent on the heterogeneous wire lengths of sample (a-b) (blue bars). The shaded region between lines represents the increase in reduced scattering coefficient due to assembly.
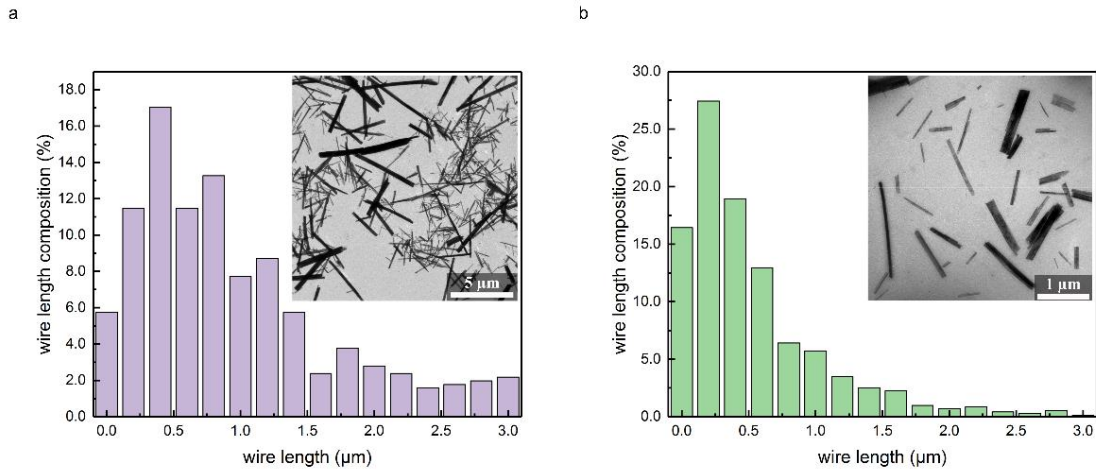
81

Figure 4.8 The commercially available TiO2 wires are rather heterogeneous in length, and tend to form large aggregates in solution if they are not sonicated. Insets are TEM images used in size measurements (a). Brief bath sonication was used to reduce aggregation and narrow the length distribution of reconfigurable random laser samples to 1.23 μm ± 1.1 μm (total wires counted = 532). (b) Probe sonication was used to further reduce average wire length by breaking long particles into smaller segments, ultimately reaching an average size of roughly 0.6 ± 0.55 μm (total wires counted = 722).

The region of Fig. 4.7e corresponding to wires of length shorter than 0.6 μm indicates that alignment of nanowires with short aspect ratios should have minimal impact on scattering coefficient or lasing quality. In order to verify the prominent role of the particle aspect ratio on the random lasing performance, an ensemble of nanowires with shorter lengths was investigated experimentally and numerically. Near- and far- field scattering simulations show that wires of that dimension lead to scattering largely insensitive to the angle of incident radiation (Fig. 4.9). Furthermore, experimentally observed emission spectra for the short wire suspension show no discernible change as a function of wire

alignment (Fig. 4.9). The latter is also verified by the observation that respective reduced scattering coefficient plots are nearly identical for these shorter particles (Fig. 4.9).

Overall, we can deduce that nanoscale material-light interactions can be manipulated through appropriate nanoparticle assembly schemes. By controlling the orientation of the nanorods through an externally applied AC electric field, the scattering cross section of the nanoparticles can be changed to optimize an optical response. In principle, this effect should be generally applicable to any anisotropic particle that can be oriented in the applied field.

4.6 Generality of tunable lasing response with other anisotropic scatterers

We studied several additional anisotropic particles to validate this generality. Figure 4.10 shows the reconfigurable lasing response for solid silver nanowires (3.35 ± 0.89 μm), metal/dielectric segmented particles that consist of 1 μm Au and 1 μm hollow (solvent-filled) segments, encased in a thin silica shell [59,60] and multiphase vanadium oxide nanowires that are heterogeneous in length (4.11 ± 3.71 μm). All of these particles could be oriented in the electric field, and all of them exhibited enhanced lasing when oriented with their long axes perpendicular to the light incidence. The metallic nanowires performed especially well, exhibiting the lowest pump energy threshold (2 μJ as compared with 6 μJ for similarly sized titania and multiphase vanadia wires). The strong improvement of lasing performance supplied by metallic wires is likely due to plasmonic effects, which has potential to be useful for many optical applications [61].

4.7 Experimental Methods

4.7.1 Random laser suspension preparation and device fabrication

Random laser samples were prepared in 1.5 μL micro centrifuge tubes. Rhodamine B powder was weighed via microbalance and dissolved in EG to produce desired concentration dye solutions. TiO2 nanowire powder was weighed in the same fashion and suspended in dye solution via vortexing. Suspensions were then bath sonicated in brief pulses to disperse particle aggregates, or probe sonicated for 60 minutes as a means to reduce average nanowire length [63]. A 600 W Misonix Sonicator S-4000 system with a titanium microtip was used to probe sonicate TiO2 wires in set time intervals to control wire length and reduce aggregation. The microtip pulsed at a 5 s on/3 s off interval; the amplitude was set to 25% power. Samples were placed in an ice bath to avoid heating of the sample. Random laser suspension concentrations were determined post sonication via hemocytometer and adjusted to desired concentration via dilution with additional dye solution. The heterogeneity of particle dimensions was characterized by transmission electron microscopy and recorded as histograms (Fig. 4.8).

Figure 4.6 shows images of sample cells constructed to perform nanowire assembly. ITO coated coverslips were separated by 500 μm thick silicone spacer material. Spacers were cut to size and shape to form wells for sample confinement during experiments such that 20 μL of solution fills the cell. Device walls were secured to the coverslip substrate by using a 90-degree support template and hot glue adhesive.
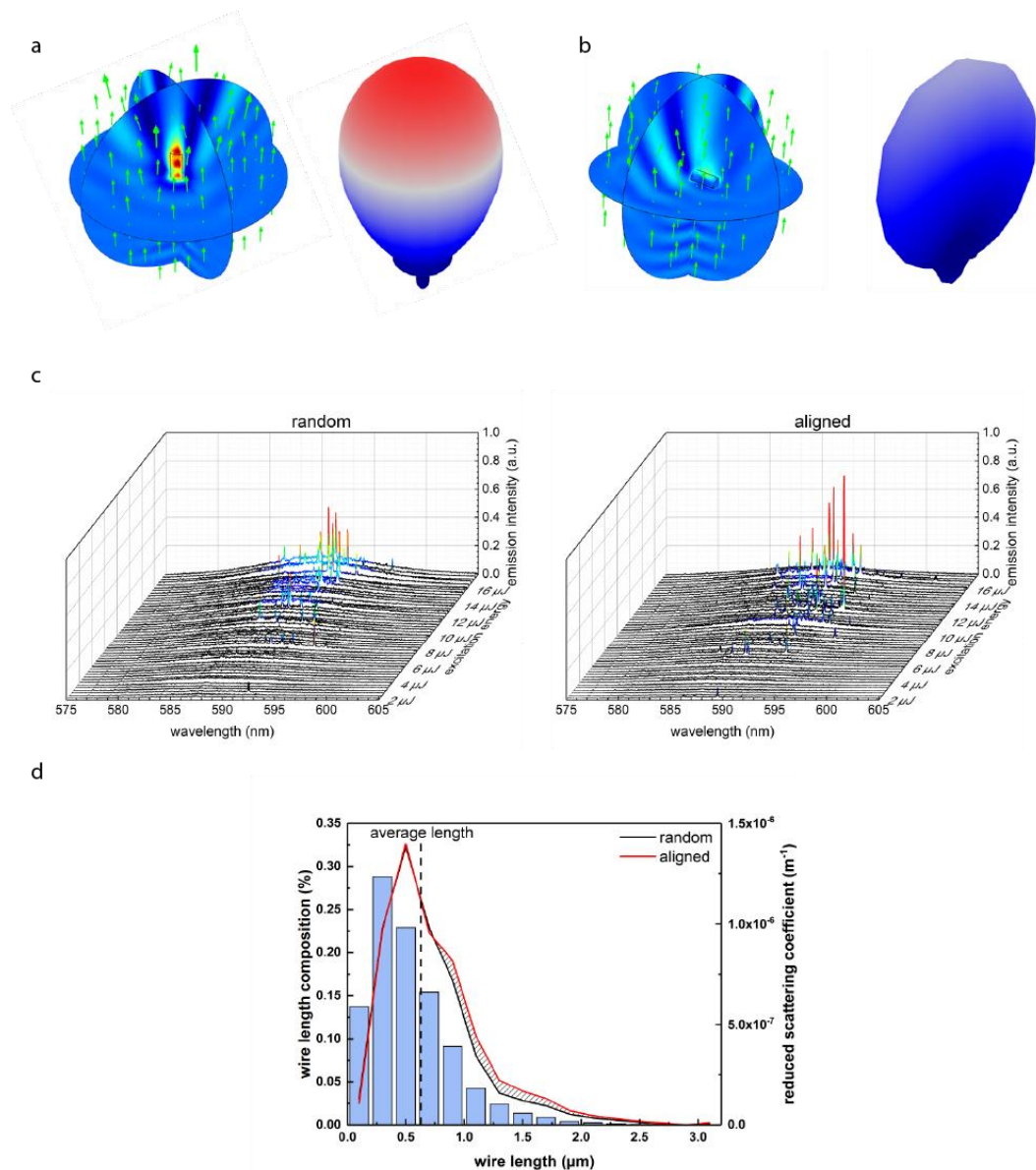
Figure 4.9 Scattering simulations, lasing spectra, and wire length/scattering histogram for shorter nanowires, with mean length of 0.6µm. (a, b) Near- and far-field plots representing scattering from a single TiO2 nanowire of length 1.3µm for circularly polarized incident 585 nm light. (a) light incidence parallel to the long axis of wire and (b) incident light perpendicular to the long axis of wire. (c,d) Random laser emission at very high short wire concentration (109 particles/mL). This high concentration is necessary in order to observe the transitions between the random and aligned assembly conditions. For lower concentrations, similar to the ones of long wire experiments, lasing is never observed. This is in agreement with (d), which shows the corresponding reduced scattering coefficient plot versus the wire length distribution in the sample.
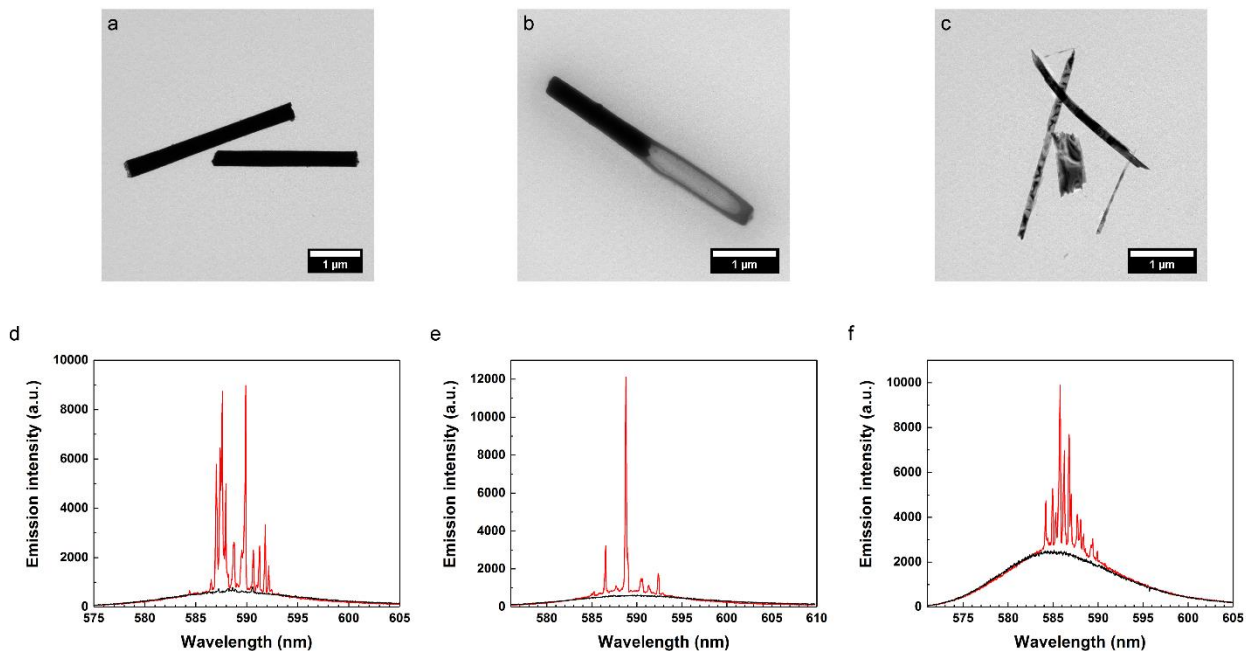
Figure 4.10 Ubiquity across material composition. (top) TEM images of different anisotropic nano-materials and (bottom) respective assembly enabled random lasing response for particles suspended in 2mM rB EG dye solution. (a) Bare silver nanowires synthesized via electrodeposition, (b) glass coated hybrid wire made of gold (dark region) and a solvent filled glass silica shell, (c) multiphase vanadium oxide nanowires, where different phases can be observed in different density regions. (d) Ag nanowire lasing response when (black plot) wires are randomly oriented and (red plot) aligned. (e) Lasing response for hybrid gold/silica wires shown in (b) before (black plot) and after (red plot) horizontal alignment of the wires via assembly. (f) Random lasing tuning behavior of VxOy wire assembly in unaligned (black plot) and aligned (red plot) states.

4.7.2 Hybrid optical/assembly setup

In order to conduct reconfigurable random lasing experiments, a custom optical system was designed and built by integrating a 532 nm 5 ns 10 Hz Nd:YAG laser with a Nikon TE2000-U inverted microscope and a high-resolution optical spectrometer with a liquid nitrogen cooled CCD camera (Princeton Instruments, SpectraPro 2500i). Detailed setup is shown in Fig. 4.6. In general, the pump laser beam was coupled into the microscope's side port enabling excitation of the sample assembly region through a 100× oil immersion objective. Resultant emission signal was epi-collected via the same objective and coupled out of the microscope. A power attenuator (formed by a half waveplate and a polarizing beam splitter (PBS) was used to finely adjust the excitation pulse energy. In detail, the half waveplate rotates the input polarization of the laser beam, which changes the power ratio between the s polarized and the p polarized components. As the polarizing beam splitter only allows the p polarization light to pass through and reflects the s polarization light, we can control the power entering the system. For excitation spot size control, we utilized a convex and concave lens pair with 150 mm and 100 mm focal lengths respectively. In conjunction with a 100× objective, this allowed for a beam size reduction from 9 mm to 60 μm in diameter. Separation of the excitation beam and the emission signal was achieved by using a non-polarizing beam splitter followed by a 550 nm long pass filter. Random laser signal was finally coupled into a large core multimode fiber via a focusing lens and analyzed by the spectrometer.

4.7.3 Data acquisition for random lasing experiments

Random laser samples were placed onto the microscope stage. Gold thread (Ametek Electronic Components) and silver adhesive (Electron Microscopy Sciences) were used to electrically connect ITO coverslips (8–12 Ω, SPI) to leads of a function generator. To perform experiments random laser suspensions were first loaded into custom assembly cells. Optimal AC field parameters for TiO2 wire alignment in rB EG solution were determined to be 80 V/cm and 0.4 MHz via optical microscopy based calibration experiments. Modulation between field "on" and "off" states was then applied in order to assemble and disassemble wire suspensions respectively. Single shot excitation and emission spectrum collection was performed via a custom shutter controlled serially by a computer as needed for each alignment condition throughout experiments. To prevent bleaching of dye in a local area and to ensure spectra collected were representative, the observed location was changed frequently within a sample. Three distinct locations were studied per set of experimental parameters. The respective spectra were collected and subsequently analyzed using WaveMetrics IGOR Pro and OriginPro for normalization of fluorescent backgrounds between comparable experiments. Experiments were generally performed within 30 min. of sample preparation to avoid changes in lasing response due to particle sedimentation.

4.7.4 Fourier transform analysis of lasing emission spectra

The inherent randomness of the emission spectra from a random laser arrangement can be further demonstrated by applying the Fourier Transform (FT) analysis. Specifically, emission spectra are expressed as a function of the wavenumber ($1/\lambda$, λ is wavelength of the

light); the field autocorrelation can then be obtained after performing the Fourier transform as follows.

$$G(x) = \int \left| E\left(\frac{2\pi}{\lambda}\right) \right|^2 e^{-j\frac{2\pi}{\lambda}x} d\left(\frac{2\pi}{\lambda}\right) \tag{4.25}$$

where G(x) is the field autocorrelation function. This means that every peak in G(x) corresponds to a length at which signals exhibit a high degree of coherence (in conventional Fabry Perot lasers G(x) is peaked at integer multiples of the cavity round trip length). Results of random spaced coherence lengths as opposed to evenly spaced ones are shown in Fig. 4.3e and confirm that lasing observed is supported by random scattering particle cavities.

4.7.5 Assembly image autocorrelation calculations

To quantify and visualize the degree of particle alignment, an image autocorrelation technique was applied. Images were run through a threshold and binarization image process to remove background pixels and clearly distinguish nanowires. Note that for autocorrelation results shown in Figs. 4.5d,e, the x- and y-axes represent spatial distance, which allows one to estimate the correlation distance of features in the original image. For the unassembled case, since the particles are oriented randomly, the correlation between particles is weak and isotropic in shape. On the other hand, the assembled particles exhibit uniform orientation along the horizontal direction in the image. Therefore, the autocorrelation function extends on the horizontal axis, indicating net wire alignment in this direction.

4.8 Conclusions

The presented examples demonstrate the generality of the proposed nanoparticle platform to incorporate a diverse variety of anisotropic nano-materials, including segmented metal/dielectric particles and metal oxide phase-transition nanowires that are difficult to fabricate and assemble using conventional top-down approaches. Segmented metal/dielectric particles are highly customizable in design [59], making them candidates for complex reconfigurable ordered or disordered optical systems. Insulator-to-metal phase transitions in certain vanadium oxides (VO_2) have been shown to be a powerful means to tune optical properties [62]. Although this work focuses on the case study of controlling random lasers, we expect that the proposed nanoparticle optical architecture can incorporate heterogeneous materials of a wide range of optical functionalities, including gain, scattering, plasmonic resonance, and nonlinearity, and will thus enable similar reconfigurable optical responses in applications even beyond random lasing, such as the realization of dynamic metamaterials in which the organization of nanostructures plays a key role in determining their optical properties. By introducing an "active" nanoparticle platform enabled with electric field directed assembly, which can exert control over the position and orientation of the constituent heterogeneous nano-materials at the single particle level, we provide a new approach to tune light-matter interactions and hence the collective function of the nanoparticle ensemble.

4.9 References

1. V. M. Shalaev, "Optical negative-index metamaterials," Nat. Photonics **1**, 41-48 (2007).

2. N. Meinzer, W. L. Barnes, and I. R. Hooper, "Plasmonic meta-atoms and metasurfaces. " Nat. Photonics **8**, 889-898 (2014).

3. A. I. Kuznetsov, A. E. Miroshnichenko, M. L. Brongersma, Y. S. Kivshar, and B. Luk'yanchuk, "Optically resonant dielectric nanostructures," Science **354**, aag2472 (2016).

4. E. Yablonovitch, T. J. Gmitter, and K. M . Leung, "Photonic band structure: The face-centered-cubic case employing nonspherical atoms," Phys. Rev. Lett. **67**, 2295-2298 (1991).

5. M. Segev, Y. Silberberg, and D. N. Christodoulides, "Anderson localization of light," Nat. Photonics **7**, 197-204 (2013).

6. R. Yan, D. Gargas, and P. Yang, "Nanowire photonics," Nat. Photonics **3**, 569-576 (2009).

7. J. Yao, Z. Liu, Y. Liu, Y. Wang, C. Sun, G. Bartal, A. M. Stacy, and X. Zhang, "Optical Negative Refraction in Bulk Metamaterials of Nanowires," Science **321**, 930 (2008).

8. X. Guo, Y. Ying, and L. Tong, "Photonic Nanowires From Subwavelength Waveguides to Optical Sensors, " Acc. Chem. Res. **47**, 656-666 (2014).

9. C. R. Simovski, P. A. Belov, A. V. Atrashchenko, and Y. S. Kivshar, "Wire metamaterials: physics and applications," Adv Mater **24**, 4229-4248 (2012).

10. L. Tong, R. G. Gattass, J. B. Ashcom, S. He, J. Lou, M. Shen, I. Maxwell, and E. Mazur, "Subwavelength-diameter silica wires for low-loss optical wave guiding," Nature **426**, 816-819 (2003).

11. M. Law, D. J. Sirbuly, J. C. Johnson, J. Goldberger, R. J. Saykally, and P. Yang, "Nanoribbon Waveguides for Subwavelength Photonics Integration," Science **305**, 1269-1273 (2004).

12. M. H. Huang, S. Mao, H. Feick, H. Yan, Y. Wu, H. Kind, E. Weber, R. Russo, and P. Yang, "Room-Temperature Ultraviolet Nanowire Nanolasers," Science **292**, 1897-1899 (2001).

13. X. Xiong, C.-L. Zou, X.-F. Ren, A.-P. Liu, Y.-X. Ye, F.-W. Sun, and G.-C. Guo, "Silver nanowires for photonics applications," Laser Photonics Rev. **7**, 901-919 (2013).

14. H. Li, X. Wang, J. Xu, Q. Zhang, Y. Bando, D. Goldberg, Y. Ma, and T. Zhai, "One-dimensional CdS nanostructures: a promising candidate for optoelectronics," Adv Mater **25**, 3017-3037 (2013).

15. M. J. Solomon, "Tools and Functions of Reconfigurable Colloidal Assembly," Langmuir **34**, 11205-11219 (2018).

16. M. Wang and Y. Yin, "Magnetically Responsive Nanostructures with Tunable Optical," Properties. J. Am. Chem. Soc. **138**, 6315-6323 (2016).

17. Y. Zhang, Q. Liu, H. Mundoor, Y. Yuan, and I. I. Smalyukh, "Metal Nanoparticle Dispersion, Alignment, and Assembly in Nematic Liquid Crystals for Applications in Switchable Plasmonic Color Filters and E-Polarizers," ACS Nano **9**, 3097-3108 (2015).

18. L. Jiang, H. Mundoor, Q. Liu, and I. I. Smalyukh, "Electric Switching of Fluorescence Decay in Gold–Silica–Dye Nematic Nanocolloids Mediated by Surface Plasmons," ACS Nano **10**, 7064-7072 (2016).

19. M. Zhang, D. J. Magagnosc, I. Liberal, Y. Yu, H. Yun, H. Yang, Y. Wu, J. Guo, W. Chen, Y. J. Shin, A. Stein, J. M. Kikkawa, N. Engheta, D. S. Gianola, C. B. Murray, and C. R. Kagan, "High-strength magnetically switchable plasmonic nanorods assembled from a binary nanocrystal mixture," Nat. Nanotechnol. **12**, 228-232 (2016).

20. A. A. Shah, M. Ganesan, J. Jocz, and M. J. Solomon, "Direct Current Electric Field Assembly of Colloidal Crystals Displaying Reversible Structural Color," ACS Nano **8**, 8095-8103 (2014).

21. Q. Liu, Y. Yuan, and I. I. Smalyukh, "Electrically and Optically Tunable Plasmonic Guest–Host Liquid Crystals with Long-Range Ordered Nanoparticles," Nano Lett. **14**, 4071-4077 (2014).

22. S. Leinberg, V. Kisand, A. Sutka, K. Saal, R. Lohmus, U. Joost, M. Timush, and E. Nommiste, "Switchable optical transmittance of TiO2 submicron-diameter wire suspension-based "smart window" device," Opt. Mater. **46**, 418-422 (2015).

23. S. J. Boehm, L. Kang, D. H. Werner, and C. D. Keating, "Field-Switchable Broadband Polarizer Based on Reconfigurable Nanowire Assemblies," Adv. Funct. Mater. **27**, 1604703 (2017).

24. S. F. Marshall, D. S. Covert, and R. J. Charlson, "Relationship between Asymmetry Parameter and Hemispheric Backscatter Ratio: Implications for Climate Forcing by Aerosols,".Appl. Opt. **34**, 6306-6311 (1995).

25. F. Martelli, S. Del Bianco, A. Ismaelli, and G. Zaccanti, *Light Propagation through Biological Tissue and Other Diffusive Media* (SPIE press Bellingham, Washington, USA, 2010).

26. M. Kerker, *The Scattering of Light and Other Electromagnetic Radiation* (Academic Press, Vol. 16, 1969).

27. K. Alwin, K. F. Florian, D. Rolf, and H. Raimund, "Light Propagation in Dentin: Influence of Microstructure on Anisotropy," Phys. Med. Biol. **48**, N7-N14 (2003).

28. J. Heino, S. Arridge, J. Sikora, and E. Somersalo, "Anisotropic Effects in Highly Scattering," Media. Phys. Rev. E **68**, 031908 (2003).

29. A. Kienle, C. Wetzel, A. Bassi, D. Comelli, P. Taroni, and A. Pifferi, "Determination of the Optical Properties of Anisotropic Biological Media Using an Isotropic Diffusion Model," J. Biomed. Opt. **12**, 014026 (2007).

30. C. A. Balanis, *Antenna Theory: Analysis and Design* (Wiley-Interscience, 2005).

31. Z. Lin and Z. Bai, *Probability Inequalities of Random Variables. In Probability Inequalities* (Springer Berlin Heidelberg, Berlin, Heidelberg, 2011).

32. A. Leon-Garcia, *Probability, Statistics, and Random Processes for Electrical Engineering* (Pearson/Prentice Hall, 3rd ed.,Upper Saddle River, NJ, 2008).

33. R. G. Newton, *Scattering Theory of Waves and Particles* (Springer-Verlag Berlin Heidelberg, 2nd ed., 1982).

34. H. Cao, Y. G. Zhao, S. T. Ho, E. W. Seelig, Q. H. Wang, and R. P. H. Chang, "Random Laser Action in Semiconductor Powder," Phys. Rev. Lett. **82**, 2278-2281 (1999).

35. D. S. Wiersma, "The physics and applications of random lasers," Nat. Phys. **4**, 359-367 (2008).

36. B. Redding, M. A. Choma, and H. Cao, "Speckle-free laser imaging using random laser illumination," Nat. Photonics **6**, 355-359 (2012).

37. F. Luan, B. Gu, A. S. L. Gomes, K.-T. Yong, S. Wen, and P. N. Prasad, "Lasing in nanocomposite random media," Nano Today **10**, 168-192 (2015).

38. E. Ignesti, F. Tommasi, L. Fini, F. Martelli, N. Azzali, and S. Cavalieri, "A new class of optical sensors: a random laser based device," Sci Rep **6**, 35225 (2016).

39. H. Ramachandran, "Mirrorless lasers," Pramana **58**, 313-323 (2002).

40. X. Wu, W. Fang, A. Yamilov, A. A. Chabanov, A. A. Asatryan, L. C. Botten, and H. Cao, "Random lasing in weakly scattering systems," Phys. Rev. A **74**, 053812 (2006).

41. C.-Y. Tsai, Y.-M. Liao, W.-C. Liao, W.-J. Lin, P. Perumal, H.-H. Hu, S.-Y. Lin, C.-H. Chang, S.-Y. Cai,T.-M. Sun, H.-I Lin, G. Haider, and Y.-F. Chen, "Magnetically Controllable Random Lasers,". Adv. Mater. Technol. **2**, 1700170 (2017).

42. V. V. Ursaki, V. V. Zalamai, A. Burlacu, J. Fallert, C. Klingshirn, H. Kalt, G. A. Emelchenko, A. N. Redkin, A. N. Gruzintsev, E. V. Rusu, and I. M. Tiginyanu, "A comparative study of guided modes and random lasing in ZnO nanorod structures," J. Phys. D: Appl. Phys. **42**, 095106 (2009).

43. T. Okamoto and S. Adachi, "Effect of Particle Size and Shape on Nonresonant Random Laser Action of Dye-Doped Polymer Random Media," Opt. Rev. **17**, 300-304 (2010).

44. B. Kumar, S. K. S.Patel, N. S. Gajbhiye, and R. K. Thareja, "Random laser action with nanostructures in a dye solution," J. Laser Appl. 25, 042012 (2013).

45. H. Shin, S. Y. Cho, K. H. Choi, S. Oh, and Y. Kim, "Directional random lasing in dye-TiO2 doped polymer nanowire array embedded in porous alumina membrane," Appl. Phys. Lett. **88**, 263112 (2006).

46. C.-R. Lee, J.-D. Lin, B.-Y. Huang, S.-H. Lin, T.-S. Mo, S.-Y. Huang, C.-T. Kuo, and H.-C. Yeh, "Electrically controllable liquid crystal random lasers below the Fréedericksz transition threshold," Opt. Express 19, 2391-2400 (2011).

47. S. M. Morris, D. J. Gardiner, P. J. W. Hands, M. M. Qasim, T. D. Wilkinson, I. H. White, and H. J. Coles, "Electrically switchable random to photonic band-edge laser emission in chiral nematic liquid crystals,". Appl. Phys. Lett. **100**, 071110 (2012).

48. F. Yao, W. Zhou, H. Bian, Y. Zhang, Y. Pei, X. Sun, and Z. Lv, "Polarization and polarization control of random lasers from dye-doped nematic liquid crystals," Opt. Lett. **38**, 1557-1559 (2013).

49. C.-W. Chen, H.-P. Huang, H.-C. Jau, C.-Y. Wang, C.-W. Wu, and T.-H. Li, "Polarization-asymmetric bidirectional random laser emission from a twisted nematic liquid crystal," J. Appl. Phys. **121**, 033102 (2017).

50. N. Bachelard, S. Gigan, X. Noblin, and P. Sebbah, "Adaptive pumping for spectral control of random lasers," Nat. Phys. **10**, 426-431 (2014).

51. M. Leonetti, C. Conti, and C. Lopez, "The mode-locking transition of random lasers," Nat. Photonics **5**, 615-617 (2011).

52. B. M. I. van der Zande, G. J. M. Koper, and H. N. W. Lekkerkerker, "Alignment of Rod-Shaped Gold Particles by Electric Fields," J. Phys. Chem B **103**, 5754-5760 (1999).

53. J. J. Arcenegui, P. Garcia-Sanchez, H. Morgan, and A. Ramos, "Electro-orientation and electrorotation of metal nanowires," Phys. Rev. E: Stat., Nonlinear, Soft Matter Phys. **88**, 063018 (2013).

54. B. D. Smith, T. S. Mayer, and C. D. Keating, "Deterministic Assembly of Functional Nanostructures Using Nonuniform Electric Fields," Annu. Rev. Phys. Chem. **63**, 241-263 (2012).

55. H. Morgan and N. G. Green, *AC Electrokinetics: Colloids and Nanoparticles* (Research Studies Press, Philadelphia, PA, 2003).

56. V. Ntziachristos, "Going deeper than microscopy: the optical imaging frontier in biology," Nat Methods **7**, 603-614 (2010).

57. S. R. Arridge, "Optical tomography in medical imaging," Inverse Problems **15**, R41-R93 (1999).

58. D. A. Boas, M. A. O'Leary, B. Change, and A. G. Yodh, "Scattering of diffuse photon density waves by spherical inhomogeneities within turbid media: Analytic solution and applications," Proc. Natl. Acad. Sci. U. S. A **91**, 4887-4891 (1994).

59. B. D. Smith, D. J. Kirby, I. O. Rivera, and C. D. Keating, "Self-Assembly of Segmented Anisotropic Particles: Tuning Compositional Anisotropy To Form Vertical or Horizontal Arrays," ACS Nano 7, 825-833 (2013).

60. B. D. Smith, D. J. Kirby, and C. D. Keating, "Vertical Arrays of Anisotropic Particles by Gravity-Driven Self-Assembly," Small **7**, 781-787 (2011).

61. Z. Wang, X. Meng, A. V. Kildishev, A. Boltasseva, and V. M. Shalaev, "Nanolasers Enabled by Metallic Nanoparticles: From Spasers to Random Lasers," Laser Photonics Rev. **11**, 1700212 (2017).

62. Z. Yang, C. Ko, and S. Ramanathan, "Oxide Electronics Utilizing Ultrafast Metal-Insulator Transitions," Annu. Rev. Mater. Res. 41, 337-367 (2011).

63. J. S. Taurozzi, V. A. Hackley, and M. R. Wiesner, "Ultrasonic dispersion of nanoparticles for environmental, health and safety assessment--issues and recommendations," Nanotoxicology 5, 711-729 (2011).

64. P. P. Donahue, C. Zhan, N. Nye, J. Miller, C.-Y. Wang, R. Tang, D. Christodoulides, C. D. Keating, and Z. Liu, "Controlling Disorder by Electric-Field-Directed Reconfiguration of Nanowires To Tune Random Lasing," ACS Nano 12, 7343–7351 (2018).

CHAPTER 5: TILTED-PULSE-FRONT SPACE-TIME WAVE PACKETS

5.1 Introduction

When a pulsed beam passes through a dispersive device, such as a prism or a diffraction grating, each wavelength emerges propagating at a different angle [1]. As a consequence of this angular dispersion, the intensity front of the resulting pulse becomes tilted with respect to the phase front [2]. So-called `tilted-pulse-front' (TPF) pulses have been critical in the development of many applications in nonlinear and quantum optics [3]. In nonlinear optics, TPF pulses have been utilized in single-shot pulse auto-correlators [4], arrangements involving traveling-wave excitation [5], frequency doubling [6-8], and sum-frequency mixing [9], whereupon the use of a TPF pulse increases the phase-matched bandwidth [10-12]. Additionally, TPF pulses were instrumental in the observation of quadratic spatio-temporal solitons [13-15]. In quantum optics, the concept of TPF pulses has enabled increasing the bandwidth of photon pairs produced by the process of spontaneous parametric downconversion, and has helped reduce the correlations between the photons - such that each photon is in a pure quantum state [16-18]. Furthermore, the utilization of TPF pulses in THz applications has led to efficient phase-matching for the generation of intense ultrafast THz pulses by the optical rectification of femtosecond pulses in LiNbO4 [19, 20], thereby enabling femtosecond THz nonlinear spectroscopy [21, 22]. More recently, TPF pulses have been shown to hold promise for synchronizing the interactions between optical radiation and electrons, whether for particle acceleration [23, 24], ultrafast electron microscopy [25], or X-ray generation [26, 27].

The efficacy of TPF pulses in these applications is typically described via a perturbation-based analysis, whereupon the effects of diffraction and space-time coupling are minimized [28-34]. As such, experiments have traditionally made use of pulsed beams having large transverse dimensions and limited propagation distances to avoid spectral walk-off; Fig. 1.1(a). Recently, a theoretical study proposed a closed-form expression for non-paraxial ultrashort pulsed electromagnetic fields that possess the central features of TPF pulses, such as a tilted intensity front [35]. Furthermore, an extension of these proposed pulsed electromagnetic beams were shown to be propagation-invariant [35], therefore hinting tantalizingly at a potential connection between the two apparently disparate topics of TPF pulses [2, 3] and propagation-invariant pulsed beams [36, 37] that have, to date, been synthesized with co-aligned phase and intensity fronts. Underlying all realizations of propagation-invariant pulsed beams [38-46] (or wave packets) is a fundamental principle; namely, that they possess tight spatio-temporal spectral correlations [47-52]. We refer to these pulsed beams as `space-time' (ST) wave packets. We have recently proposed a general spatio-temporal synthesis procedure for synthesizing such ST wave packets [52-55]. To guarantee diffraction-free and dispersion-free propagation, the spatiotemporal spectral loci of ST wave packets must lie at the intersection of the light-cone with tilted spectral hyperplanes [47, 52], which enforces the requisite correlations. The group velocity of a ST wave packet in free space is determined by the tilt angle of the spectral hyperplane, and can be made to take on values above or below the speed of light in vacuum, whether in the forward direction propagating away from the source, or even backwards towards it [56], and such wave packets can propagate in optical materials at the speed of light in vacuum [57].
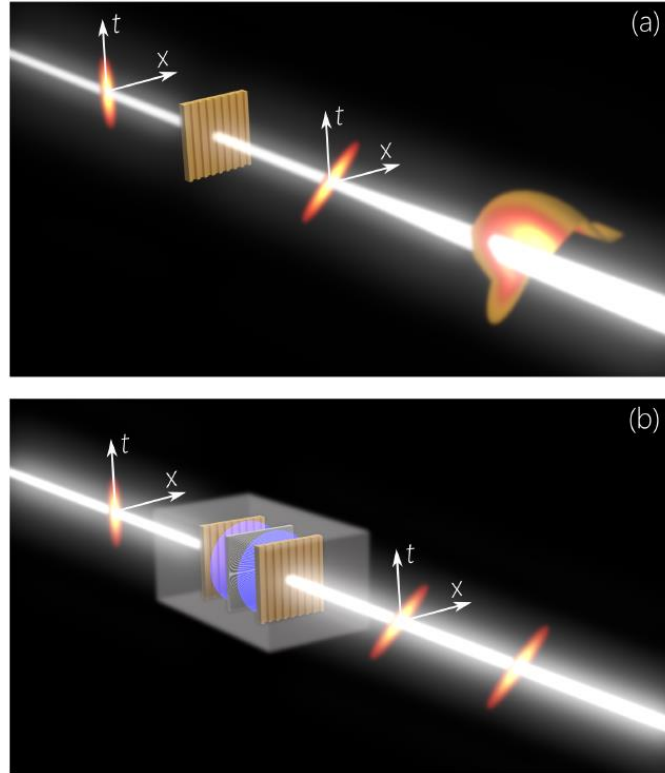
Figure 5.1 Concept of space-time wave packets in the context of TPF. (a) A TPF pulse produced by a dispersive device such as a grating. The field diffracts and disperses with propagation through spectral walk-off and space-time coupling. (b) A TPF-ST wave packet has the same properties of traditional TPF pulses, and is diffraction-free and dispersion-free with propagation even when having a small transverse spatial width. The wave packet is synthesized in transmission mode via a sequence of a grating, a collimating lens, a SLM, a lens, and a grating. In our experiment, we make use of a reflective SLM, and the system thus comprises only three components, a grating, a lens, and the SLM.

Here we demonstrate that sculpting the complex spatio-temporal spectrum of ST wave packets enables the synthesis of a TPF pulse with spatial dimensions hitherto inaccessible to the traditional approaches utilizing a single dispersive optical element [64].

101

By combining ultrafast pulse shaping with spatial beam modulation in the same arrangement, we encode an arbitrary one-to-one relationship between the spatial and temporal frequencies. This spatiotemporal Fourier-optics approach makes use of a dispersive device (a diffraction grating) to separate the temporal spectrum in space, and then reconstitute the pulse after modulating the two-dimensional wave front with a spatial light modulator (SLM) [50, 53, 58]. The wave packet spatio-temporal profile is recorded via an interferometric setup in which spatially resolved fringes resulting from the superposition of the ST wave packet with a short reference pulse reveal the wave packet envelope [56, 57] We thus observe a propagation-invariant ST wave packet featuring a tilted intensity front produced with any desired beam size; Figure 5.1(b). By modulating the spectral phase, we demonstrate control over the shape of the wave packet intensity front; and by modulating the spectral amplitude, we confirm control over the tilt of the intensity front.

Our experiments are based on new propagation-invariant elementary scalar solutions for the homogeneous wave equation. These solutions satisfy a Klein-Gordon equation, which is converted into a modified Helmholtz equation via a complexification of the spatio-temporal degrees of freedom. The solutions are linearly independent, but not mutually orthogonal, and are used as a basis for constructing pulsed beams whose intensity fronts may be tilted or aligned with respect to the phase front. Unlike the more familiar plane-wave basis, the elementary solutions used here have finite spatial and temporal extents, and thus they possess the central features of the more complex propagation-invariant wave packets they are used to construct. Examined in the spatio-temporal spectral domain, these constructed solutions are revealed as having the requisite spatio-temporal

spectral correlations for propagation invariance. However, an added feature is revealed, namely an asymmetric spatial spectrum that results in a TPF structure. We thus firmly establish the connection between the field of TPF pulses and propagation-invariant wave packets. Our results demonstrate that the range of applications of TPF pulses can be extended by harnessing the unique features of ST wave packets, such as self healing [59] and the potential for extended propagation distances [58].

5.2 Theoretical analysis

We start our analysis by assuming a divergence-free field of the form $\vec{E} = \hat{y}E_y(x,z,t)$ satisfying the wave equation $\left(\partial_{xx} + \partial_{zz} - \frac{1}{c^2}\partial_{tt}\right)E_y = 0$, where c is the speed of light in vacuum. We introduce normalized coordinates $X = x/x_n$, $Z = z/x_n$, and $T = ct/x_n$, where x_n is an arbitrary length-scaling parameter, resulting in a wave equation of the form $(\partial_{XX} + \partial_{ZZ} - \partial_{TT})E_y = 0$. The corresponding conjugate variables (k_x, k_z, ω), which are Fourier-transform duals to (x, z, t), will also be normalized according to $k_X = k_x/k_n$, $k_Z = k_z/k_n$, and $\Omega = \omega/\omega_n$, where $k_n = 2\pi/x_n$ and $\omega_n = 2\pi c/x_n$. The normalization parameters will be selected for convenience; for example in Fig. 5.2 we set x_n to be the central wavelength λ_o, while in Fig. 5.3 we choose $x_n = \omega_o$, where ω_o is the half-width at half-maximum of the ST wave packet spatial profile.

We are interested here in propagation-invariant wave packets, specifically those of the form $E_y(X, Z, T) = e^{i\mu Z}G(X, T)$ where $\mu = 2\pi w_n/\lambda_o$ is a normalized propagation constant and λ_o is a central wavelength, in which case G satisfies a Klein-Gordon equation

$(\partial_{XX} - \partial_{TT})G - \mu^2 G = 0$. The dispersion relationship for this field takes the hyperbolic form

$\Omega^2 - k_X^2 = \mu^2$ for a monochromatic plane wave $G \sim e^{ik_X X} e^{-i\Omega T}$. To symmetrize this equation

with respect to space and time, we carry out the substitution $X' = X + iX_o$ and $T' = iT + T_o$,

which results in a complexification of the space and time degrees of freedom; here X_o and T_o

are free parameters that can be used to control the spatio-temporal spectral content (in

particular, its tilt in space-time) and the size of the diffraction-free ST wave packets. As a

result of this transformation, the wave equation regains a Helmholtz-type form $(\partial_{X'X'} +$

$\partial_{T'T'})G - \mu^2 G = 0$, which can be solved in a number of different coordinate systems subject

to the appropriate boundary conditions [60]. We utilize here the cylindrical polar

coordinates system (ρ, φ) related to the Cartesian coordinates through the transformation

$X' + iT' = \rho e^{i\varphi}$ $(X' = \rho cos\varphi, T' = \rho sin\varphi)$, such that

$$\frac{1}{\rho}\frac{\partial}{\partial\rho}\left(\rho\frac{\partial G}{\partial\rho}\right) + \frac{1}{\rho^2}\frac{\partial^2 G}{\partial\varphi^2} - \mu^2 G = 0 \qquad (5.1)$$

Note that ρ and φ mix the spatial and temporal coordinates. By separation of

variables, we obtain solutions of the form

$$G(\rho, \varphi) = K_m(\mu\rho)e^{im\varphi} \qquad (5.2)$$

where m is an integer, $K_m(.)$ is the modified Bessel function of the second kind, while the

modified Bessel function of the first kind $I_m(.)$ is excluded since we demand that G remain

finite when $\rho \to \infty$. Reverting back to our original coordinates, the field takes the form,

$$G(X,T) = K_m\left(\mu\sqrt{(X + iX_o)^2 + (iT + T_o)^2}\right)e^{imtan^{-1}\frac{iT+T_o}{X+iX_o}} \qquad (5.3)$$

The order m of the modified Bessel function determines the spectral extent of the

diffraction-free ST wave packets, as shown in the examples plotted in Fig. 5.2. These

eigenfunctions are linearly independent as can be verified by computing the relevant Wronskian [60], but they are not orthogonal.

To avoid singularities in the phase, we rewrite G as follows,

$$G(X,T) = K_m\left(\mu\sqrt{(X+iX_o)^2+(iT+T_o)^2}\right)\left(\frac{X-T+i(X_o+T_o)}{X+T+i(X_o-T_o)}\right)^{m/2} \tag{5.4}$$

where we have made use of the fact that $e^{im\theta} = \left(\frac{e^{i\theta}}{e^{-i\theta}}\right)^{m/2} = \left\{\frac{(1+i\tan\theta)}{(1+i\tan\theta)}\right\}^{m/2}$. Finally, in evaluating the modified Bessel function of the second kind $K_m(z)$, we have exploited the asymptotic series expansion for large arguments $|z|$ [61],

$$K_m(z) \approx \sqrt{\frac{\pi}{2z}}e^{-z}\sum_{j=0}^{\infty}\frac{a_j(m)}{z^j} \tag{5.5}$$

where the first expansion coefficient is $a_0(m) = 1$, and the subsequent coefficients are given by

$$a_0(m) = 1, \quad a_j(m) = \frac{(4m^2-1)(4m^2-3^2)...(4m^2-(2j-1)^2)}{j!8^j} \quad (j \geq 1) \tag{5.6}$$

For small mode indices m, the main contribution to this infinite sum comes from the first term. Consequently, we expect from Eqs. (5.3-6) that the low-order modes will be nearly degenerate. Note that such ST wave packets formally have in nite energy, which is the case for any truly diffraction-free beam. To attain physically realizable waveforms, we apodize the intensity distributions by multiplying them with an exponential function of the form $e^{-(T/T_c)^2}$, where T_C is a cut-off parameter.

In Fig. 5.2 we plot the spatio-temporal intensity distributions and the corresponding Fourier spectra for different elementary modes of Eq. (5.2). For the fundamental mode $m = 0$, we observe a wavepacket that does not exhibit any tilt in the pulse front [Fig. 5.2(a)]. The

associated spatio-temporal spectrum has two critical features: (1) the spectrum has tight spatio-temporal correlations as a consequence of the propagation invariance of the ST wave packet, and (2) the spectrum of plane waves $e^{i\mu z}e^{\pm ik_x z}$ is excited symmetrically with respect to the origin $k_x = 0$ of the spatial spectrum. The first feature is common to all the elementary wave packets of the form of Eq. (5.2), but the second feature is absent in any wave packet that displays a tilt in the pulse intensity front. For higher-order modes $m > 0$, the pulse front gradually tilts in the spatio-temporal domain, even for small values of m, which is associated with an asymmetric spectral amplitude around $k_x = 0$. Moreover, the sign of m determines the direction of the pulse-front tilt, as seen in the contrast between the positive $m > 0$ values [Fig. 5.2(c) and Fig. 5.2(e)] and the negative values $m < 0$ [Fig. 5.2(g)]. The asymmetry of the spatial spectrum towards positive $k_x > 0$ [2(d, f)] or negative $k_x < 0$ [Fig. 5.2(h)] spatial frequencies follows the direction of the tilt in the pulse front. When $m = -10$, the skewness in the space-time domain becomes significantly large and a single-sided excitation of the spatial spectrum is observed. We note that in addition to the mode order, manipulating the parameter X_o also enables control over the tilt of the pulse front, as clear from comparing Figs. 5.2(c,d) with Figs. 5.2(e,f). In all the cases in Fig. 5.2, the waveforms have not been apodized ($T_c = 1$), and the different parameters are normalized with respective to the central wavelength ($x_n = \lambda_o = 803\ nm$).
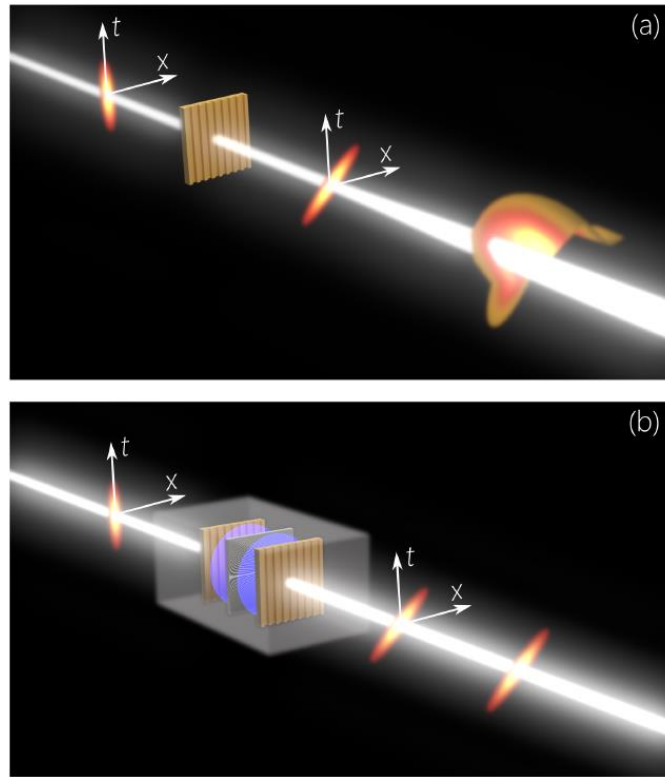
Figure 5.2 Intensity in the spatio-temporal domain (left column) and the corresponding Fourier spectrum (right column) based on simulation results for the following modes: (a, b) K_0 with $X_o = 0$ and $T_o = 4$, where no tilted pulse front is observed and the spectrum is symmetric; (c, d) K_0 with $X_o = 0.3$ and $T_o = 4$, where a tilted pulse front is realized and the spectrum is asymmetric; (e, f) K_5 with $X_o = 0$ and $T_o = 4$, where the tilt of the pulse front has increased compared to (c) and the spectral asymmetry is stronger than in (d); and (g, h) K_{-10} with $X_o = 0$ and $T_o = 4$, where the direction of the tilted pulse front has been reversed with respect to those in (c) and (e), and the direction of the spectral asymmetry has been reversed with respect to (d) and (f). The center wavelength of operation is assumed to be $\lambda_o = 803\ nm$.

In experimentally relevant scenarios, it is expected that generating a specific elementary solution would be prohibitively difficult. Instead, we expect that a superposition of such modes will be excited according to the accessible spatio-temporal spectrum. In Fig. 5.3 we plot simulation results (with $\lambda_o = 803 \, nm$) for three distinct cases that correspond to the experimental configurations to be described in Figs. 5.4-5.6. We introduce two experimentally motivated modifications. First, all the wavepackets are appropriately apodized in time, resulting in a finite spectral uncertainty in the correlation between λ and k_x [50]. Second, the superposition of elementary modes leads to a rapidly varying spectral phase (as described in Eqs. 5.3, 5.4), which we set to a fixed value. In Fig. 5.3(a), we set the spectral phase to 0, resulting in an even-parity symmetric spectrum and thus a spatio-temporal intensity distribution with a central lobe that is symmetric with respect to the space and time coordinates and also lacking in pulse-front tilt. In Fig. 5.3(c) we introduce a π-phase step along the k_x direction, resulting in a spectrum with odd-parity symmetry. This leads to the appearance of a nodal line along the spatial coordinate at x = 0 in the wave packet and two off-center central lobes [Fig. 5.3(d)]. If instead of the symmetric amplitude of the spatio-temporal spectrum we introduce an asymmetry with respect to $k_x = 0$ while holding the phase fixed [Fig. 5.3(e)], then a tilt in the pulse intensity front emerges [Fig. 5.3(f)]. These simulations confirm that the general features observed in the elementary solutions shown in Fig. 5.2 are retained when superposing multiple modes, which helps guide the experimental synthesis process of ST wave packets that have a TPF structure.
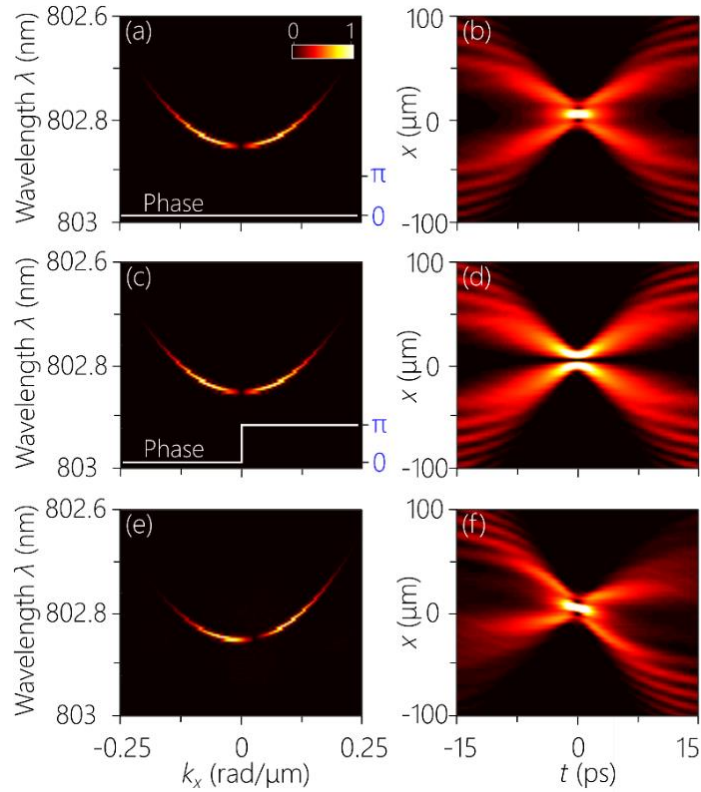
Figure 5.3 Left column shows simulated spatio-temporal spectra $\left|\tilde{E}(k_x,\lambda)\right|^2$ in the (k_x,λ) - domain, and the right column shows the spatio-temporal intensity distribution $|E(x,z,t)|^2$ in the (x,t) - domain at a fixed z. The spatio-temporal spectral phase profiles are flat except in (c), where the phase distribution is shown as an inset. The depicted mode superpositions are (a) $K_0 + K_2$ with the spectral phase set to a constant; (b) $K_0 + K_2$ with a π-phase step introducing odd parity in the spatio-temporal spectrum spectral phase set to a constant; and (c) $K_{41} + K_{43}$ with the spectral phase set to a constant. In all cases we use $X_o = 0$ and $T_o = 100$.

5.3 Experimental methods

Our experimental arrangement is depicted schematically in Fig. 5.4. We start with femtosecond pulses from a Ti:Sapphire laser (Tsunami, Spectra Physics; central wavelength $\approx 800\ nm$) that are spatially expanded. The spectrum is spread in space via a reflective

diffraction grating G (1200 $lines/mm$, dimensions $25 \times 25 \ mm^2$; Newport 10HG1200-800-1), collimated with a cylindrical lens L_{1-y} (focal length 50 mm), and then directed to a spatial light modulator (SLM; Hamamatsu X10468-02) that imprints a two-dimensional phase distribution $\Phi(x, y)$ on the impinging wave front. In this configuration, each wavelength occupies a column on the SLM. The phase distribution Φ is designed such that each column assigns a pair of spatial frequencies $\pm k_x$ to the associated wavelength. Consequently, by changing the arrangement of spatial frequencies along the SLM, any desired correlation relationship between k_x and λ can be realized. Here, we implement the hyperbolic dispersion relationship $(\omega/c)^2 - k_x^2 = \beta^2$, where β is a fixed wave number associated with $k_x = 0$, whereupon ω reaches its smallest value (longest wavelength). This configuration corresponds to an iso-β spectral hyperplane intersecting with the light-cone [50-52].
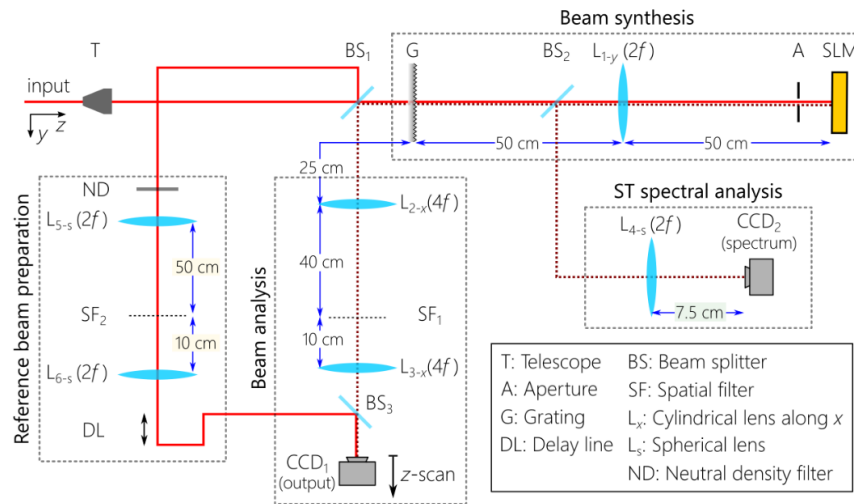
Figure 5.4 Measurement setup for synthesizing and characterizing ST wave packets. The inset provides a key to the elements in the setup.

The wave front incident on the SLM is retro-reflected back through the lens L_{1-y} to the grating G, whereupon the wavelengths are all superimposed and the pulse reconstituted. Because of the correlation between the spatial and temporal frequencies, the ST wave packet is formed at this step. The ST wave packet can then be monitored in space via a CCD camera (CCD1 in Fig. 5.4) that is scanned along the axial direction z, which confirms the diffraction-free propagation of the transverse spatial profile. However, a CCD camera is slow with respect to the pulse width, such that the recorded intensity profile is time-averaged $I(x, z) = \int dt I(x, z, t)$. To reconstruct the spatio-temporal profile $I(x, z, t)$ we make use of the interferometric arrangement shown in Fig. 5.4. We first sample a portion of the initial femtosecond pulses via a beam splitter and direct it to the reference arm in a two-path interferometer. Additional spatial filtering is implemented in the reference arm where a delay line τ can be swept. The ST wave packet (pulse width $\approx 9\,ps$, bandwidth $\approx 0.2\,nm$) is superposed with the much shorter reference pulses (pulse width $\approx 100\,fs$, bandwidth $\approx 10\,nm$) at another beam splitter. When the two pulses overlap in space and time, high visibility spatially resolved fringes are observed at the CCD camera at a fixed plane. It can be shown [56] that the visibility of the fringes as the delay τ is swept is proportional to the spatio-temporal profile $|E(x, z, \tau)|^2$ at fixed z.

Additionally, we measure the spatio-temporal spectrum $\left|\tilde{E}(k_x, \lambda)\right|^2$ of the ST wave packets. By taking a portion of the field retro-reflected from the SLM and performing a spatial Fourier transform to reveal the spatial spectrum while maintaining the temporal spectrum spread, we can record the spatio-temporal spectrum using a CCD camera (CCD2 in Fig. 5.4).
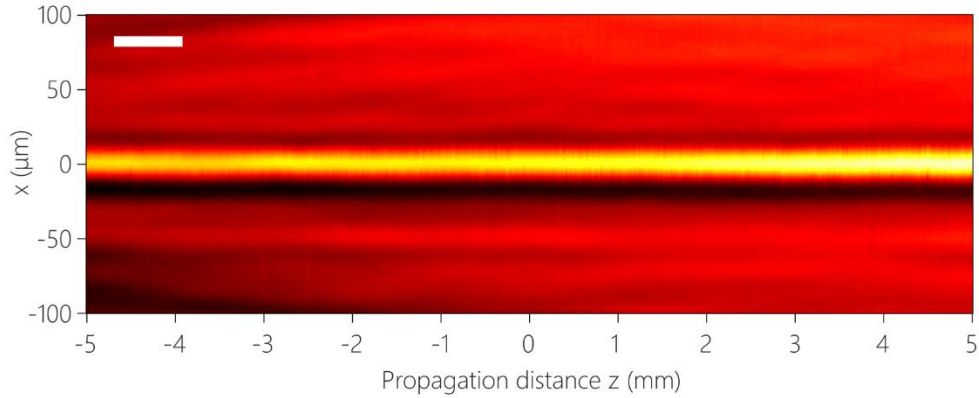
Figure 5.5 Confirmation of the propagation invariance of the ST wave packet. We plot the axial evolution of the time-averaged intensity distribution $I(x, z)$ over a distance of $10\ mm$. The white bar represents the Rayleigh range ($\approx 0.77\ mm$) of a traditional Gaussian beam having the same transverse width as the ST wave packet.

We first confirm the propagation-invariance of the synthesized ST wave packet. We plot in Fig. 5.5 the axial evolution of the time-averaged intensity distribution $I(x, z)$, revealing a transverse width of the spatial profile is $\approx 14\ \mu m$ maintained with minimal change over a distance of $\sim 10\ mm$. This is to be compared to the traditional Rayleigh range of $\sim 0.77\ mm$ for a Gaussian beam of the same transverse width and central wavelength.

We plot in Fig. 5.6 the measured spatio-temporal spectrum $\left|\tilde{E}(k_x, \lambda)\right|^2$ and the results of interferometrically reconstructing the intensity profiles $I(x, z, \tau)$ of three ST wave packets. First, we perform the measurements on a ST wave packet with a symmetric real spectrum [Fig. 5.6(a)]. The intensity profile is shown in Fig. 5.6(b) and confirms a spatially and temporally symmetric distribution. Next, we introduce a π-phase step between the two halves of the spatial spectrum along k_x while maintaining the same magnitudes as in the first

112

ST wave packet [Fig. 5.6(c)]. This π-phase-step is introduced by the SLM by adding a relative phase π to all the negative spatial frequencies. Consequently, a null is produced along the x-direction in the ST wave packet, while remaining symmetric along the temporal axis.

Finally, we introduce asymmetry in the spatio-temporal spectrum by blocking all the negative spatial frequencies [Fig. 5.6(e)]. This does not change the temporal spectrum along λ because there is a one-to-one relationship between λ and $|k_x|$. The reconstructed spatiotemporal intensity profile [Fig. 5.6(f)] shows clearly a tilted wave front of the ST wave packet.

The propagation invariance of these ST wave packets is ultimately limited by the spectral uncertainty in the spatio-temporal spectrum. This spectral uncertainty is the unavoidable 'fuzziness' in the association between the spatial and temporal frequencies (or wavelengths) that is inherent in any finite system. In our setup, the main limiting factor is the spectral resolution of the grating G, which results from its aperture size. We estimate the spectral uncertainty in our case to be $\delta\lambda \sim 25\ pm$ (see the measured spatio-temporal spectra in Fig. 5.6). We have recently shown theoretically and experimentally [62, 63] that the Rayleigh range of the ST wave packet is inversely proportional to $\delta\lambda$, and that the Rayleigh range is enhanced over its Gaussian beam counterpart (of the same transverse width and central wavelength) by a factor equal to the ratio between the full bandwidth and $\delta\lambda$. Indeed, by careful design of the spatio-temporal correlations introduced into the ST wave packet spectrum, the propagation distance can be extended to many meters [58]. The spectral uncertainty does not affect the central result reported here: the tilted-pulse-front structure

113

of the synthesized wave packets relies only on the asymmetry in the spatio-temporal structure.
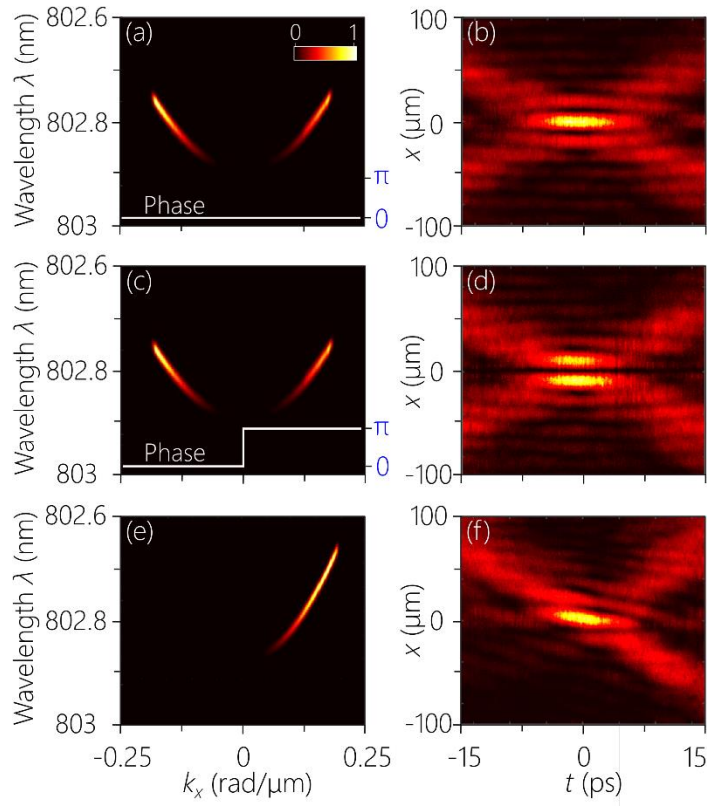
Figure 5.6 Measurement results. The left column shows spatio-temporal spectral intensities, and the right column shows the corresponding intensity profiles in space-time. (a) A symmetric spectrum and at spectral phase, leading to (b) a symmetric ST wave packet. (c) A symmetric spectrum and a spectral phase with a π-step along k_x, leading to (d) a symmetric ST wave packet with a central null. (e) An asymmetric spectrum and at spectral phase, leading to (f) a ST wave packet with a tilted pulse front structure.

5.4 Conclusions

We have demonstrated here that a ST wave packet with amplitude asymmetry introduced into its spatial spectrum has a tilted intensity front with respect to its phase front and the direction of propagation. The possibility of producing TPF ST wave packets may have profound ramifications for applications in nonlinear and quantum optics and light-matter interactions. First, unlike traditional TPF pulses, the ST wave packets presented here have no restrictions on the beam size or pulse width. Furthermore, in principle the group velocity can also be varied arbitrarily and is independent of the spatio-temporal extent of the wave packet [56]. Such characteristics can be maintained over large distances58 even extending to tens of meters. Moreover, ST wave packets may be produced in the high-pulse-energy regime by exploiting transparent refractive phase plates [55], which paves the way to new applications of TPF ST wave packets in light-matter interactions. We finally note that the fields synthesized here have the form of (2 + 1)D wave packets (with one transverse dimension uniform), and future work will focus on extending this framework to (3+1)D wave packets localized in all dimensions, as those introduced in Ref.35 where particular ST wave packets having a TPF structure were introduced for the first time. The functional basis we have provided here can be used to construct further particular solutions along those lines.

In conclusion, we have synthesized and characterized ST wave packets that simultaneously have a tilted-pulse-front structure. These wave packets are based on new propagation invariant elementary solutions of the wave equation identified through a complexification of the spatial and temporal degrees of freedom. Employing these results, we experimentally synthesize ST wave packets that have a pulse intensity front that is tilted

with respect to the propagation axis. By establishing the connection between ST propagation-invariant pulses and TPF pulses, a path is opened to exploiting the unique attributes of ST wave packets in nonlinear and quantum optics, and in novel configurations for the interaction of optical pulses with electrons.

5.5 References

1. B. E. A. Saleh and M. C. Teich, Principles of Photonics (Wiley, 2007).

2. J. P. Torres, M. Hendrych, and A. Valencia, "Angular dispersion: an enabling tool in nonlinear and quantum optics," Adv. Opt. Photon. 2, 319-369. (2010).

3. J. A. Fülöp and J. Hebling, Applications of tilted-pulse-front excitation (Recent Optical and Photonic Technologies, K. Y. Kim Ed., InTech, 2010).

4. R. Wyatt and E. E. Marinero, "Versatile single-shot background-free pulse duration measurement technique, for pulses of subnanosecond to picosecond duration," Appl. Phys. 25, 297-301 (1981).

5. J. Hebling, J. Kuhl, and J. Klebniczki, "Femtosecond optical gating with a traveling-wave amplifier," J. Opt. Soc. Am. B 8, 1089-1092 (1991).

6. V. D. Volosov, S. G. Karpenko, N. E. Kornienko, and V. L. Strizhevskii, "Method for compensating the phase-matching dispersion in nonlinear optics," Sov. J. Quantum Electron., 4, 1090-1098 (1975).

7. O. E. Martinez, "Achromatic phase matching for second harmonic generation of femtosecond pulses," IEEE J. Quantum Electron. 25, 2464-2468 (1989).

8. G. Szabó and Z. Bor, "Broadband frequency doubler for femtosecond pulses," Appl. Phys. B: Photophys. Laser Chem. 50, 51– 54 (1990).

9.   T. Hofmann, K. Mossavi, F. K. Tittel, and Szabó, G, "Spectrally compensated sum-frequency mixing scheme for generation of broadband radiation at 193 nm," Opt. Lett. 17, 1691– 1693 (1992).

10.   A. Dubietis, G. Valiulis, G. Tamosauskas, R. Danielius, and A. Piskarskas, "Nonlinear second-harmonic compression with tilted pulses," Opt. Lett. 22, 1071– 1073 (1997).

11.   B. Richman, S. Bisson, R. Trebino, E. Sidick, and A. Jacobson, "Efficient broadband second-harmonic generation by dispersive achromatic nonlinear conversion using prisms only. Opt. Lett. 23, 497– 499 (1998).

12.   A. Schober, M. Charbonneau-Lefort, and M. Fejer, "Broadband quasi-phase-matched second-harmonic generation of ultrashort optical pulses with spectral angular dispersion," J. Opt. Soc. Am. B 22, 1699– 1713, (2005).

13.   P. Di Trapani, D. Caironi, G. Valiulis, A. Dubietis, R. Danielius, and A. Piskarskas, "Observation of temporal solitons in second harmonic generation with tilted pulses," Phys. Rev. Lett. 81, 570– 573 (1998).

14.   X. Liu, K. Beckwitt, and F. W. Wise, "Two-dimensional optical spatiotemporal solitons in quadratic media," Phys. Rev. E 62, 1328– 1340 (2000).

15.   F. Wise and P. Di Trapani, "The hunt for light bullets-spatiotemporal solitons," Opt. Photonics News 13, 29– 32 (2002).

16. J. P. Torres, M. W. Mitchell, and M. Hendrych, "Indistinguishability of entangled photons generated with achromatic phase matching," Phys. Rev. A 71, 022320 (2005).

17. X. Shi, A. Valencia, M. Hendrych, J. Torres, "Generation of indistinguishable and pure heralded single photons with tunable bandwidth," Opt. Lett. 33, 875– 877 (2008).

18. M. Hendrych, X. Shi, A. Valencia, J. P. Torres, "Broadening the bandwidth of entangled photons: a step towards the generation of extremely short biphotons," Phys. Rev. A 79, 023817 (2009)

19. J. Hebling, G. Almási, I. Z. Kozma, and J. Kuhl, "Velocity matching by pulse front tilting for large area THz-pulse generation," Opt. Express 10, 1161– 1166 (2002)

20. K.-L. Yeh, M. C. Hoffmann, J. Hebling, and K. A. Nelson, "Generation of 10 µJ ultrashort terahertz pulses by optical rectification," Appl. Phys. Lett. 90, 171121 (2007).

21. P. Gaal, K. Reimann, M. Woerner, T. Elsaesser, R. Hey, and K. H. Ploog, "Nonlinear terahertz response of n-type GaAs," Phys. Rev. Lett. 96, 187402 (2006).

22. J. Hebling, K.-L. Yeh, M. C. Hoffmann, K. A. Nelson, "High-power THz generation, THz nonlinear optics, and THz nonlinear spectroscopy," IEEE J. Sel. Top. Quantum Electron. 14, 345– 353, (2008)

23. T. Plettner, P. P. Lu, and R. L. Byer, "Proposed few-optical cycle laser-driven particle accelerator structure," Phys. Rev. Spec. Top.--Accel. Beams 9, 111301 (2006).

24. E. A. Peralta, K. Soong, R. J. England, E. R. Colby, Z. Wu, B. Montazeri, C. McGuinnes, J. McNeur, K. J. Leedle, D. Walz, and E. B. Sozer, "Demonstration of electron acceleration in a laser-driven dielectric microstructure," Nature 503, 91– 94 (2013).

25. P. Baum and A. H. Zewail, "Breaking resolution limits in ultrafast electron diffraction and microscopy," Proc. Natl. Acad. Sci. U. S. A. 103, 16105– 16110, (2006)

26. C. Chang, C. Tang, and J. Wu, "High-gain Thompson-scattering X-ray free-electron laser by time-synchronic laterally tilted optical wave," Phys. Rev. Lett. 110, 064802 (2013).

27. T. Plettner and R. L. Byer, "Proposed dielectric-based microstructure laser-driven undulator," Phys. Rev. Spec. Top.--Accel. Beams 11, 030704 (2008) .

28. M. R. Topp and G. C. Orner, "Group dispersion effects in picosecond spectroscopy," Opt. Commun. 13, 276– 281 (1975).

29. N. H. Schiller and R. R. Alfano, "Picosecond characteristics of a spectrograph measured by a streak camera/video readout system," Opt. Commun. 35, 451-454 (1980).

30. Z. Bor and B. Rácz, "Group velocity dispersion in prisms and its application to pulse compression and travelling-wave excitation," Opt. Commun. 54, 165– 170, (1985).

31. O. E. Martinez, "Pulse distortions in tilted pulse schemes for ultrashort pulses," Opt. Commun. 59, 229– 232 (1986).

32. S. Szatmari, G. Kuhnle, and P. Simon, "Pulse distortions in tilted pulse schemes for ultrashort pulses," Appl. Opt. 29, 5372– 5379 (1990).

33. J. Hebling, "Spectral resolving power," J. Opt. Soc. Am. A 11, 2900– 2904 (1994).

34. J. Hebling, "Derivation of the pulse front tilt caused by angular dispersion," Opt. Quantum Electron 28, 1759– 1763 (1996).

35. L. J. Wong and I. Kaminer, "Ultrashort tilted-pulsefront pulses and nonparaxial tilted-phase-front beams," ACS Photonics 4, 2257– 2264 (2017).

36. J. Turunen and A. T. Friberg, "Propagation-invariant optical fields," Prog. Opt. 54, 1–88, (2010).

37. H. E. Hernández-Figueroa, E. Recami, and M. Zamboni-Rached, Eds., Non-diffracting Waves (Wiley-VCH, 2014).

38. H. Sõnajalg and P. Saari, "Suppression of temporal spread of ultrashort pulses in dispersive media by Bessel beam generators," Opt. Lett. 21, 1162–1164 (1996).

39. P. Saari and K. Reivelt, "Evidence of X-shaped propagation-invariant localized light waves," Phys. Rev. Lett. 79, 4135–4138 (1997).

40. K. Reivelt and P. Saari, "Optical generation of focus wave modes," J. Opt. Soc. Am. A 17, 1785–1790 (2000).

41. M. A. Porras, I. Gonzalo, and A. Mondello, "Pulsed light beams in vacuum with superluminal and negative group velocities," Phys. Rev. E 67, 066604, (2003).

42. P. Di Trapani, G. Valiulis, A. Piskarskas, O. Jedrkiewicz, J. Trull, C. Conti, and S. Trillo, "Spontaneously generated X-shaped light bullets," Phys. Rev. Lett. 91, 093904 (2003).

43. C. J. Zapata-Rodríguez and M. A. Porras, "X-wave bullets with negative group velocity in vacuum," Opt. Lett. 31, 3532–3534 (2006).

44. D. Faccio, A. Averchi, A. Couairon, M. Kolesik, J. Moloney, A. Dubietis, G. Tamosauskas, P. Polesana, A. Piskarskas, and P. D. Trapani, "Spatio-temporal reshaping and X Wave dynamics in optical filaments," Opt. Express 15, 13077–13095 (2007).

45. M. Clerici, D. Faccio, A. Lotti, E. Rubino, O. Jedrkiewicz, J. Biegert, and P. D. Trapani, "Finite-energy, accelerating Bessel pulses," Opt. Express 16, 19807–19811 (2008).

46. F. Bonaretti, D. Faccio, M. Clerici, J. Biegert, and P. Di Trapani, "Spatiotemporal amplitude and phase retrieval of Bessel-X pulses using a Hartmann-Shack sensor," Opt. Express 17, 9804– 9809 (2009).

47. R. Donnelly and R. Ziolkowski, "Designing localized waves," Proc. R. Soc. London, Ser. A 440, 541– 565 (1993).

48. P. Saari and K. Reivelt, "Generation and classification of localized waves by Lorentz transformations in Fourier space," Phys. Rev. E 69, 036612 (2004).

49. S. Longhi, "Gaussian pulsed beams with arbitrary speed," Opt. Express 12, 935– 940 (2004).

50. H. E. Kondakci and A. F. Abouraddy, "Diffraction-free pulsed optical beams via space-time correlations," Opt. Express 24, 28659– 28668 (2016).

51. K. J. Parker and M. A. Alonso, "The longitudinal iso-phase condition and needle pulses," Opt. Express 24, 28669– 28677 (2016)

52. M. Yessenov, B. Bhaduri, H. E. Kondakci, and A. F. Abouraddy, "Classification of propagation-invariant space-time light-sheets in free space: Theory and experiments, " arXiv:1809.08375 (2018).

53. H. E. Kondakci and A. F. Abouraddy, "Diffraction-free space-time beams,". Nat. Photonics 11, 733– 740 (2017).

54. H. E. Kondakci and A. F. Abouraddy, "Airy wavepackets accelerating in space-time," Phys. Rev. Lett. 120, 163901 (2018).

55. H. E. Kondakci, M. Yessenov, M. Meem, D. Reyes, D. Thul, S. R. Fairchild, M. Richardson, R. Menon, and A. F. Abouraddy, "Synthesizing broadband propagation-invariant space-

time wave packets using transmissive phase plates," Opt. Express 26, 13628– 13638, (2018).

56. H. E. Kondakci, A. F. Abouraddy, "Optical space-time wave packets of arbitrary group velocity in free space," arXiv:1810.08893 (2018).

57. B. Bhaduri, M. Yessenov, and A. F. Abouraddy, "Space-time wave packets that travel in optical materials at the speed of light in vacuum," Optica 6, 139– 146 (2019).

58. B. Bhaduri, M. Yessenov, and A. F. Abouraddy, "Meters-long propagation of diffraction-free space-time light sheets," Opt. Express 26, 20111–20121 (2018).

59. H. E. Kondakci, and A. F. Abouraddy, "Self-healing of space-time light sheets," Opt. Lett. 43, 3830–3833 (2018).

60. G. B. Arfken, H. J. Weber, and F. E. Harris, Mathematical Methods for Physicists: A Comprehensive Guide (Academic Press, 2012)

61. M. Abramowitz, I. A. Stegun, Eds., Handbook of Mathematical Functions: with Formulas, Graphs, and Mathematical Tables (Dover Publications, 1965).

62. H. E. Kondakci, M. A. Alonso, and A. F. Abouraddy, "Classical entanglement underpins the propagation invariance of space-time wave packets," arxiv:1812.1056 (2018).

63. M. Yessenov, L. Mach, B. Bhaduri, D. Mardani, H. E. Kondakci, G. A. Atia, M. A. Alonso, and A. F. Abouraddy, "What is the maximum differential group delay achievable by a space-time wave packet in free space," arxiv:1901.00538 (2019).

64. H. E. Kondakci, N. Nye, D. Christodoulides, and A. F. Abouraddy, "Tilted-pulse-front space-time wave packets," ACS Photonics 6, 475-481 (2019).

CHAPTER 6: CONCLUDING REMARKS

In the first part of this work, the properties of PT-symmetric metasurfaces have been investigated for the purposes of free-space modal control. Passive PT-symmetry was introduced in "distorted" honeycomb-like lattices, through loss elements. Selective directional scattering over a broad range of wavelengths was observed, while the introduced two-dimensional geometric distortions determine the far-field directivities. The observed asymmetric light transport was attributed to a spontaneous PT symmetry breaking mechanism. Unidirectionality and violation of Friedel's law of diffraction have also been reported, as a result of the complex and deeply subwavelength interactions between gain and lossy elements. The presented methodology can be readily extended to other wavelength regions and open up new possibilities in the field of reconfigurable optics. Of great interest, would be to investigate the behavior of the proposed non-Hermitian arrangements close to the exceptional point of operation. In this case, not only the eigenvalues, but also the eigenvectors coalesce, leading to extraordinary transmission properties.

Mode management has been also demonstrated in guided arrangements, by exploiting notions from supersymmetry. More specifically, we have presented the first realization of an integrated SUSY laser array. By applying appropriate isospectral/supersymmetric transformations, we have judiciously designed an active array of waveguides, where the superpartner system filters the undesired optical modes. The existence of an unbroken SUSY phase in conjunction with a judicial pumping of the laser

array, can promote the in-phase supermode thus resulting to a high radiance emission. The spectral response, far-field emission, and light-light characteristics revealed a superior performance of the proposed structure compared to conventional multi-element waveguide configurations. This new mechanism of phase-locking is general and indicates the potential of SUSY for high brightness single mode laser arrays and optical filtering applications.

In the third part of this dissertation, we have studied the properties of random assembly configurations and exhibited the potential of reconfigurable lasing in a disordered nanoparticle platform. Using an alternating current electric field, we control the nanowire orientation to dynamically control the collective scattering of the sample and thus light confinement. Field autocorrelation, spectrum measurements, and reduced scattered efficiency numerical calculations, have shown that lasing can be manipulated by exerting control over the position and orientation of the nanoparticles. Moreover, the generality of the tunable lasing response has been demonstrated with a variety of anisotropic scatterers, indicating the applicability of the proposed methodology in dynamic metamaterial architectures

Lastly, we have synthesized and characterized ST wave packets that have a tilted-pulse-front structure. Diffraction-free space-time pulses are generated by an appropriate entanglement of both the temporal and spatial degree of freedom. In that respect, propagation invariant beams can be generated potentially with arbitrary transverse profiles. Respective analytical solutions have been derived after complexification of the time and spatial coordinates. Exploiting these findings, we experimentally synthesize ST wave packets that have a pulse intensity front that is tilted with respect to the propagation axis.

By establishing this link between space-time propagation-invariant beams and TPF pulses, a path is opened towards taking into advantage the unique properties of ST wave packets in both nonlinear and quantum optics.